University of Louisville
ThinkIR: The University of Louisville's Institutional Repository

Electronic Theses and Dissertations

11-2020

An exercise device used to achieve bone formation metrics for the strengthening of the proximal femur.

Sean P. Coyle
University of Louisville

Follow this and additional works at: https://ir.library.louisville.edu/etd

 Part of the Biomedical Devices and Instrumentation Commons

Recommended Citation

Coyle, Sean P., "An exercise device used to achieve bone formation metrics for the strengthening of the proximal femur." (2020). *Electronic Theses and Dissertations.* Paper 3434.
https://doi.org/10.18297/etd/3434

This Master's Thesis is brought to you for free and open access by ThinkIR: The University of Louisville's Institutional Repository. It has been accepted for inclusion in Electronic Theses and Dissertations by an authorized administrator of ThinkIR: The University of Louisville's Institutional Repository. This title appears here courtesy of the author, who has retained all other copyrights. For more information, please contact thinkir@louisville.edu.

AN EXERCISE DEVICE USED TO ACHIEVE BONE FORMATION METRICS FOR THE STRENGTHENING OF THE PROXIMAL FEMUR

By

Sean P. Coyle, B.S. University of Louisville Speed School, 2016

A Thesis
Submitted to the Faculty of the
University of Louisville
J. B. Speed School of Engineering
as Partial Fulfillment of the Requirements
for the Professional Degree

MASTER OF ENGINEERING

Department of Bioengineering

November 2020

AN EXERCISE DEVICE USED TO ACHIEVE BONE FORMATION METRICS FOR THE STRENGTHENING OF THE PROXIMAL FEMUR

By

Sean Coyle

A Thesis Approved on

11/23/2020

By the following Thesis Committee

Digitally signed by Michael J Voor
Date: 2020.11.30 17:53:46 -05'00'

Thesis Chair

Digitally signed by Thomas J. Roussel, Jr.
Date: 2020.11.30 18:58:42 -05'00'

Committee member

John Caruso

Digitally signed by John Caruso Date: 2020.11.30 19:09:10 -05'00'

Committee member

ACKNOWLEDGMENTS

Foremost, I would like the sincerely thank my advisor, Dr. Michael Voor, and the rest of my committee, Dr. Thomas Roussel and Dr. John Caruso, for continuing to work with me over the course of this thesis. With their patience and abundant knowledge, I have been able to further develop my own knowledge and skills in the field of bioengineering through this experience. Their support has motivated me to continually develop myself academically and personally.

I also have Daniel Mills, B.S. to thank for outstanding aid in custom hardware and custom software used throughout testing. Similarly, I appreciate Jeremy Turner and FirstBuild for their time, generosity, and use of their resources through fabrication. I also could not have completed this without the volunteers who opted to donate their time and efforts into testing.

With abundant gratitude, I thank my mom who has continued to be a mentor, inspiration, and friend throughout not only my studies but throughout my entire life. Her support among that of my friends, faith, and lab mates along the way has been both warmly received and invaluable.

ABSTRACT

Lateral falls often lead to hip fracture particularly in the elderly who have low bone mineral density. These fractures frequently lead to indirect mortality soon after injury. Normal use over the course over a lifetime leads to optimized adaptation of the bone in the proximal femur according to normal loading. A lateral fall generates non-normal, lateral loading at the proximal hip where the bone has not adapted to withstand such loading. The resulting fracture is generated by reversed strains on the bone tissue in the femoral neck in the hip in contrast to vertical, quotidian loading. Modern practices for preventing hip fractures are largely supplements or medications while standard exercise and vibration therapies are also used. Preventative measures such as these may help but it is apparent that more is needed.

A supplementary exercise device intended to stimulate lateral, localized bone formation at the hip while providing user quality feedback could be a promising solution to overcoming such high hip fracture rates. The device consists of: a main body in the form a lap plate, two adjustable pad arms that optimally position two impact pads adjacent to the user's lateral proximal femur, and a knee plate that helps maintain the device in the optimal position on the lap relative to the hip joint. Anabolic thresholds for strain magnitude and strain rate are both shown to be critical metrics for stimulating bone remodeling such as what occurs in the femoral neck. The objectives of this second-generation prototype are to design, fabricate, and validate a versatile device with user

performance feedback to allow the user to comfortably achieve the biological thresholds for appropriate anabolic bone remodeling in the femoral neck.

The prototype design was based on anthropometric data representing the typical archetype. Strength of key elements was analyzed via manual calculations and finite element analysis (FEA). Ideal sensor placement was also analyzed via FEA to maximize sensitivity. Quasi-static testing in an MTS machine across the breadth of relevant user settings is performed to translate strain gage output to pad force. The discrete results of this testing were then used to generate a 95% two-sided regression model of continuous predictors for accurate force measurement based on user-specific setting inputs. Custom software was developed to process the raw data and provide user feedback. Additional accelerometer data was processed as a potentially simpler alternative to strain data for feedback to the user regarding proper exercise effort. Dynamic testing was collected on 10 volunteers who perform a swift hip abduction using the prototype which creates three-point bending in the femur that generates strain in the femoral neck. Additional tests were performed to optimize data outcome based on user factors. Pad force rate was converted to theoretical bone strain rate based on data provided by the first-generation device study. Strain and strain rate data were compared to the accepted biological thresholds to stimulate remodeling taken from the prevailing bone biomechanics literature.

A prototype was successfully fabricated after calculations were used to validate design integrity. This device was proven functional in acquiring dynamic data via custom software after use by volunteers of varying anthropometry. Before this dynamic data was acquired, preferred strain gage placement was determined to provide the most sensitive measure of pad impact force by calculating stress profiles at minimum and maximum

settings and the regression model was validated via four-in-one plot analysis with an R^2 of 99.97%. Ideal instruction and performance of the exercise using the device were refined though a series of sub-studies evaluating data acquisition and data metrics. These sub-studies suggested optimal feedback is achieved through an appropriate knee arm setting and a narrow pad arm setting using extra padding under the instruction to swiftly drive through the pad to a 60 beats per minute metronome without pushing down on the plate. Volunteer data revealed an average peak value of 499.5 N surpassing the 350 N minimum and 450 N suggested force to achieve strain magnitudes above the 1000 με osteogenic threshold. Similarly, the average strain rate of the volunteers averaged 21509.6 με/s far exceeding the 10000 με/s bone remodeling threshold. These findings suggest that this device has the potential induce anabolic bone remodeling at the hip, thus encouraging more study toward aims of reduced hip fracture rates. Acceleration data did not prove to be an alternative to strain data for user feedback.

TABLE OF CONTENTS

NOMENCLATURE

A_{Circle} = Area of Circle
C = Center of Mohr Circle
I_A = Area of Inertia
M = Moment Arm
S = Shear Force
y = Distance from Neutral Axis
σ_B = Bending Stress
σ_P = Principal Stress
τ_{Max} = Maximum Shear Stress

LIST OF TABLES

LIST OF FIGURES

I. INTRODUCTION

A. Clinical Need

Hip fractures are among the most common fractures in the aging population and often lead to tragic consequences because of high mortality rates following hip fractures. It is well known that mortality is high within the first three months to a year post-hip fracture especially in those of higher age groups (Farahmand et al., 2005; Koh et al., 2013; von Friesendorff et al., 2016). Farahmand et al., 2005 found up to a four-fold larger likelihood of death following a hip fracture than age-matched control groups. Extended mortality out to six years after such a fracture approaches 40% which shows 27% higher mortality than the control group. However, this is shown to be largely due to chronic-disease comorbidity as opposed to the direct hip fracture trauma (Farahmand et al., 2005; Koh et al., 2013). Most commonly, cardiovascular disease, pneumonia, and cancer are the culprits of the increased death (Faramand et al., 2005; Friesendorff et al., 2016; Koh et al., 2013).

Despite being one of the most prevalent causes of death in the US, hip fractures are often disguised as the aforementioned in comorbidity statistics making hip fracture a larger issue than it appears. In the United States alone, more than 258,000 people of age 65 or older suffered hip fractures in 2010. Extrapolated from this data, there is an estimated 11.9% growth in hip fractures by 2030. (Stevens & Rudd, 2013) Such an increase indicates an ever increasing need to prevent these from occurring. Within this pervasiveness, it is suggested that the 60+ year old females have a proximal femur

fracture nearly 2.5 times as frequently as males of a similar age (Glinkowski et al., 2019). There exists a strong, positive correlation between low bone mineral density in women and hip fractures (Määttä et al., 2014). The US national economic burden of hip fractures was $12.1 billion in 2005 and is projected to more than double by 2025 (Burge et al., 2007).

B. Bone Biomechanics

Moving forward means having an in-depth understanding of how the proximal femur behaves under different loading conditions. Under loading, bone will either support the load or fail and fracture. Bone responds to how it has been recently loaded over time compared to prior use. This can result in strength, density, and size changes of the bone that increase with overloading, decrease with reduced loading, or maintain without a change in typical loading. Understanding the mechanics of how it remodels by adapting to use over time and how it fractures under excessive loading are crucial. While forces are applied during both, variables such as how the loading occurs and how the bone responds to the load matter greatly. To prevent hip fracture, stimulating remodeling safely via an appropriate amount and type of overloading is the key.

1. Hip Fractures

The cause of hip fractures in the elderly is simply falling onto one's side in over 90% of cases (Hayes et al., 1993). Even a simple fall from standing height onto the greater trochanter of the femur generates enough energy to fracture the neck or trochanteric region of the hip (de Bakker et al., 2009; Horii et al., 2016). Having adapted to normal loading of the hip from walking, the bone can sustain relatively high loads downward from the acetabulum through the medial wall of the proximal femur and into

the shaft. This contrasts with the lateral, non-normal loading seen in falls. An analysis of the internal stresses of the hip reveals the typical compression and tension of the bone to be effectively reversed under lateral impact conditions as displayed in Figure 1 (de Bakker et al., 2009). This is particularly true for those with lower bone density caused by aging

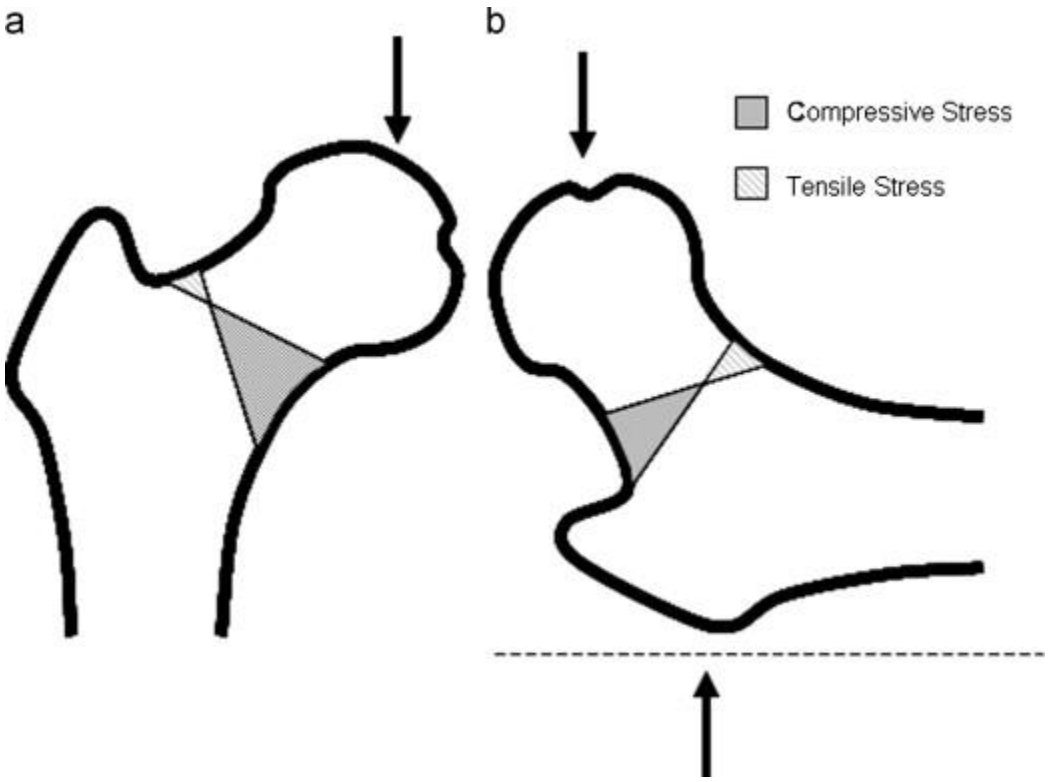

FIGURE 1 – The femoral neck as it undergoes respective stresses from a) walking versus b) a lateral fall (de Bakker et al., 2009).

and low bone density where there is not enough bone in the proper orientation to appropriately carry the forces. It is widely accepted that only about 7000 με is required to begin bone failure but specific values vary around this based on whether the bone is cortical or trabecular and whether the stress applied is tensile or compressive (Bayraktar et al., 2004; Niebur et al., 2000; Pistoia et al., 2002). Propagation of bone failure in femoral neck hip fractures therefore commonly begins in the thinned superior neck before

generating a second crack upward from the inferior neck as exemplified in Figure 2 (de Bakker et al., 2009). These locations are the same locations where the stress is reversed from Figure 1. This highlights the potential benefit of proactive lateral stimulation to induce bone remodeling in the proximal femur to prevent such failure.

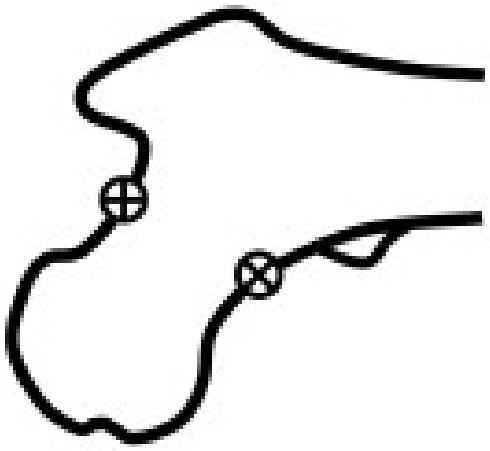

FIGURE 2 – Locations of femoral neck failure as propagated over time under acute lateral loading where the ⊕ symbol indicates the location of the first fracture and the ⊗ symbol indicates the location of the second fracture (de Bakker et al., 2009).

2. Bone Remodeling

Bones get their strength from an organic matrix and calcium salts to provide structure and strength. The organic matrix is largely comprised of collagen fibers providing high tensile strength. High compressive strength is a result of hydroxyapatite crystals that overlap adjacent to the collagen fibers creating a rigid structure. Osteoblasts are responsible for laying collagen monomers and proteoglycans. The monomers ultimately polymerize into fibers which readily precipitate calcium salts from the proteoglycans on the surface to form the mature bone structure. (Hall, 2016) While both remodel anisotropically according to normal loading and its vectors, the resulting difference in structure of cortical versus trabecular bone leads to different mechanical properties. Consequently, bone is capable of withstanding high loads particularly in the

directions of typical loading from daily use but is more vulnerable to failing under high loads in non-normal directions. This is especially in the case for trabecular bone such as that in the femoral neck. Each type of bone remodels on its surface via osteogenesis and resorption (Hall, 2016; Li et al., 2017). Due to surface remodeling of bone, the high surface area, low matrix volume trabeculae network of trabecular bone can more readily remodel in contrast to the low surface area, high matrix volume of cortical bone (Li et al., 2017). Being more ready to remodel provides trabecular bone with more sensitivity towards laying or resorbing bone according to changes in direction and quantity of loading.

Osteoclasts resorb bone by releasing acids and enzymes to break down the matured bone structure (Hall, 2016). This process of balancing the break-down and reforming of bone is bone remodeling. Independently, it has been found that resorption occurs on the order of weeks while rebuilding is on the order of months. Specific proteins and hormones mediate the rates each phase of the process cell-to-cell maintaining the appropriate bone density to function. (Caetano-Lopes et al., 2007) As people age, this process slows and becomes less balanced resulting in lower bone density. Decreased bone mineral density is especially present in post-menopausal women which is attributed to a drop in estrogen (Dick and Prince, 1997; Prince et al., 1990; Ziller et al., 2012). This drop ambiguously affects the parathyroid hormone, cholecalciferol, and osteoprotegerin presence and local influence on the availability of RANKL to allow preosteoclasts to mature into active osteoclasts (Hall, 2016). Over time, this degradation frequently leads to osteopenia and osteoporosis. In the context of the proximal femur, low bone mineral density translates to thinning of both the trabecular network of trabecular bone as well as

the cortical shell of the epiphysis surrounding it. This lack of bone structure in combination with the previously discussed anisotropic properties of bone leaves the femoral neck particularly prone to failure in the case of the femur undergoing the large atypical, longitudinal forces of a lateral fall for someone with low bone mineral density.

Dynamic loading elicits different strains, strain rates, and vibrations that induce an increase in bone mineral density (Manske et al., 2009). Varying strains and their rates have been tested many times to show a positive correlation between their presence and an increase in bone strength (Duncan et al., 2002; Judex et al, 2000; Rubin & Lanyon, 1985; Troy et al., 2020; Turner & Takano, 1995). Similarly, varying vibrational frequencies and amplitudes have been tested to generate the desired biological response. It is believed that in these lies the key to improving bone health non-pharmacologically by utilizing an external stimulus. In one study, functionally isolated turkey ulnae were studied as strain was applied through 500-4000 με (Rubin & Lanyon, 1985). The results of the study indicated an increase in bone development with increasing strain while strains lower than 500 με weakened bones. In humans, there have also been studies testing how impact affects bone stimulation in athletes. These studies consistently reveal that in athletes participating in strain-inducing impact activity such as runners have stronger bones than those even of high-level athletes without impact such as swimmers and cyclists by 10% in the femoral neck as they do not generate similar strains (Duncan et al., 2002).

Beyond strain magnitude alone, strain rates have also been proven to heavily influence bone growth. One study by Judex et al, 2000 tested bone reformation rates by having roosters perform drop-jumps versus a walking control group over three weeks. The strain gages recorded data from the mid-diaphyseal tarsometatarsus bone in the leg.

The data from the gages revealed a 30-40% higher strain magnitude as well as a 740% increase in strain rate which lead to an overall 370% increase in bone formation rate under dynamic loading. Furthermore, it was concluded that the strain rate was a much more significant impact on bone formation rates than other inputs (Judex et al., 2000). While keeping sufficient bending strain magnitudes the same in a bending load, osteogenesis significantly increased with strain rate in rat tibiae (Turner & Takano, 1995). What is taken from this is that remodeling also requires a sufficient strain rate caused dynamically in addition to a sufficient magnitude. If the strain rate is insufficient, the remodeling process will not take place.

Both strain and strain rate as stimuli for bone adaptation have also been studied together as independent groups of the same study by Troy et al., 2020. 102 women were separated into two groups of strain and strain rate each with three sub-groups of a control, low respective magnitude, and high respective magnitude. Over a 12-month period, documented values of loading and time under uniaxial compression for 100 cycles 3-4 times a week are compared to the BMD from starting and finishing quantitative CT scans. Subject-specific force requirements to achieve the appropriate target metric in the ultradistal radius is found via user-specific finite element analysis (FEA) of compiled starting scan results. The found value is applied to the custom device for adequate performance feedback. From the 66 women who completed the study, the results imply that trabecular osteogenesis in the ultradistal radius is stimulated collectively by strain, strain rate, and number of respective loading events in contrast to the controls. Independently, both strain rate and amount of loading events had the largest influence on the increase in integral bone mineral content. Limitations of achieving target metrics in

the high groups left narrower variability between high and low data than desired which may explain narrow differences in bone mass between high and low groups found in the results. (Troy et al., 2020) Ultimately, this study is another testament to the importance of mechanical loading on bone remodeling especially under cycles of dynamic loading.

Application of these strain magnitude and strain rate findings are applied to dynamic testing of a hip abduction prototype for strengthening the proximal femur in a preceding study of an earlier prototype iteration in Osbourne, 2017. This study utilizes FEA as well as artificial, ex-vivo cadaveric, and in-situ cadaveric femurs to evaluate laterally applied strain magnitudes and strain rates generated by three-point bending in a hip abduction motion. This hip abduction motion is characterized by each femur externally rotating about its respective fixed acetabulum through the transverse plane from a seated position. Throughout the course of the study, 450 N is used as the applied load to generate bone strain. The reported compressive strains in the femoral lateral neck according to the FEA and in-situ tests are 2451.6 με and 1511.3 με, respectively. These findings are within the defined target range for osteogenic stimulation of lamellar bone at 1000 με but under the 3100 με that causes microdamage leading to woven bone formation. Strain rate in the in-situ cadaver study yielded 36954 με/s (Osbourne, 2017). This is larger than the defined threshold of 10000 με/s for anabolic bone remodeling. Reaching these metrics implies promising possibility in a future prototype iteration as well as result guidelines.

C. Exercise

Exercise has traditionally been considered important for wellbeing such as cardiovascular health, muscle development, agility, and various rehabilitation. Over time

better equipment has been developed but still focuses on muscular and cardiovascular conditioning. However, the influences of load bearing exercise on bone remodeling have not been considered nor targeted by equipment developers. Although, there has been an increase in research literature on how exercise influences bone mineral density as well as the ability to reduce the risk of falling. Falls are the most common cause of femoral neck fractures.

1. Fracture Prevention

Exercise has been shown to reduce the rates of falls. A meta-analysis of 21 studies including over 5,500 subjects supports the conclusion that balance, strength, and gait exercise training significantly reduces the rates of falls in the aging population (Lee et al., 2017). These forms of exercise target the muscular and coordination ability of the person but do not necessarily reduce injury severity in the event of a fall. Similar to some previously reviewed literature, Narra et al., 2013 studied how different exercises influence growth in the femoral neck. Between the high-impact, odd-impact, low-impact, high magnitude, and no-impact exercises, the high-impact and odd-impact exercises had the highest improvements in bone mineral density (BMD). However, the odd-impact exercise utilizing multi-directional loading had the greatest overall improvement in more regions of the bone (Narra et al., 2013). This further indicates that trabecular bone – particularly that of the femoral neck – adapts to the loading of the bone according to the direction of loading generated by the exercise to become stronger. Even among similar exercises, the faster movement as performed during power training versus strength training significantly reduced bone mineral density loss in the proximal hip and spine of 53 osteopenic, postmenopausal women (Stengel et al., 2005). Many forms of exercise

benefit the trabecular bone mineral density in aging population best by utilizing dynamic, acute loading to achieve the higher strain rates and direction necessary to reduce the risk of fall-related injury.

D. Solution

Having an in-depth understanding of bone remodeling opens new avenues for hip fracture prevention. Most of what is currently available are supplements, drugs, balancing exercises, vertical impact exercise, and implants post-fracture. While some of these are effective at reducing falls or strengthening the bone, the device designed for this thesis can be used as a further aid in preventing falls via muscular conditioning alongside a much more effective tool for lateral hip strengthening to reduce injury in the event of a fall. By performing the exercise with the device, the hip abductor muscles will likely become stronger. This may enhance the user's ability maintain balance thus avoiding a fall. Additionally, the dynamic bone stresses generated as the device is used should stimulate a net increase in bone formation in the superolateral femoral neck by generating the appropriate strains and strain rates in the local bone tissue. Such development could reduce the likelihood of bone failure in the event of a lateral fall. Appropriately utilized, the device will create three-point bending in the femur with sufficient strain magnitude and strain rate as seen in Figure 3 (Osbourne, 2017). Its design was based on the most vulnerable population: aging women. The objectives herein are to design, fabricate, and validate a second-generation prototype device with user feedback and adjustable settings that meets the biological requirements for stimulating appropriate trabecular and cortical bone remodeling in the femoral neck. If the device is appropriately made with accurate

feedback, then target users should be capable of comfortably generating the target metrics when fitted and used properly.

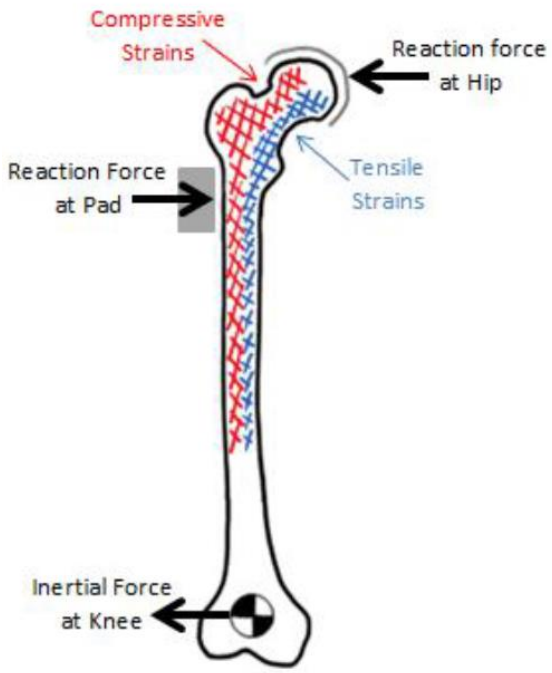

FIGURE 3 – During hip abduction into the pads of the device, the inertial force at the knee generates strains in the femoral neck comparable to those of a lateral fall.

II. MATERIALS & METHODS

A. Device Design

A first-generation device as seen in Figure 4 was fabricated with 80/20 Inc. aluminum bar stock and fasteners with padding for the impact generated by a hip abduction exercise (Osbourne, 2017). This exercise required that the user to be in a seated configuration with only the buttocks supported by a rigid seat so that the motion of the hips is unrestricted. While seated with feet on the floor, the knees were to be bent approximately 90 degrees. To perform the motion of the exercise, the knees were to begin together before the femurs were both swiftly abducted in an outward arc about each hip joint. This outward rotational movement would be stopped by a fixed padded barrier to generate the desired three-point bending loading in the femurs. In order to be effective, the device design should facilitate this exercise safely, comfortably, and consistently. This project sought to improve the design by considering an improved performance of the exercise motion, user safety, effectiveness, reproducibility, adjustability, and comfort. Device strength was an important factor for both user safety and its own ability to perform without failure over time. Onboard sensors and the provision of user feedback were also added to the design. Altogether, the second-generation design aims to account for and improve upon the aforementioned factors to produce a fully functional tool for safe loading of the proximal femur with the goal of stimulating bone strengthening through remodeling.

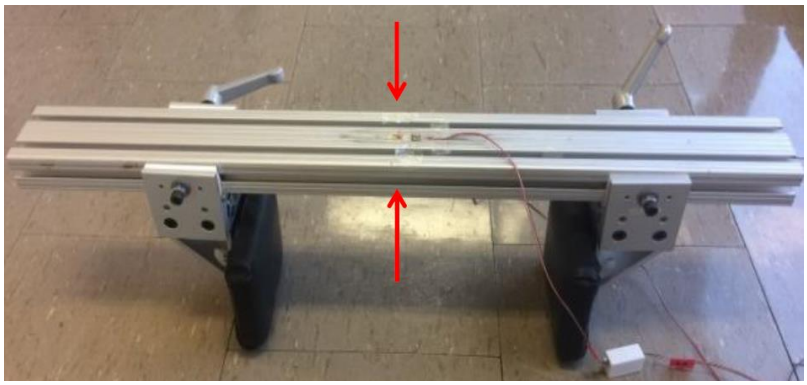

FIGURE 4 – The first iteration prototype with arrows depicting mounted strain gage locations (Osbourne, 2017).

1. Size, Shape, and Function

For the new design, the concept of three-point bending of the proximal femur remained the same alongside much of the device layout of the first prototype. Specifically, an aluminum frame, lateral padded supports, and basic geometry of the abduction exercise were maintained for the second-generation prototype. 6061 aluminum – the material for much of the new design – is a functional balance of strength and weight. Padding must be maintained for comfort and subject safety. The fundamental abduction exercise is critical in order to load the hip and exercise the hip abductors to consequently stimulate the bone and increase balance, respectively.

Despite the similarities, many new elements and the design of the former elements were improved. The ideal location for the pads to produce appropriate peak compressive strains and strain rates in the superior-lateral femoral neck is most proximal to the greater trochanter but not over the acetabulum (Osbourne, 2017). As a result, the pads must be shifted further back to fit the user's anatomical constraints at the hip without obstruction from the other anatomy such as the abdomen as seen in the previous design. An adjustable knee positioning plate was added to aid in maintaining the position of the impact pads at the proximal-lateral femur position. Comfort and ease of use were

further considered via implementation of a plate with handles versus a bar. Throughout the design of each piece, design simplification for ease of fabrication or potential replication was considered along with user ease and safety.

a. Top Plate

The top plate is the fundamental element that forms the framework to which the other elements of the device are attached. These elements include other parts of the device as well as stain and acceleration sensors for feedback. It also serves to help maintain the vertical positioning of the pads for consistent impact on the lateral femur by resting on the user's lap. Length of the plate was determined from minimum anthropometric data to best fit most intended users seen in Appendix I. In 5^{th} percentile women of ages 40-69, the upper leg length on seated individuals from the inguinal crease to the distal end of the femur was recorded to be approximately 30.1 cm (Fryar et al., 2012). However, this value did not account for further tissue or patellar length to reach the front of the knee. This additional length was estimated to be about 2 cm. A resulting 33.02 cm length was used for the plate at its minimum length. The minimum width of the plate was determined based upon several other elements and parameters such as pad thickness and hip width through a range of potential users. A minimum distance from greater trochanter to greater trochanter in anticipated users is expected to be 27.94 cm. Due to the thickness and position of other parts, 35.56 cm is conservatively selected for the top plate width in the first iteration. The proximal sides of the plate from which the pad arms adjust their length were tapered at 30 degrees to adjust at an appropriate pad width to depth ratio according to the user. To compensate for a user's abdominal shape, the proximal edge of the plate was bellied inward for comfort. Many arched cuts were

made in the plate to lighten the device while maintaining its ability to appropriately handle applied forces. Plate thickness was a critical parameter influencing the flexibility of the top plate as well as the total weight of the device. Flexibility was important to the detection of acceleration and strain via sensors as discussed later which were induced by forces applied during abduction. A height of 0.635 cm was assumed to suit the needs and parameters of the device application to be evaluated under Strength Analysis. All holes in the plate were threaded to allow screws to tighten directly into the plate from the top without excess protrusion nor fasteners such as a nut. The final design was cut using a waterjet and manually tapped at FirstBuild. A second iteration plate was created with additional features. Weight was removed from the device via slots cut out where stresses were minimal. The remaining frame has arcs to match the motion of the legs as the exercise is performed. The path of the leg through the exercise would leave the knee and some of the leg past the plate width in the first iteration. Consequently, the addition of lateral handles onto the top plate in the second iteration increases the plate width to 48.26 cm allowing the leg to stay under the plate through the exercise and thus maintain a consistent vertical position. Furthermore, these side handles allow for easier transport. A thin, smooth adhesive bottom was considered as an addition to the plate but was not utilized throughout testing. Figure 5 shows the current iteration of the top plate.

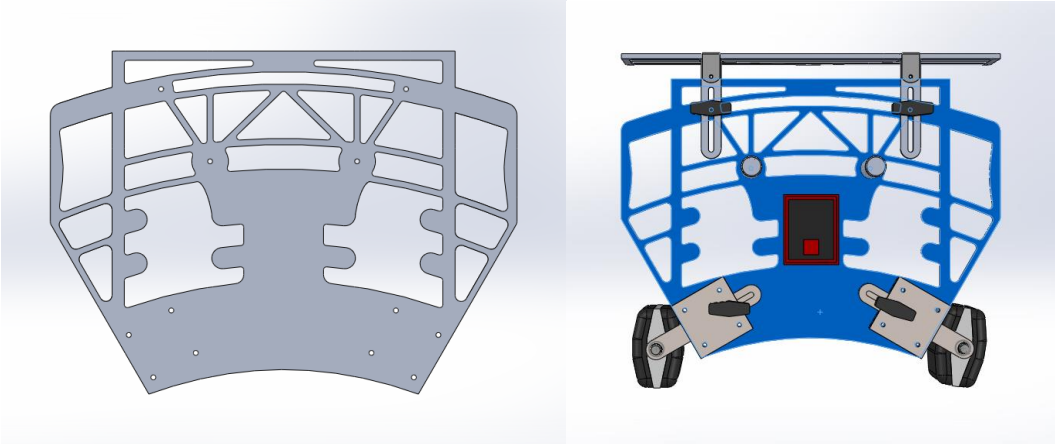

FIGURE 5 – The SolidWorks model of the top plate part (Left) and the integrated model where the top plate part is highlighted blue (Right).

b. Pad Arm

Responsible for ultimately translating the load from the user into the plate, the pad arm was critical to the functionality of the device. Stainless steel was selected as the material for its strength and corrosion resistance. It must be strong and rigid enough to adequately transfer the load into the plate providing consistent feedback to the strain gage (load sensor) and accelerometer. Another element of strength is the ability to withstand the forces from the pad pin as they enter the arm. The stainless steel 1.5875 cm threaded hole was expected not to deform over time due to the 1.27 cm thickness of the part and enough of a remaining radius.

As a close fit, moving part, it was important that it remain smooth and maintenance free. Length of the part was critical in the design of the part for its need to accommodate different sizes of people. Ergonomics data for the total waist depth of 5th to 95th percentile women has shown a fluctuation of 8.89 cm in Appendix II (Openshaw, 2006). Based on this value and the expectation that the change in total waist width would not exceed this, the desired range of motion for each arm was raised to 5.08 cm. The

extra space additionally accommodates for the plate width potentially being small. Having kept the element as weight efficient as possible, the smallest length to compensate for this range of motion was selected to be 15.24 cm. On this length, a shallow slot was added to aid in guiding the part as well as securing the holding knob. One end of the slot would begin at the midpoint of the part while the end would leave 1.27 cm from the end of the part making the total slot length 6.35 cm. Having accounted for the 30˚ angle at which the arms were placed, the tolerance for the range of motion becomes just over 5.08 cm. Figure 6 shows the final design of the pad arm. The rounding of the ends was to reduce sharp corners. The final part was manually milled and tapped at FirstBuild.

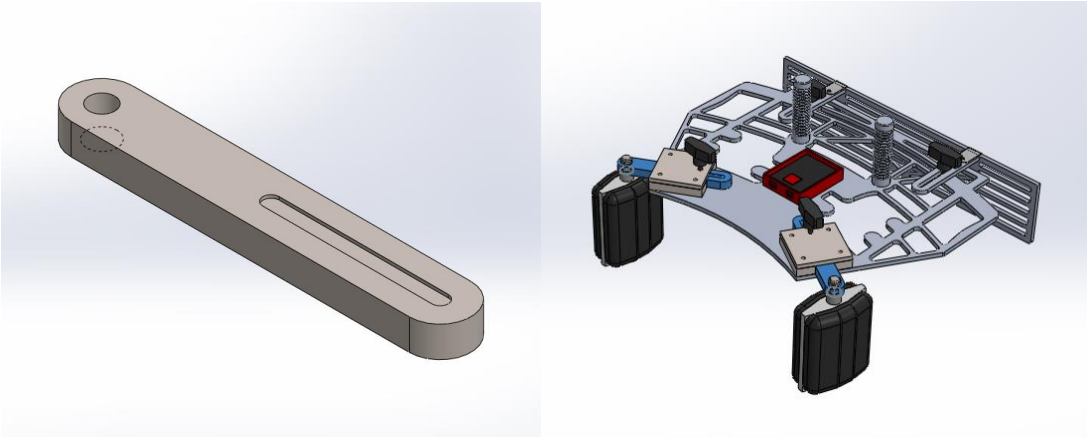

FIGURE 6 – The SolidWorks model of the pad arm part (Left) and the integrated model where the pad arm parts are highlighted blue (Right).

c. Knee Arm.

The knee arm was not designed to carry forces but is important in the performance of the exercise. At the start of the exercise the knees were to be together and resting on the back of the plate in order to aid in standardizing the start position of each repetition and prevent the device from shifting backward during use. Adjustability was again necessary to accommodate users of different femur lengths. Varying femur length

was compensated using anthropometric data of 5th to 95th percentile females. By taking the buttock-to-knee data and removing both the plate length and the waist depth data, the variance was roughly 2.54 cm (Openshaw, 2006). However, it was expected that there would be more variance than this so 7.62cm was selected to match the change within either 5th to 95th percentile measurement used. The aluminum knee arms were cut by waterjet at FirstBuild and filed to the final shape as seen in Figure 7.

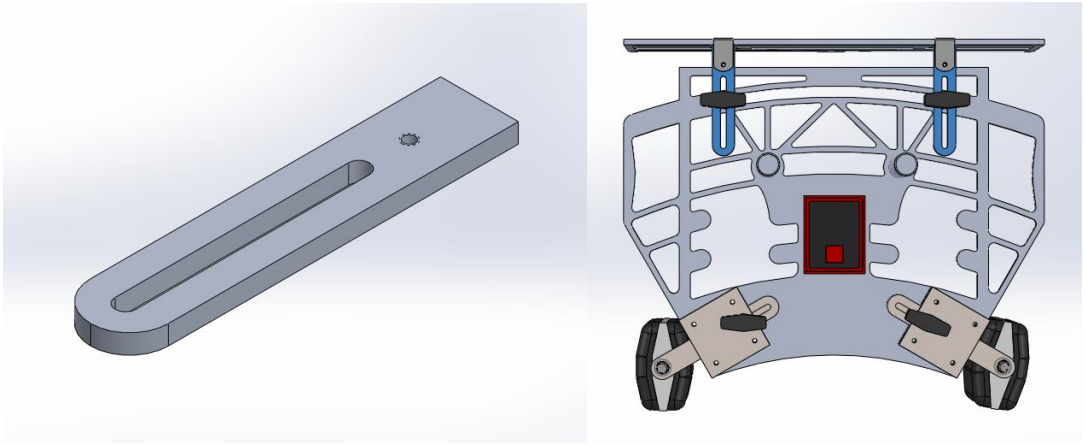

FIGURE 7 – The SolidWorks model of the knee arm part (Left) and the integrated model where the knee arm parts are highlighted blue (Right).

d. Pad Mount.

While it was a simple element of the design, the pad mount had to meet several parameters in order to properly translate the load of the exercise into the part. Additionally, it was responsible for how the device applied the loads back into the user. Based on previous work, the reaction force at the trochanter of the femur needs to be precise but also safe for the user (Osbourne, 2017). Consequently, the pad mounts were designed to freely rotate about a pin to load the bones from the center of the mount at the point of interest. To aid in this process, the pad mount was also curved to reduce excessive dampening with large surface area contact while maintaining a consistent the

location of the load through the center of the pin. It was made from UHMW Polyethylene for its excellent impact rating and weight efficiency. Due to the slick nature of the material, texture was added to aid in the holding of the pad to the mount. Another iteration was designed in case pad adhesion requires mechanical aid. Figure 8 shows the basic design of the pad mount. The part was drilled and milled at FirstBuild.

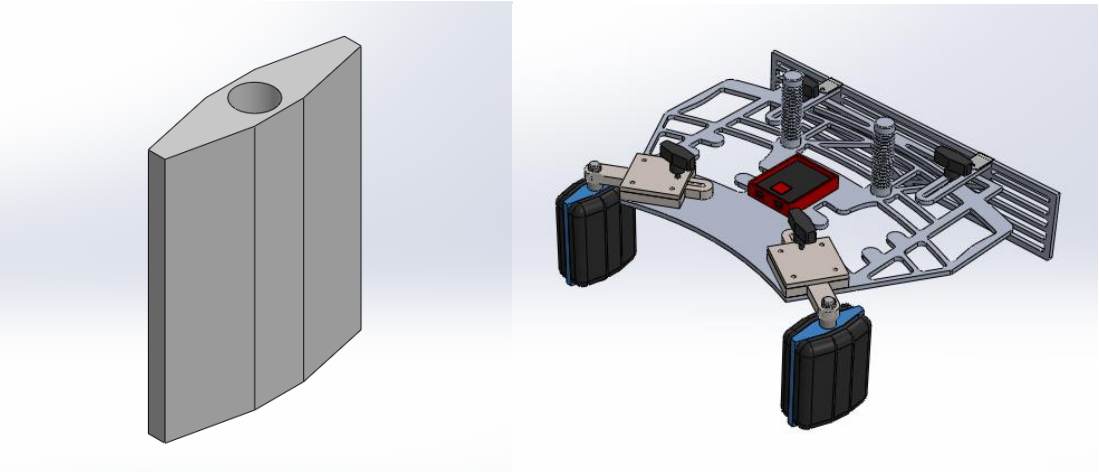

FIGURE 8 – The SolidWorks model of the pad mount part (Left) and the integrated model where the pad mount parts are highlighted blue (Right).

e. Ordered Elements.

Four components of the device were ordered from McMaster Carr: the brackets holding the knee plate, the knobs, the pins, and foam. The brackets hold the knee plate flush with the ends of the knee arms so that the device remains secure even as the user holds it to their knees. To adjust the two knee arms and the two pad arms, they must slide then be locked down. For the knee arms, the knobs tighten each arm in place via threaded hole in the top plate. For the pad arms, the knobs screw through a steel threaded hole and against the arm to hold the part. The pins are a significant element in withstanding and translating the loads in the device. Since strength was such an important factor, a steel

shoulder bolt was selected for the pin to allow the rotation of the pad mount and threads into the pad arm. It was important that the selected foam not over dampen the exercise nullifying potential results, soft enough for user comfort, be easy to clean, and be resilient. A 0.635cm thick polyurethane foam that is soft, flexible, and ultra-smooth texture was expected to meet parameters. Furthermore, an adhesive back was chosen for ease of application to the pad mount and itself. One side of the pad mount was doubled over providing a more comfortable option should a single layer induce discomfort.

f. Other Elements.

Several other pieces were required to support the functional elements and use of the device. Consequently, these required minimum design. Handles are valuable for comfort and alignment of the device on the lap during use. A simple 2.54 cm diameter rod with a threaded hole for securing it onto the plate was sufficient for the prototype. Texture was added via lathe for further grip enhancement and comfort. The pad arm holding plate covers the pad arm and has a threaded hole for a knob to secure the arm before exercise. Additionally, it has threaded holes to secure it to the spacers and plate. In order to maintain strength through the threaded holes, it was decided that the holding plate should be steel. Spacers were needed to elevate the holding plate to allow space for the arm to move. They are made of left-over aluminum bar stock form to be both resource and weight efficient. A knee plate was required to help the user find a starting point as well as prevent the device from pulling into the abdomen as the device is loaded. Initially, the knee plate was a simple plate matching the width of the first iteration top plate. The second iteration was lengthened to a matching 48.26 cm, has removed material in wide slots that match the movement of the knees, and rounded bottom corners for extra

safety as seen in Figure 9. Since the pads and pad arms were unadjusted, 48.26 cm remains enough width to not allow the knees to slip off of the sides as with the first iteration. An additional iteration was created in case the shown iteration requires additional reinforcement. It was not anticipated that additional reinforcement would be necessary. With minimum loading, the structure of the knee plate was believed to be sufficient.

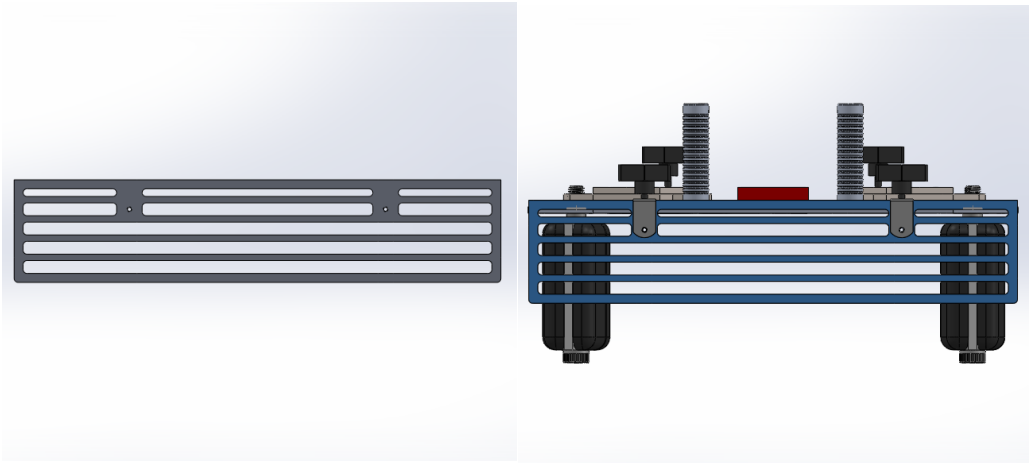

FIGURE 9 – The SolidWorks model of the knee plate part (Left) and the integrated model where the knee plate part is highlighted blue (Right).

2. Strength Analysis

Calculations and FEAs (SolidWorks Simulation, V2018, Dassault Systèmes Los Angeles, CA) aided in determining the proper design parameters to pass failure and safety specifications. A FEA is a method of testing the behavior of a 3D computer model under simulated real-world conditions. This is used in this analysis to simulate mechanical testing through design iterations prior to fabrication therefore saving time, resources, and cost. Critical elements of the device require analysis to ensure the desired functionality. To meet the demands of this mechanical device, bending and shearing

stresses were the focus of analysis for both single event failure and endurance failure over time.

a. Plate Analysis.

The top plate of the device is ultimately responsible for translating the input loads into the sensors on the top of the device. This does so by symmetrically flexing about the midline of the plate as the moment arm is moved from the pad arms to the plate after an abduction is performed. The plate needed to be thin enough to provide reliable feedback to the sensors but not be so thin it breaks. Due to the nature of accelerometer sensitivity, data filtration, and the plate being relatively thin aluminum, flexibility was not a concern while rigidity was when considering such high input loads. Calculations for bending stress were performed using Equation 1 where σ_B is bending stress, M is moment arm, y is the distance from the neutral axis, and I_A is the area of inertia for a rectangle. Bending stress is calculated about an axis on the plate which was then compared to the fatigue strength of the material yielded the part viability over numerous loading cycles.

$$\sigma_B = \frac{My}{I_A} \left(\frac{N}{mm^2} \; or \; MPa\right) \qquad \text{Eq. 1}$$

To calculate the bending stress about the midline of the prototype, the respective dimensions of the device were used. Perpendicular distance from the midline was overestimated to 13.97 cm at the maximum pad arm setting to provide extra precaution while the cross section at the axis was limited to the first gap in the plate. The force applied in the moment arm of the input was also overestimated at 1000 N to assume a worst-case scenario in which the user input is large and applied directly to the point selected for the perpendicular distance. A second calculation was later performed about an axis perpendicular to the arm while tangent to maximal stress geometry according to

the FEA with all other parameters the same. The third and fourth calculations were performed using the anticipated user force of 450 N applied 75% down the pad with respect to each axis used. Due to the complex geometry and transfer of stress across varying materials, an FEA was performed on the final iteration of the top plate to check the stresses at potential points of failure. The parameters of this were similar and extreme as in the manual calculations. Symmetry about the midline was used with a fixed geometry at the far edge of the symmetry while the effective loads of 1000N and 450 N were applied to a simplified pad pin. 6061 aluminum material settings were used on the plate for these FEAs. A solid, curvature-based mesh was used with 19100 to 21893 elements of 7.9 mm maximum size and of 1.6 to 3.2 mm minimum size.

b. Pin Analysis.

The pin receives the most direct load after the impact generated from the user into the pads. Due to the pin screwing into the pad arm, analysis was needed to ensure that it is strong enough to handle the stresses without failure. The pin must also be rigid enough to translate the load into the arm to then go into the plate to be detected by the accelerometer. Since the pin is steel with a shoulder tangent to the arm, the concern was failure. Two modes of analysis were used: principal stress analysis and a FEA analysis. For the principal stress analysis, the cross-sectional area of expected failure would be the minimum diameter of the threaded section of the shoulder bolt. The force anticipated by the average user was 450 N (Osbourne, 2017). However, an undampened overestimate of 1000 N was applied 14 cm away at the very bottom of the shoulder bolt assuming a 6.7 mm radius where the pin receives the stresses. Using the previous bending stress equation

and Equation 2 for shear stress below where τ_{Max} is the maximum shear stress, S is the shear force, and A_{Circle} is the area of the circle in the cross section of the neck.

$$\tau_{Max} = \frac{4}{3}\left(\frac{S}{A_{Circle}}\right) \left(\frac{N}{mm^2} \; or \; MPa\right) \quad \text{Eq. 2}$$

Both bending stress and shear stress were calculated before being utilized as inputs for Mohr's circle as per Equation 3 to find the principal stress at the location of interest where σ_P is the principal stress, σ_B is bending stress, C is the center of the Mohr's Circle, and τ_{Max} is the maximum shear stress. The distance from the shoulder at which the endurance limit is reached with expected force application was then similarly calculated.

$$\sigma_P = \sqrt{(\sigma_B - C)^2 + (\tau_{Max})^2} + C \;\; \left(\frac{N}{mm^2} \; or \; MPa\right) \quad \text{Eq. 3}$$

The FEA of the pin was performed in SolidWorks using a simplified pin with accurate relevant geometry with the same force inputs. Furthermore, another FEA-specific part was used to allow compression and tension in the pin without relocating nor amplifying stresses for accuracy. This part was aligned to receive compression on the opposite side of the pin receiving the load. In preparation for the test, the simplified threaded region of the pin and the flat at the bottom of the FEA-specific part were set as fixed geometry to accurately simulate how the stresses travel through the pin and arm. A displacement profile was evaluated to identify how and where the stress loads into the pin. Constraints for the assembly with fixed geometry and loading are seen in Figure 10. Testing was set up by applying a force to the flat of the pad mount. A 2000 N force was used to compensate for the distribution of the load to resemble a 1000 N load applied at the bottom of the pin. Alloy steel material settings were used on the pad pin for these

FEAs. A solid, blended curvature-based mesh was used with 20845 elements of 2.8 mm maximum size and of 0.9 mm minimum size.

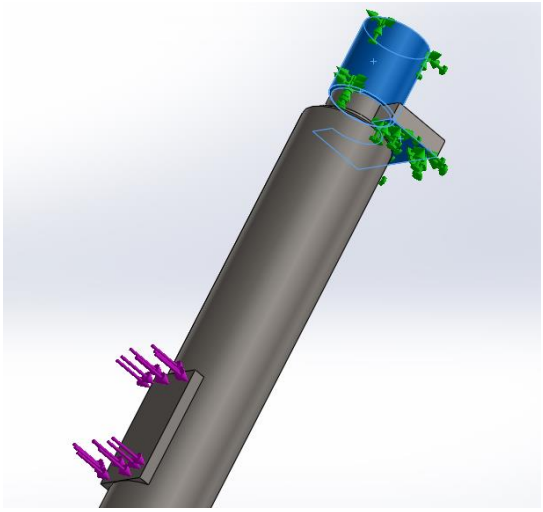

FIGURE 10 – The assembly of the simplified pin and FEA-specific part where the purple arrows indicate force loading while the green arrows on the blue highlighted surfaces indicate fixed geometry.

B. Performance Experiment

1. Sensors

Critical to analysis is data collection. Several factors such as sensor location, equipment specifications, and calibration influence the results. The location for mounting a sensor was first parameterized via objective and input. Utilizing a strain gage and accelerometer, bending and vertical motion were most valued. Strain is easily measured even with small amounts of bending by a strain gage. This bending could then be used to observe Z-axis acceleration trends as a potentially simpler alternative to validating exercise effectiveness for the user in future work. Later in the study, acceleration data was frequently analyzed in terms of jerk: the rate of change in acceleration with respect to time. It was hypothesized that the proximal portion on the midline of the top plate is a reliable and repeatable placement due to its symmetry and anticipated torque generated

by the exercise. To ascertain this, a FEA was performed on an early iteration of the top plate. The early iteration was believed to be verified by its similarity to the final iteration especially within the objectively functional region of the top plate.

2. Procedure

To test the effectiveness of the device and translate proper feedback to the user, the appropriate set up was necessary. The strain gage was mounted in a location that would maximize its induced change in potential across the bridge via bending in the plate at any arm setting. Maximizing the strain for the gage via placement ensures meeting the reading threshold and increases output sensitivity. Along the midline of the device was where the strain gage was placed as this was where a large amount of left-right averaged plate bending was anticipated. An FEA of an early plate iteration was performed with symmetry about the midline and fixed geometry at the far edge of the symmetry while a load was applied to the simplified pad pin. 6061 aluminum material settings were used on the plate for this FEA. A solid, blended curvature-based mesh was used with 14597 to 14933 elements of 11.5 to 12.1 mm maximum size and of 2.3 to 2.4 mm minimum size.

Determining the type of gage circuit was also critical due to its sensitive nature. A Micro-Measurements 120 Ω quarter-bridge circuit was selected as only a single bending axis was needed. This gage utilized an excitation voltage of 5 V and a gage factor of 2.11. Furthermore, there was no worry of thermal shifting with time as the device was assumed to be stored and used at room temperature by nature. However, the calibration of the gage equipment itself was performed utilizing a 120 Ω half-bridge circuit. A control 120 Ω 1% resistor was mounted to an aluminum bar to complete the half-bridge circuit. Once mounted via protocol in Appendix III, the sensor's ability to send and receive input was

verified on a Vishay 2100 Strain Gage Conditioner and Amplifier System. The voltage accuracy was tested by applying a known load at a known point on the bar and comparing the experimental voltage output to the theoretical output. A balanced output indicates that the sensor and wiring are effective and functional. Once achieved, it was confirmed that the experimental and theoretical voltage outputs were similar and therefore functional. An ADXL335 three-axis accelerometer was also used with a maximum acquisition rate of 550 Hz for the Z-axis.

Sensor calibration on the device must be performed by simulating the intended use under known conditions. The parameters to be met were based on the work of Osbourne, 2017 in which the device was mounted to a materials testing system (MTS) which is responsible for testing how materials behave under various loading conditions. An MTS Bionix 858 Test System was used to quasi-statically load the device at the pads. The mounting protocol can be found in Appendix IV. One user to the next was expected to have different strength. Furthermore, an increasing load up to approximately 600 N outward was applied to mimic user abduction. Force was achieved via increasing the height of the machine between 10-12mm.

Quasi-static calibration testing must cover independent parameters evaluating the influence of each on the strain gage given force into the pads. It was expected that varying user anthropometry affects how and where the proximal femur impacts the device. Consequently, the height on the pad where impact occurs may influence the bending moment via a difference in perpendicular distance at a given force. Pad arm lengths were also tested for any potential effect on the plate strain at a given force. The pads were tested narrow, average, and wide as well as at the low and medium heights on

the pad for each arm setting. It was reasoned that the greater trochanter of the femur would not likely reach the top of the pads due to the soft tissue and muscle tissue height of the user, so it was not studied. Cumulatively, these inputs provided a universal calibration curve between strain gage output and pad force through the range of user settings. Later, this could be manipulated to generate the metrics of interest. It was hypothesized that the data would be linear indicating proper function.

A portable electronic circuit communicating to a custom LabVIEW program via a custom serial microcontroller firmware (Arduino UNO, Arduino.cc) was required for data acquisition and processing. The function of this hardware was to integrate accelerometer data with the strain gage data through an analog circuit and microcontroller capable of recording data with an appropriate acquisition rate. Parameters for the software and hardware to synergize were reviewed and manipulated to ensure that data acquisition from both inputs were also in sync and fast enough to meet testing needs. Maximum collective acquisition rate for all of the hardware was determined to be 500 Hz. Ultimately, an acquisition rate of 250 Hz (one sample per 4 ms) was used in the software while the strain signal amplification was x 205. The signal Figure 11 shows the both the hardware and an example software output.

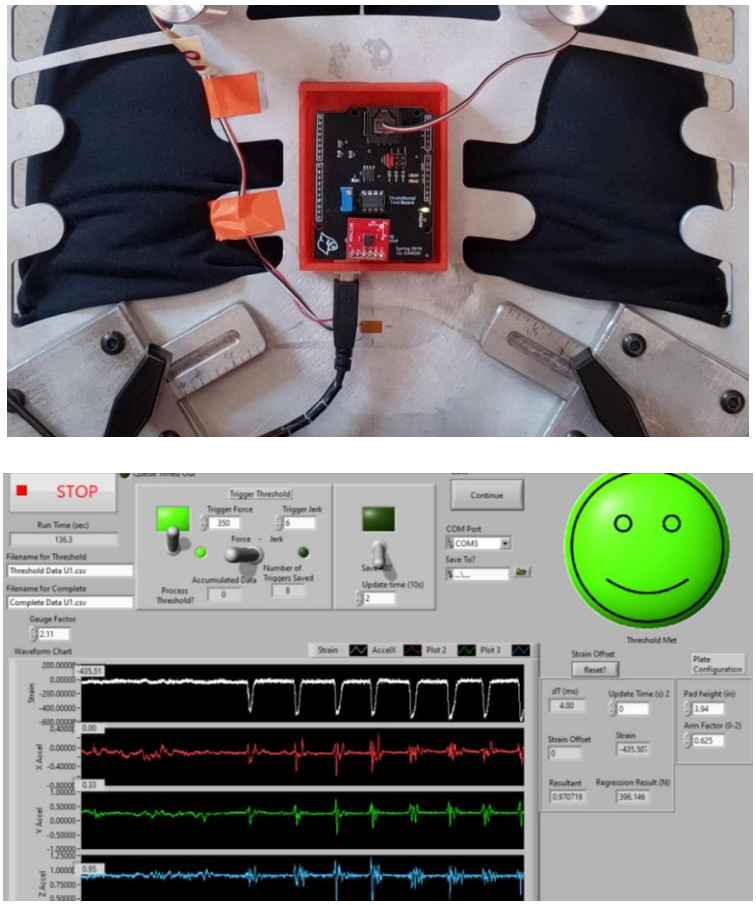

FIGURE 11 – The mounted data acquisition hardware (top) and example live output from the GUI (bottom).

Throughout the process of refining data acquisition programs and compiling hardware, preliminary data was collected to present large-scale trends as well as diagnose issues with the device or software. At this point, the strain hardware had been validated to be functional and accurate while the accelerometer had been proven functional. While acquiring the data, the known software issues were duplicate time stamps for both sets of data and an acceleration baseline shift. Stress and acceleration output data were recorded live but were truncated and transcribed into an Excel file without timestamps as a 3 second interval of data around an achieved threshold of strain. This translates to a qualitatively interpolated user force output based on previous FEA and calibration data

which was necessary to achieve the beneficial strain rates in the bone. For the first iteration, fourteen trials were performed, however, the first two were left out of the preliminary analysis having not been properly performed and recorded. The remaining data of the twelve runs were assigned time then qualitatively assessed for consistent trends and relationships of stress magnitude and acceleration through the interval of interest.

A second iteration was performed similar to the first with proper strain output in terms of micro-strain. Twenty-three repetitions were recorded and filtered based on a strain greater than 300 με as well as proper performance. Results were further evaluated to refine software needs and discover data trends. Only one more iteration of preliminary dynamic data acquisition was recorded using the undated hardware and software later used in final testing. The user performed 23 repetitions of which 12 met analysis criteria. The data from the final iteration was analyzed independently as well as compared to previous data.

With the new hardware and programming, a second calibration similar to the first was performed to ensure validity. These data would be recorded at discrete increments of 50 N from 0-1000 N for simplification and comparison in the statistical analysis. Factors assessed during this test again include the arm setting and the loading height on the pad. These settings were created at measured points for accuracy as seen in Figure 12. Pad arm length was tested at minimum, central, and maximal lengths while the pad height was tested 50%, 75%, and 100% down the pad at each arm setting. Strain was zeroed at

100 N of loading to remove any bending output due to gravity while the prototype was loaded to be held in place. As a result, the output was change of micro-strain. Linearity again determined proper function of the sensors and device. Inherent offset due to testing methods was removed for each setting based on a second order best-fit line as generated by Microsoft Excel. This data then provided true micro-strain versus change in micro-strain. Based on the new, true strain over force graphs, a best-fit regression was made to verify any significance in user factors as well as to aid in dynamic data analysis. The resulting equations were used in order to accurately read dynamic testing data on a user-specific basis by interpolating the slopes.

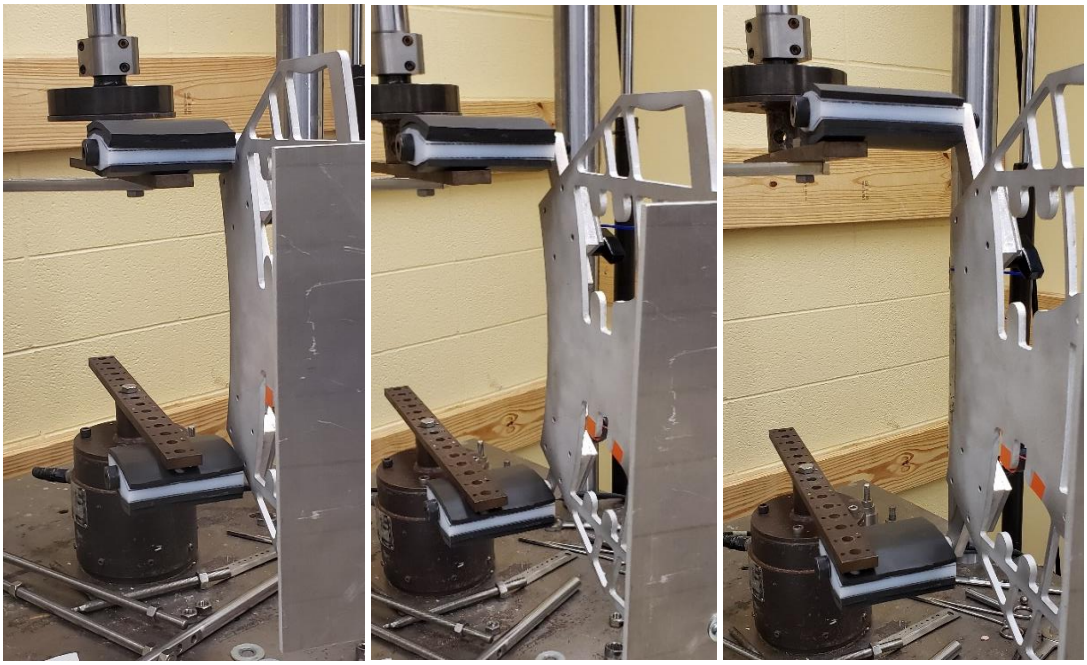

FIGURE 12 – Example mounting of the prototype into the MTS Machine for quasi-static loading at minimum arm length with 50% pad height (left), central arm length and 75% pad height (center), and maximum arm length at 100% pad height (right).

An equation was manually created based on the slopes and changes therein of the calibration data was attempted to no success. Utilizing Minitab 19, several regression equations were generated then compared in Microsoft Excel. Force was provided by

strain gage input, an arm factor value for the pad arm setting, and pad height as this was how the dynamic data will be generated in its testing. Regressions were modeled as a best fit regression at a 95% two-sided confidence interval. All terms listed above were added as continuous predictors. The terms were also coded via standardization by subtracting the mean and dividing by standard deviation for comparison of significant terms within the polynomial model to fit the known set of data. The first model was a first order regression. Higher order regressions were performed: the second model including terms through order 2 and the third model including terms through order 3. All models include interactions through order 3. A four-in-one plot was also produced for model verification. Another regression equation was generated for models with terms that require elimination via P-value greater than alpha. Random strain gage input was created by a random number generator through the anticipated accepted user input range of 300-600 με in bins of 100 με. Each number was assigned a tested setting allowing verification across each combination of settings. Accuracy and precision of the two polynomial equations were evaluated by error margins and standard deviation of the population when calculated against a second-order interpolation was generated from the calibration data in Excel. The selected equation was further tested against randomly generated continuous values and was compared to interpolated values across the collected data settings for validity. Upon approval, the regression was added to the software and tested at multiple levels to verify accuracy and functionality in use. Manual input units were simplified for ease and speed of user settings. Pad height regression input as a percent value was then calculated based on an inch measurement from the bottom of the plate to the center of the greater femoral trochanter. Pad arm length remains coded and labeled on the pad arm.

Furthermore, the knee arm was labeled for user set up but was not relevant to force output. These markings shown in Figure 13 were used for clear, consistent measurement based on unique user morphology for GUI input.

Following the second calibration, the device was dynamically tested by volunteers to reflect the potential effectiveness of the device as well as identify force to movement trends. Arm factor, abductor drive, handle grip, and knee length, metronome, and padding were tested by setting to review their importance and impact on pad force. For arm factor, a single volunteer was selected to perform through a range of pad arm settings with all else being the same. User one performed eight reps per setting from 1 to 0.375 in 0.125 increments. Average maximum forces per each setting were accumulated and plotted. To test how the hip abductors influence force and movement curves, four reps of four instructions were performed by a user. Having the user perform reps with no specific drive in mind, a quick hit and reset, abducting to the pad, and abducting through the pad provides information on trends. Similarly, four reps of five instructions for handle grip with all else the same were performed. Data was collected and plotted for the volunteer pulling the handles toward them, pushing down into the lap, a relaxed grip, minimum grip, and squeezing the handles. Knee arms were tested in ¼” intervals from 0” to 3”. Four reps per setting were performed with all other settings being equal. Trigger force was kept low at 150 N for appropriate sensitivity. Metronome testing was performed from 40 Hz to 140 Hz in 20 Hz increments to an audible metronome. A random number

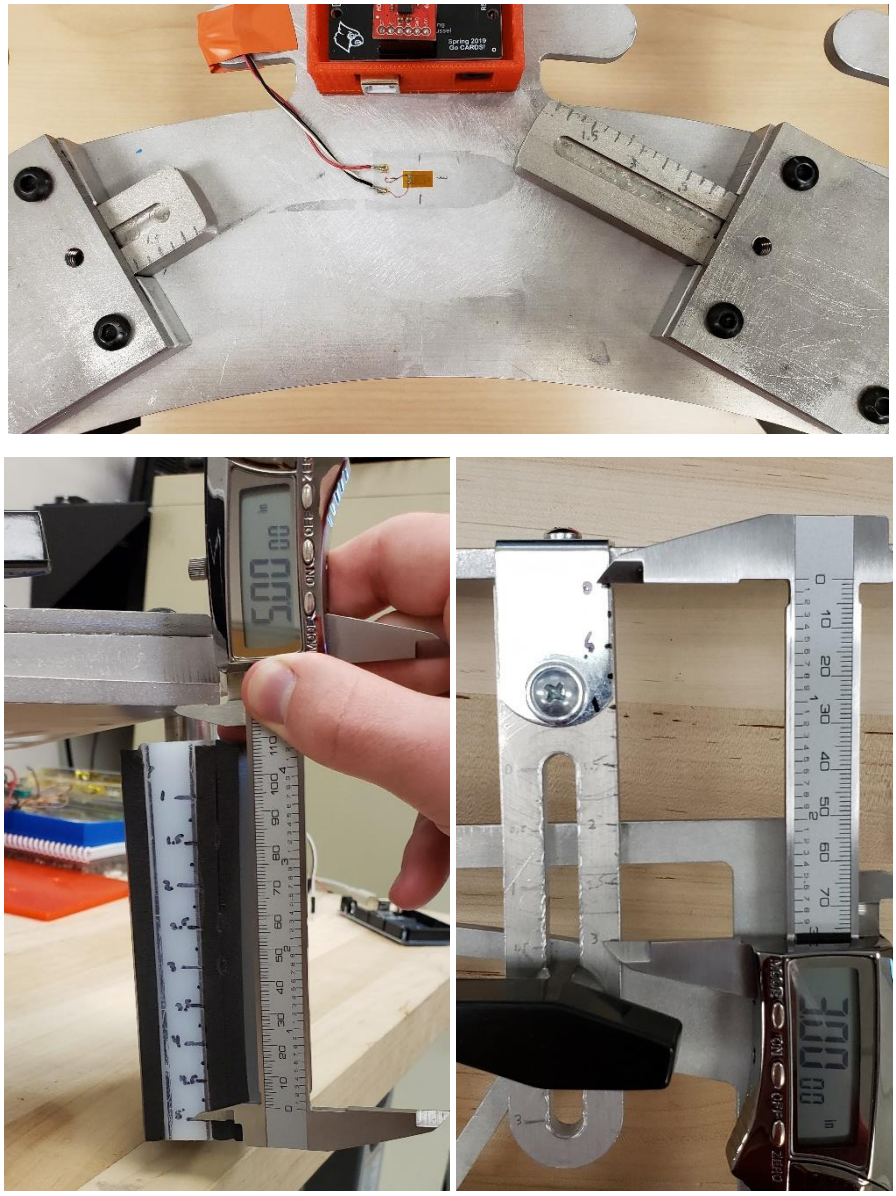

FIGURE 13 – Morphology markers for user setting and software input of the pad arms (top), pad height (bottom left), and knee arms (bottom right).

generator was used to eliminate fatigue as a factor. The resulting order of beats per minute was: 140, 40, 100, 80, 60, and 120. Eight repetitions per set were conducted. Recording and processing the data utilizing the threshold feature was limited over 104.5 beats per minute due to the code of the trigger timer. Consequently, the 100, 120, and 140 beats per minute trials were manually filtered from the complete recorded data. Upon

beginning each trial, a brief period of abductor activation was performed to the frequency of the metronome before full reps were performed and recorded in order for the user to acclimate to the respective demand. The strain and acceleration data were then collected and plotted to analyze trends in user performance of repetitions. Testing the padding sides was performed for both quality of output as well as user comfort. Fitting the user to their single padding settings was first done as a standard that was then kept constant for equal comparison. Each trial was performed at 10 repetitions per set. After completion, the prototype was placed on the user with mixed pads to further evaluate comfort.

Throughout varying stages of testing these influences, 10 volunteers perform 10 adequate repetitions as described in the following for analysis. Of these, 5 were female and 5 were male. All but two male volunteers were in their twenties by availability. It was assumed that rep performance in this study would strongly correlate to future testing among anticipated users. Volunteers were first informed of the process to-date and receive oratory permission to touch the hip as needed to acquire measurement input. The beginning step for the beneficiary was having their legs together with the knee plate properly adjusted against the knees while the top plate was against the abdomen. Proper pad adjustments must be made to ensure that the exercise would benefit the user. This was performed by first finding the greater trochanter of the femur to ensure that the pin was slightly distal during performance. Here, it was also important to ascertain that the pads were shifted down onto the head of the pin to later properly note setting measurement for GUI input. Being slightly distal to the acetabulum ultimately generates the three-point bending in the femur to successfully deliver strain. Ensuring that the pad arm setting was narrow enough to achieve high loading was ideal. User settings of arm

factor and pad height were added to the GUI so that live force could be provided from strain conversion via the regression equation. Comfortably gripping the handles, the user then performs a swift abduction against the pads as illustrated in Figure 14.

FIGURE 14 – A top view example of an abduction performed from the starting position (left) to the peak abduction into the pads (right) where the blue represents the approximate motion of the femur about the acetabulum.

An Arduino was used to collect and send the feedback data to LabVIEW where it was decoded and processed upon achieving a set minimum force threshold of 300 N. 300 N was selected as an acceptable minimum buffer to the 350 N suggested value based upon the previous work in Osbourne, 2017 in order to ascertain adequacy of a repetition. From LabVIEW, the data was exported to Microsoft Excel for further analysis. In the Excel analysis, a 7-point moving window average filter was selected for smoothing the data. Peak force was collected from the raw data while peak force rate was collected from the filtered data. Throughout the process of collecting volunteers and taking dynamic data, peak force rate calculations were updated to central difference derivatives for the last four volunteers. Peaks are reduced from the filtered data, therefore the force rate data was performed to a backwards difference derivative to be consistent with the earlier data. All strain and force data were recorded in a consistent manner allowing the data to be

comparable. The peak pad force rate was then converted to peak strain rate in the bone via an extrapolated conversion factor of approximately 3.36 N/με from the in-situ cadaver outcome of 1511.3 με at 450 N (Osbourne, 2017). This number comes from validated cadaveric testing of abduction into a first-generation prototype while measuring force and femoral neck strain rates. Average peak force and average peak strain rate of each user were accumulated for device performance evaluation of its ability to achieve and detect adequate forces expected to stimulate osteogenesis in the proximal femur.

III. RESULTS

A. Prototype

Fabrication and assembly of each component was performed to create a testable prototype to be used through the remainder of testing. Figure 15 is the complete modeled assembly and fabricated prototype used in all dynamic data collection. Adjustability and rigidity were achieved while the final iteration top plate was 33.2% lighter.

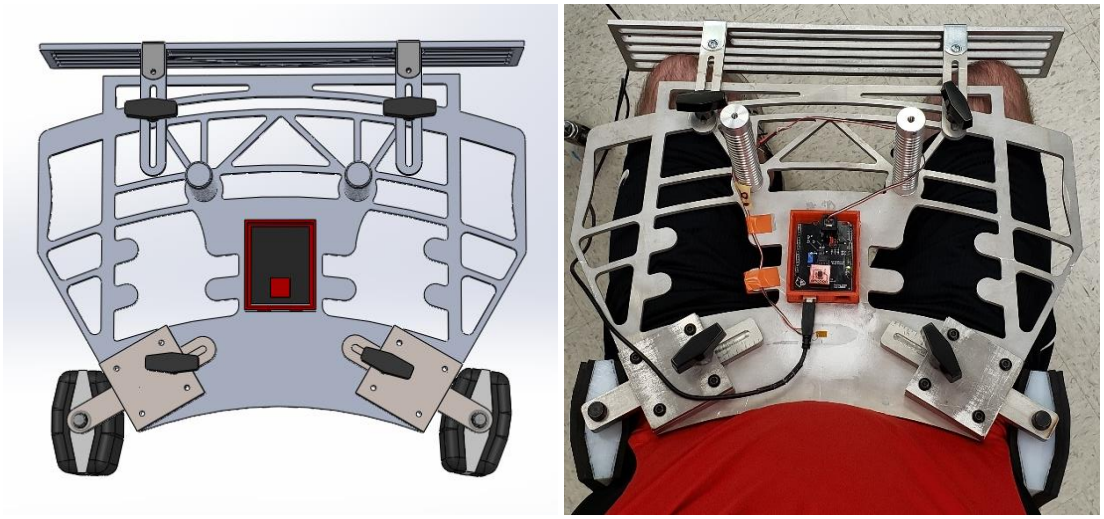

FIGURE 15 – A final SolidWorks assembly of the device (left) next to the functional prototype on a user (right).

Plate calculations were performed to ensure the integrity of the prototype. A first calculation of the bending stress about the midline with an overestimated 1000 N load resulted in a bending stress of 99.4 MPa which is well under the tensile yield strength of 276 MPa nearing the endurance limit of 96.5 MPa (MatWeb). Calculating bending stress about an axis perpendicular to the arm with the same large load for the second calculation

yields 168.9 MPa which is again below the yield strength but above the fatigue limit of 96.5 MPa. When evaluated utilizing the average expected user impact of 450 N at 75% down the pad, the outputs were merely 33.7 MPa and 57.0 MPa to the respective axes which are both below the endurance limit. These theoretical values were expected to be higher than the actual values the device would experience during use due to the excess, neglected geometry of the device. These calculations can be found in Appendix V.

FEAs were also used to evaluate the stresses in the top plate. Two iterations at 1000 N and 450 N were run for analysis. In the 1000 N test at the bottom of the pin, a maximum stress of 223 MPa was the result. This is below the yield stress of the plate. When run with the average anticipated user input of 450 N at 75% down the pad with all else equal, a maximum stress in the plate of 84 MPa was found. Here again, the value is below both the yield stress and the endurance limit. Each FEA output is shown in Figure 16 below.

Pin strength calculations were also performed. To find the principal stress in the neck of the pin, bending stress and shear stress calculations were first performed. Stresses of 675.1 MPa in bending and 10.4 MPa in shear were calculated. Using these as inputs for Mohr's circle, the principal stress was calculated to be 675.3 MPa. Pin calculations can be found in Appendix VI. The tensile strength of the pin is 965 MPa making the pin strong enough to withstand an abnormally strong impact. Consequently, the endurance limit of the metal was assumed to be about 322 MPa. The distance down the arm that the user would have to apply the anticipated average load of 450 N was evaluated for safety

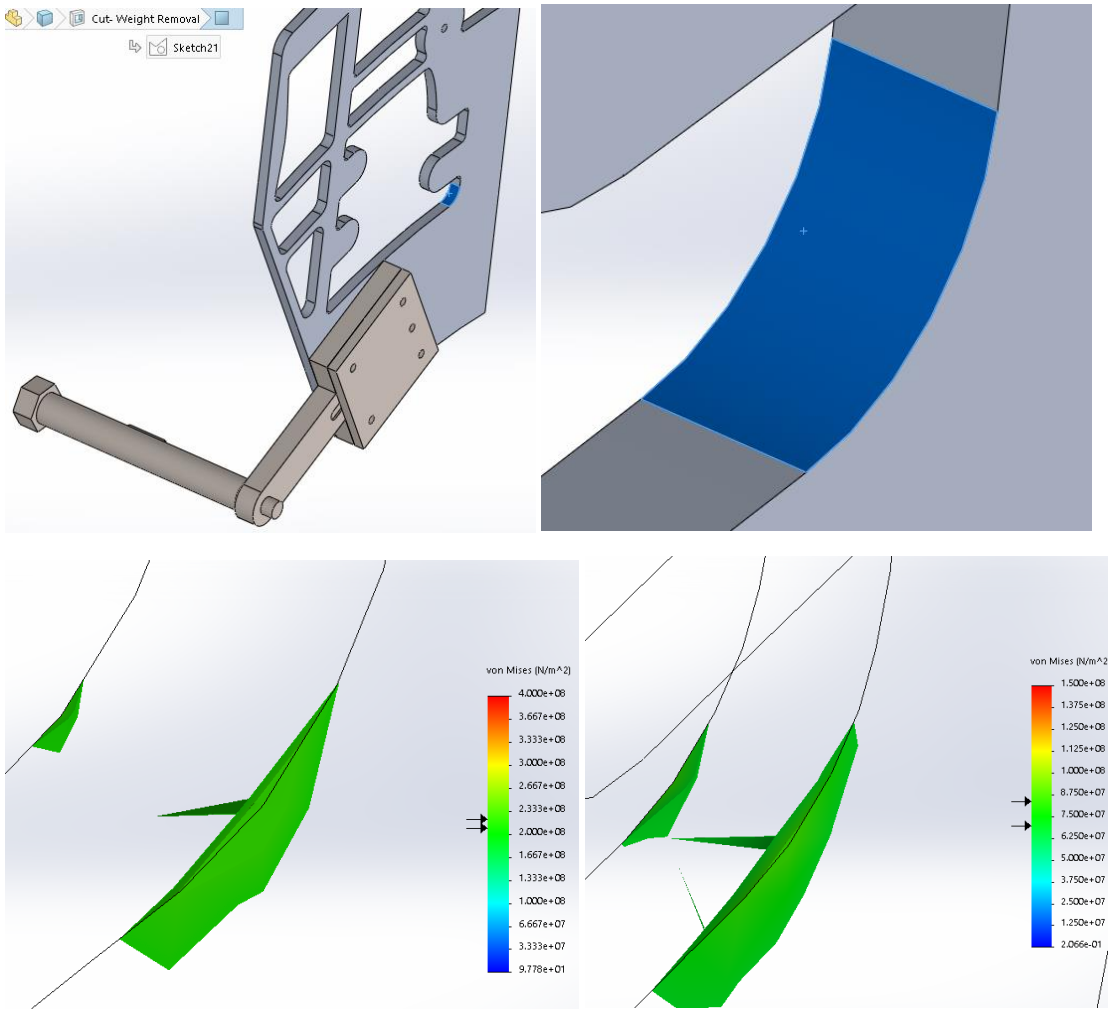

FIGURE 16 – The location of maximum stress in the plate under SolidWorks FEA loading (top-left), the magnified location of this stress where the blue plus indicates the side under tension (top-right), iso-clipping of a 1000 N input at the bottom of the pad from 210-223 MPa (bottom-left), iso-clipping of a 450 N input 75% down the pad from 70-84 MPa (bottom-right).

with long-term use. In order to reach the endurance limit, the load would have to be applied 147.3 mm (5.8 inches) down the pin – past the shoulder of the pin – indicating that the pin will endure. Additionally, the pin was expected to be stronger chiefly because of pin shoulder contact with the pad arm which should reduce the loads on the threaded cross section. However, the shoulder did not make contact with the arm upon assembly due to the fuller where the neck meets the shoulder leaving all of the stresses in the neck.

Similar to the plate analysis, a FEA of the pin was also utilized. A displacement profile was first generated as seen in Figure 17 revealing bending in the neck thus generating high stress in the neck. This also verifies that the neck would be the likely point of failure. Further stress analysis evaluates the maximum magnitude of stress in the neck That could lead to failure. The maximum tensile load was found to be just above 830 MPa in the thinnest cross section area of interest where it would fail as seen in Figure 18. While higher than the calculated principal stress, it is still below the maximum tensile stress of the pin. Similarly, maximum stress under an expected load is calculated to be only 280 MPa which is below the endurance limit of the material. Consequently, the pin was expected to hold up to unusually high magnitude stresses.

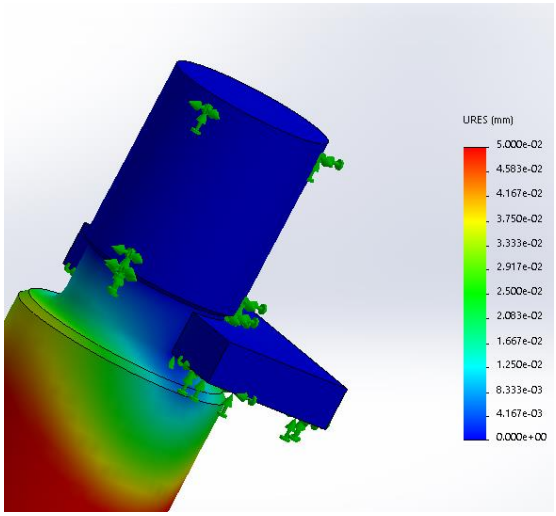

FIGURE 17 – A magnified view of the neck with a displacement profile revealing where the tensile stress at the base of the neck is highest in green.

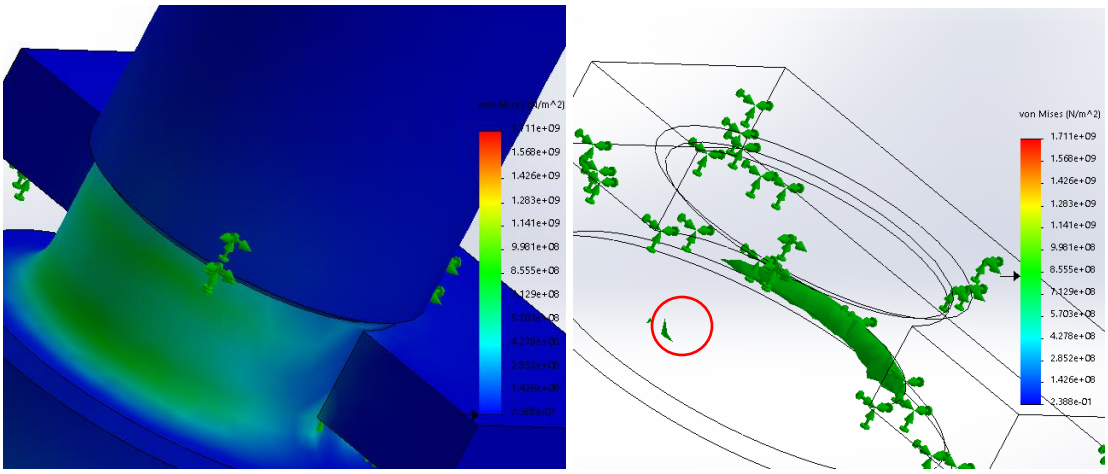

FIGURE 18 – Unfiltered FEA of stress in the neck of the simplified model pin (left) and filtered stress leaving everything above 830 MPa in green revealing a small, maximum amount of tensile stress on the neck circled in red (right).

B. Experimental Data

Strain gage placement was analyzed to ensure sufficient strain and to maximize output. An ideal location for the strain gage was decided upon by analyzing the FEA stress profile in Figure 19 within the measurable strain range of the gage. The location of this about the midline was approximately 6.5 cm away from the near edge of the plate where there is consistently high stress and bending. This was where the gage was placed. Next was ensuring proper gage performance on the plate under anticipated loads. This

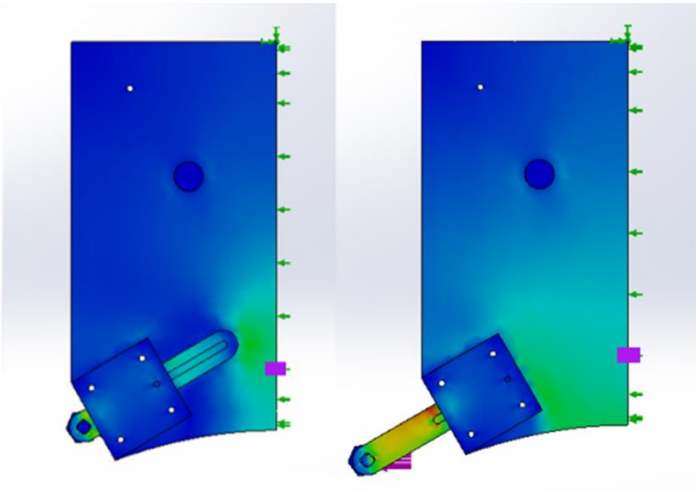

FIGURE 19 – An early design iteration FEA stress profile at the minimum (left) and maximum (right) arm positions where the purple indicates the approximate placement of the strain gage for use in testing.

was confirmed from the via linearity test in Figure 20, the first quasi-static calibration was performed. Strain data output for this test was in volts as the MTS Machine height was adjusted from 0-10 mm. Microstrain was calculated based on the voltage output and plotted over force. Despite a limited force range from the limited height change, a linear voltage over force graph in Figure 21 indicate the proper function and of the sensor while the slope indicates the degree of influence that the setting has on the strain in the plate. Appendix VII shows the complete set of quasi-static graphs. A second calibration performed later will properly analyze the relationship between force and micro-strain. However, we were able to move forward into preliminary dynamic data.

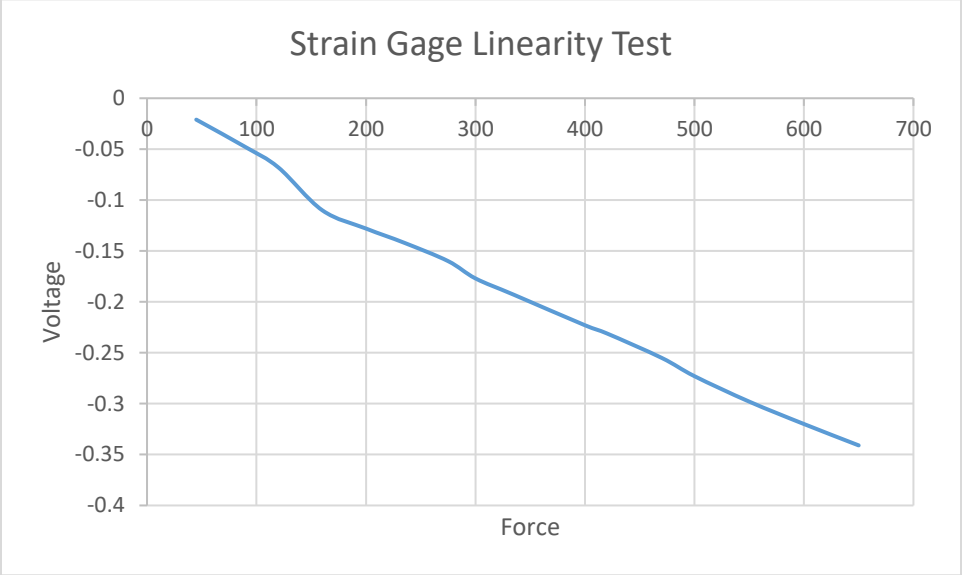

FIGURE 20 – A linear voltage over force output verifying proper function of the strain gage on the prototype.

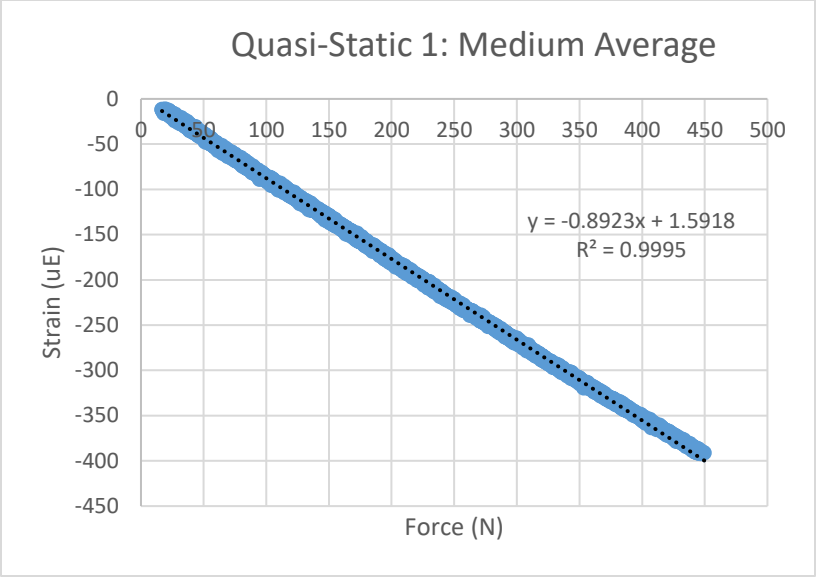

FIGURE 21 – An example of a linear quasi-static output in microstrain at the medium pad setting and average arm setting as the prototype was stretched about 10 mm.

After the first iteration of preliminary dynamic data acquisition, it was discovered that what was supposed to be the strain output was not yet converted to strain in the software. Consequently, software revision was performed before any data could be analyzed. Upon revision, the data of the second iteration was able to be read and manipulated. All dynamic data was graphed with a moving window average filter of 7 data points for smoothing without over dampening. Figure 22 below shows collective data and an example of the strain magnitude data and acceleration data by rep compared by time. Qualitatively assessing the trends to make a connection between strain and acceleration, it was noted that the moment at which peak strain within each event appeared to correlate positively with the largest slope in acceleration. Jerk at each point was then derived from the change in acceleration data over 10 ms also seen in Figure 22. Each rep of the accepted second preliminary data can be found in Appendix VIII. Due to this common

occurrence, jerk was chosen to be used as a factor for future analysis and iterations to be correlated with the peak pad load or pad loading rate for each repetition.

With the updated hardware and software, the third iteration reveals trends that were representative of what was expected in the final dynamic testing. Strain and acceleration charts were made of the data collected of all repetitions as seen in Figure 23. More variance was seen in this set of data particularly in acceleration. Additionally, there appears to be a consistent offset of about 100 με. Plotting the most unusual reps, it appeared that peak jerk was still an accurate indicator of peak strain. An example of this is found in Figure 24 while the complete set of graphs can be found in Appendix IX. Despite more variance in this iteration, there still appears similarities in trends. As a consequence of this preliminary testing, the software and hardware were believed to be sufficient for data acquisition in the final dynamic testing. Strain, acceleration, and jerk will be the focus of the final dynamic testing.

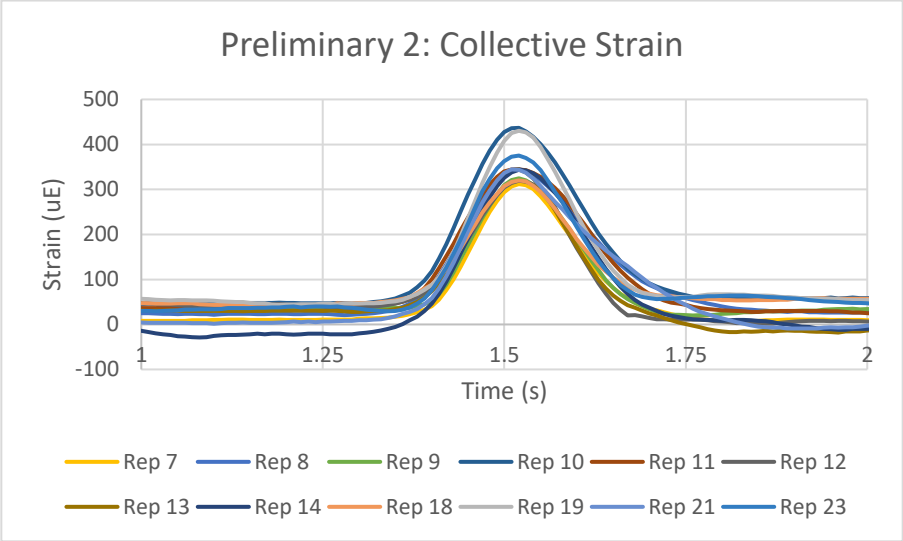

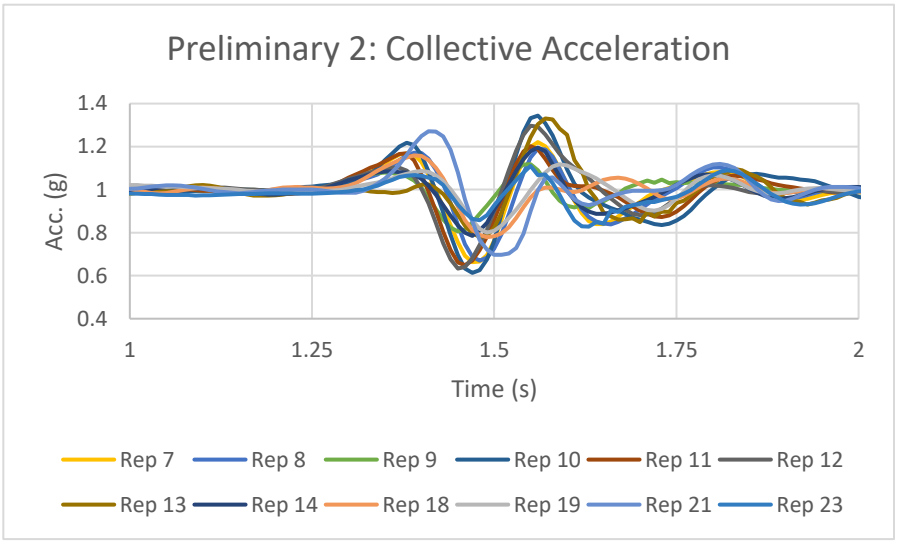

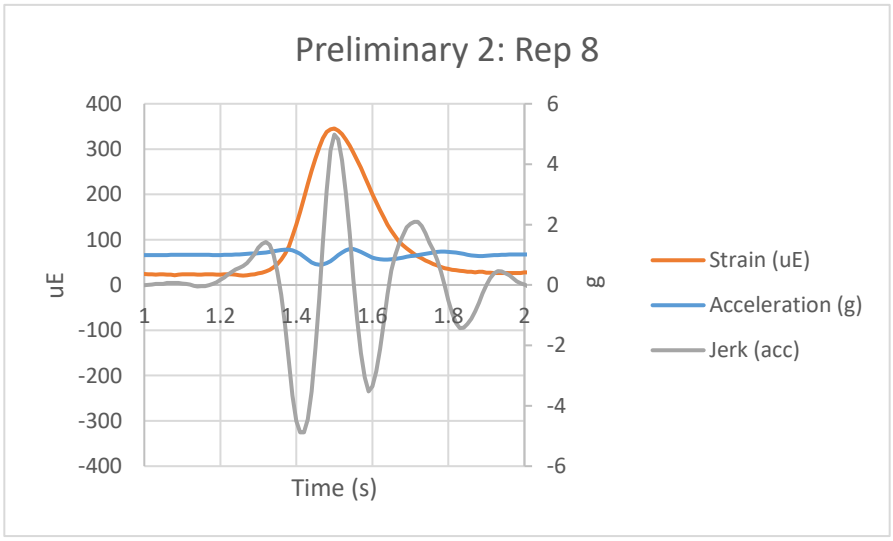

FIGURE 22 – Preliminary data of collective strain (top) and acceleration (center) for the qualifying reps as well as a single-rep example with added jerk curve (bottom).

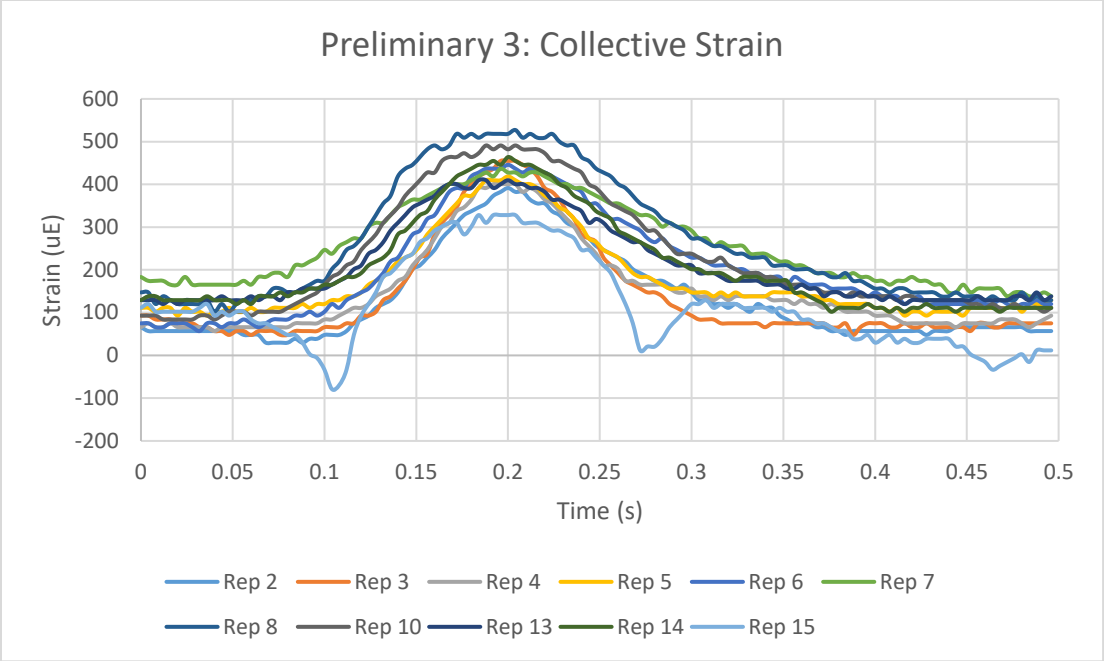

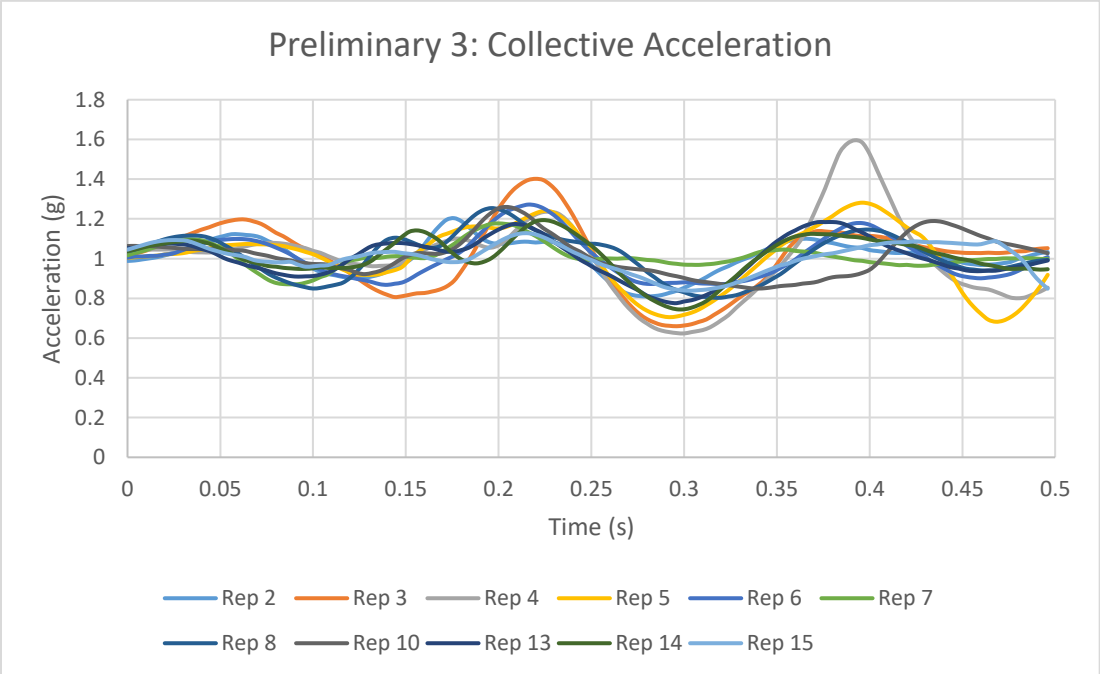

FIGURE 23 – Third iteration of preliminary data displaying collective strains (top) and collective accelerations (bottom).

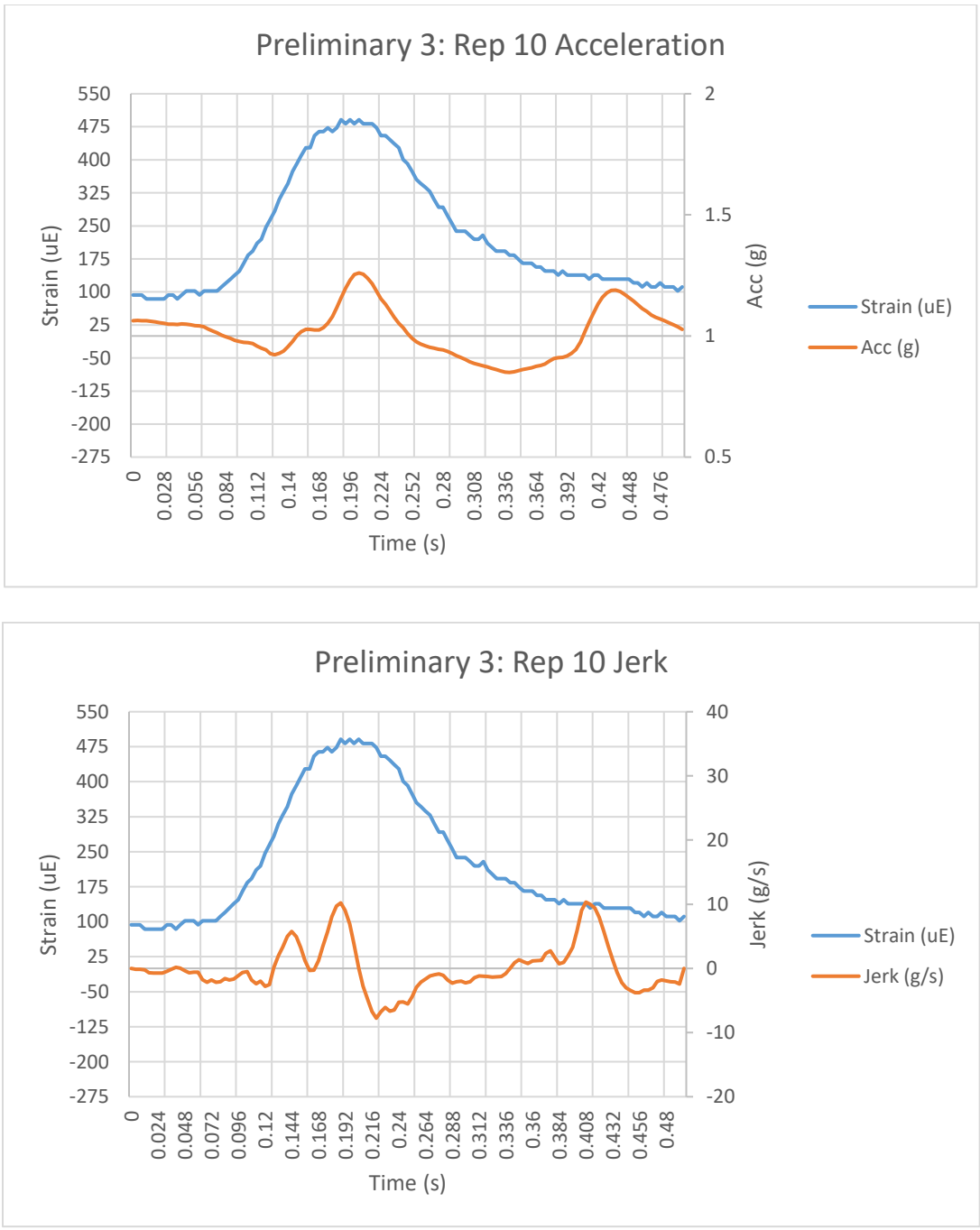

FIGURE 24 – Third preliminary data examples of the strain of a qualifying rep with both acceleration (top) and jerk (bottom).

Utilizing the updated hardware and software, the quasi-static test was again performed. One data point was missed in the recording processed at 700 N on the In 100

setting. All of the με/N graphs appear to be very linear as exemplified in Figure 25. Also exemplified in Figure 25, the R^2 values of the second-order trendlines were high. The entire set of graphs is displayed in Appendix X. While largely linear, there was a slight, steady belly through the 300 N to 600 N range which becomes important during the first order regression analysis. Furthermore, at 900 N the strain appears to become less sensitive to change across all data.

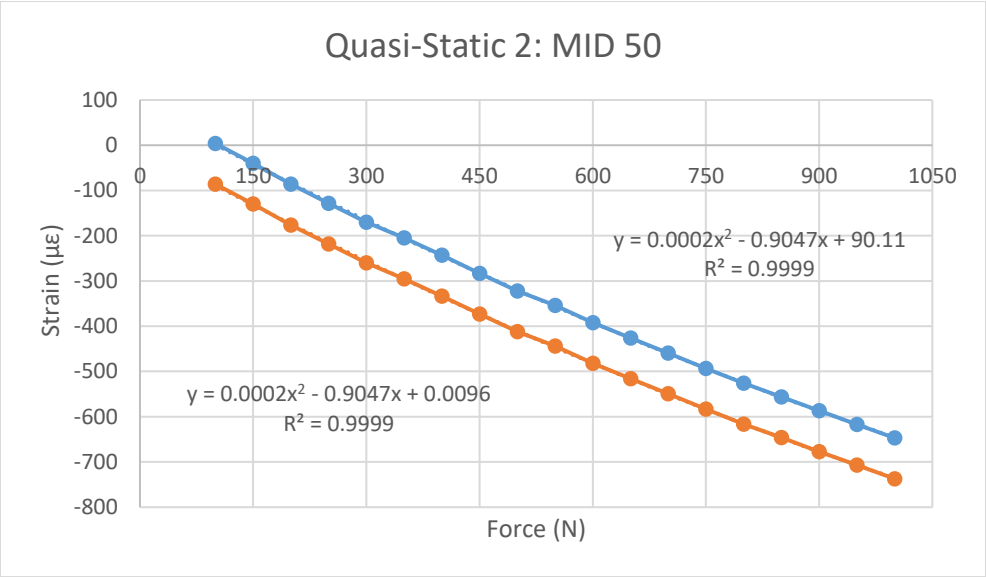

FIGURE 25 – Example data from the middle arm setting and 50% down the pad where the blue is the recorded change in strain data while the orange is the true strain without offset due to zeroing.

From this data, regression models were generated to accurately assess pad and hip loading during dynamic testing. The goal of finding an optimal regression was to obtain the highest accuracy output of pad force based on live strain gage values during use at any set of user settings. This pad force output of the regression could then be used to calculate force over time before being converted to the crucial theoretical bone strain rate metric based on the first-generation data. A manual regression was first attempted to high accuracy but was limited by its discrete nature. Minitab 19 analysis provides first, second,

and third order regressions from the quasi-static data. A second iteration of regressions was required due to the first neglecting offset prior to modeling. The third order microstrain term was eliminated from the third order regression and run again before use as a result of P-value greater than 0.05. Below in Figure 26 are the four-in-one residual plots of the regressions. From the first order regression, despite an R^2 of 99.50%, in the four-in-one residual plot the normal probability, versus fit, and histogram plots were unique and all fail to be appropriate with a large residual magnitude. In the normal probability plot, the residual error terms curve away from the regression line especially near the ends. For the versus fits plot, the residuals did not appear random but take a U-shape trend indicating a higher order model was likely necessary. The histogram did not have a clean bell curve and was skewed to the right. This skewing was not believed to be large enough to benefit from a transformation. Versus order did not appear random due to how the data was acquired and put into Minitab 19 as well as how the regression was relatively less accurate near the ends. However, because this was the case for every regression as well as minimally increasing error at each force extreme in this test, the versus order plot was of low priority. The second order and third order regressions have higher R^2 values of 99.85% and 99.97% respectively. Contrasting the second order four-in-one residual plot trends to the first order, the versus fits residuals plot was distributed much better but still has some bending. Slight bending here still indicates a likely need for a higher order model. Looking at the histograms, the second order has a cleaner bell curve while being less skewed to the right becoming negligible. In the second order normal probability plot the lower extreme better hugs the fit line but was otherwise similar. The versus order plot again has peaking trends due to model inaccuracies at the

extremes. Second order model residual magnitudes appear much smaller particularly near the ends proving a more precise and accurate model than the first order residual model. Moving on to the third order four-in-one residual plot as contrasted to the second order, the normal probability plot residual error terms were more linear along the regression line in the third order plot. Reviewing the versus fits plots, the third order plot has a more ideal distribution. There was not much change in quality of the third order histogram plot by comparison. A trend was still present in the versus order plot but appears more suppressed in the third order model. Consequently, the third order regression was expected to outperform the second order regression when they were tested against each other with random input.

While the precision and accuracy of the second order and third order regressions were close, the third order adjusted regression consistently outperformed the second order regression. Evaluating the third order coefficient plots of both unadjusted and adjusted are shown in Figure 27. One term is highlighted red indicating failure to accept the null hypothesis with a P-value greater than 0.05. Consequently, the regression was performed again without this term to maximize the precision and accuracy of outcomes. As a result of this finding and four-in-one residual plot analysis, the adjusted third order regression was selected. When testing the finalized third order regression with randomly generated, continuous settings and comparing the outcome to rough interpolated values as well as what makes sense based on the collected data, the results appear accurate and acceptable.

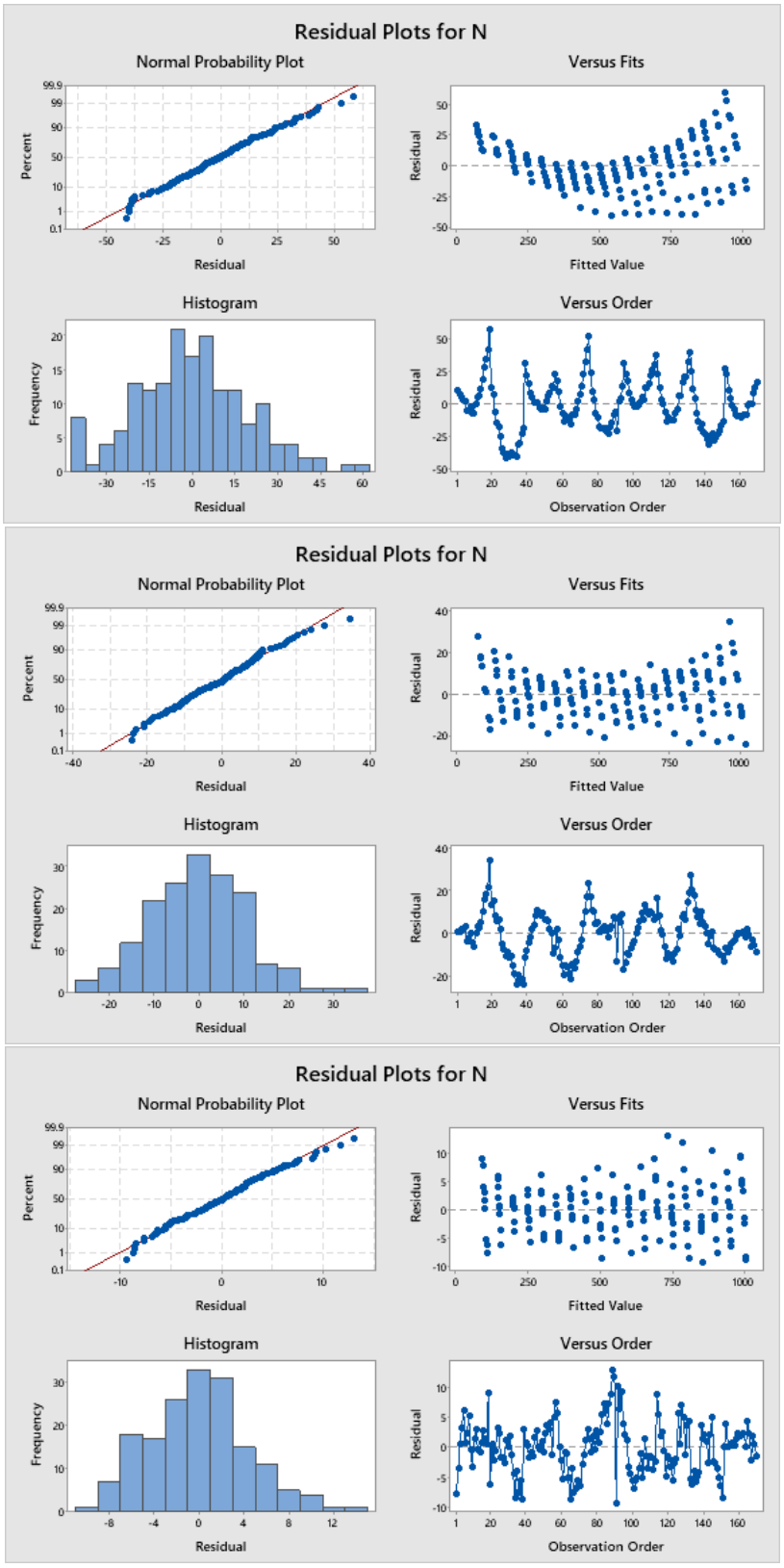

FIGURE 26 – Four-in-one residual plots of the first order (top), second order (middle), and third order (bottom) force (N) to microstrain (με) regressions from the quasi-static 2 true strain data.

3rd Order

Model Summary

S	R-sq	R-sq(adj)	R-sq(pred)
4.59745	99.97%	99.97%	99.97%

Coded Coefficients

Term	Coef	SE Coef	T-Value	P-Value	VIF
Constant	545.922	0.904	604.17	0	
A.F.	36.679	0.705	52.03	0	3.97
%	-121.359	0.754	-160.86	0	4.55
με	-315.22	1.1	-286.32	0	9.69
A.F.*A.F.	-4.475	0.503	-8.9	0	1.01
%*%	22.731	0.581	39.11	0	1.36
με*με	19.012	0.581	32.72	0	3.49
A.F.*%	-18.294	0.433	-42.23	0	1.49
A.F.*με	-20.357	0.44	-46.3	0	1.56
%*με	79.292	0.717	110.53	0	3.92
με*με*με	0.661	0.473	1.4	0.164	12.83
A.F.*A.F.*%	-1.439	0.542	-2.66	0.009	3.48
A.F.*A.F.*με	4.369	0.553	7.9	0	3.72
A.F.*%*%	-3.04	0.529	-5.75	0	3.32
A.F.*%*με	11.04	0.541	20.4	0	2.57
A.F.*με*με	1.219	0.442	2.76	0.007	3.72
%*%*με	-15.773	0.708	-22.26	0	6.56
%*με*με	-7.54	0.751	-10.04	0	12.16

3rd Order (Adjusted)

Model Summary

S	R-sq	R-sq(adj)	R-sq(pred)
4.61177	99.97%	99.97%	99.97%

Coded Coefficients

Term	Coef	SE Coef	T-Value	P-Value	VIF
Constant	545.914	0.906	602.3	0	
A.F.	36.633	0.706	51.86	0	3.97
%	-121.048	0.723	-167.38	0	4.16
με	-314.302	0.887	-354.26	0	6.25
A.F.*A.F.	-4.495	0.504	-8.92	0	1.01
%*%	22.878	0.574	39.89	0	1.31
με*με	19.13	0.577	33.18	0	3.42
A.F.*%	-18.362	0.432	-42.53	0	1.47
A.F.*με	-20.464	0.434	-47.12	0	1.51
%*με	79.776	0.63	126.63	0	3
A.F.*A.F.*%	-1.446	0.543	-2.66	0.009	3.48
A.F.*A.F.*με	4.399	0.554	7.93	0	3.72
A.F.*%*%	-3.035	0.531	-5.72	0	3.32
A.F.*%*με	11.142	0.538	20.72	0	2.53
A.F.*με*με	1.366	0.431	3.17	0.002	3.52
%*%*με	-15.988	0.694	-23.05	0	6.25
%*με*με	-8.269	0.541	-15.27	0	6.28

FIGURE 27 – Third order regression coefficient plots for unadjusted (left) and adjusted (right) regressions where a red highlight indicates a term with P-Value greater than 0.05.

Implementing such a regression equation, it was then possible to have a dynamic force output which was used to evaluate the success of a repetition according to the necessary force for bone stimulation. Furthermore, the software of the GUI was set to have an appropriate force threshold for data acquisition. From the force data, force over time could later be derived and converted to bone strain rate. All data were manipulated with peaks taken from raw data while graphs display filtered data with a moving window average of 7 similar to previous strain data. Filtered versus unfiltered data from an early volunteer iteration is displayed in Figure 28.

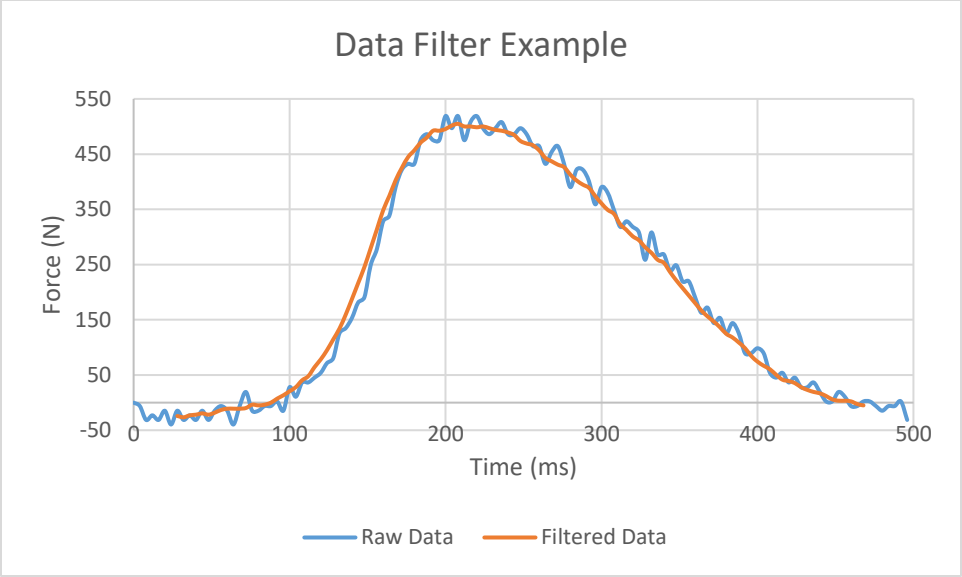

FIGURE 28 – Raw (blue) and filtered (orange) dynamic force data for one repetition.

The first test of independent setting influence was the pad arm setting or arm factor. It was noted that the trial of arm factor 0.75 had some reps that were performed with noticeably greater effort skewing the average data for that setting upward. As the pad arm setting was reduced becoming tighter on the hip, the loading events became larger, clearer, and more consistent. While the 0.75 setting was high, it still fits the general trend. Both average max force over arm factor data and example trial data is seen in Figure 29. Appendix XI shows the complete set of arm factor force data. Furthermore, the average force over arm factor plot reveals much greater force with narrower settings. To achieve this force, the settings became more difficult to achieve and even noted uncomfortable in the minimum fit setting. Consistently reaching the desirable force was still achievable at a more comfortable setting of 0.625 in this data while significantly higher force data was more easily achieved at narrower settings. It was also noted that one larger than the narrowest fitted setting without high difficulty commonly works best.

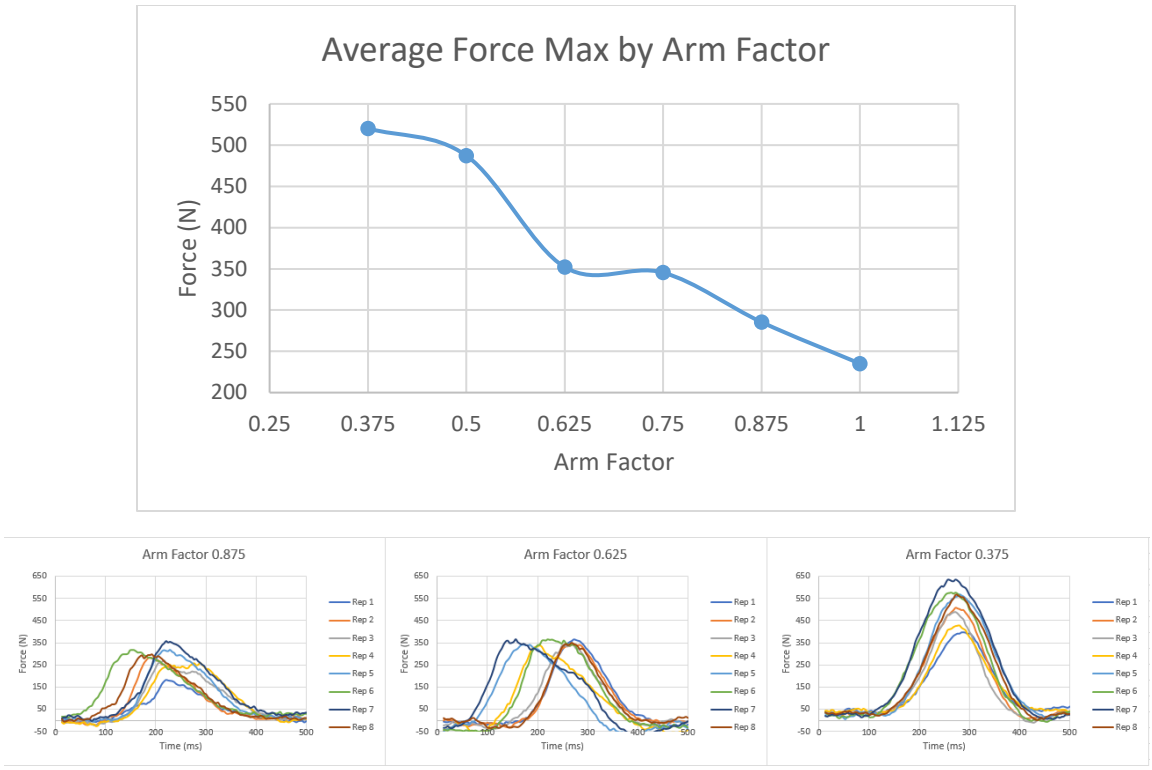

FIGURE 29 – Average force maxes by arm factor indicating quantitative influence of arm factor on force peaks (top) and example data displaying the qualitative influence of arm factor for trends (bottom).

Abductor drive was shown to have impacts on both force and jerk trends. Only hitting to the pad yields an average force output of 497 N, driving through the pad generating an average of 662 N, quickly hitting and resetting averaging 573 N, and an unparameterized normal rep average of 610 N. From this, relaxing upon hitting the pads shows consistently lower force by approximately 100 N when compared to other averages despite being an adequate average force. Driving through the pad typically resulted in a double peak where the max force was sometimes in the second peak. More differentiation occurred between jerk data. Figure 30 shows representative examples of force and jerk over time for each set. The total set of abduction instruction graphs is shown in Appendix XII. Reps of a quick hit and reset appear to generate a lot of excess jerk which makes finding a reliable peak difficult. Graphed data from instruction to hit

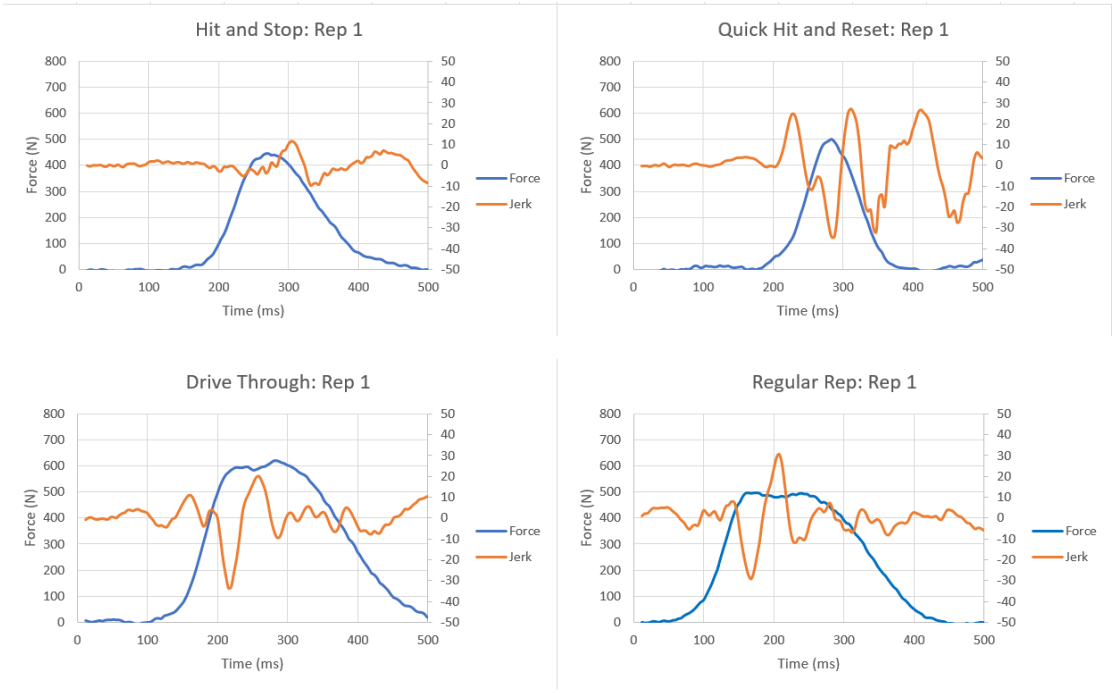

FIGURE 30 – Example repetition data of each abduction instruction displaying common characteristic differences in force magnitude, force trends, jerk magnitude, and jerk trends.

and relax did not have as smooth of curves as the data of regular instruction nor as the data of instruction to drive through the pads making the data less reliable. Repetition data from regular instruction and instruction to drive through the pad both consistently have clear, unique, and timely minimum jerk trends. All but one grip seems to have no effect on outcome. Only instruction to push down into the lap during the rep added late jerk minimums as seen in Figure 31. Rep 3 of squeeze instruction appears a large outlier. All grip graphs are found in Appendix XIII. Without this peak in jerk, the software would not accurately identify an event. There were also no consistent trends in force.

FIGURE 31 – An example force and jerk graph over time of a standard rep while pushing down onto the plate.

Despite not being an input factor that was able to be tested quasi-statically, knee arm setting seems to greatly affect force. Figure 32 shows a parabolic trend in force output throughout settings. This allowed for a range of viable user settings in which the knee arm could be set according to initial lap placement having the plate be at the belly while the knee plate was tangent to the adducted knees. It was noted that there was some discomfort when the setting was too low – 0.75” and below – and largely placed over the quadricep. This may have influenced lower effort into lower force reps. Another note expressed lesser effort for some reps at the 2.25” setting which would influence a softer curve at higher settings. Beyond 2.5”, there was an acute drop in average force output which was likely due to being placed over the acetabulum where no bending could be applied. Jerk appeared to act normally among each setting.

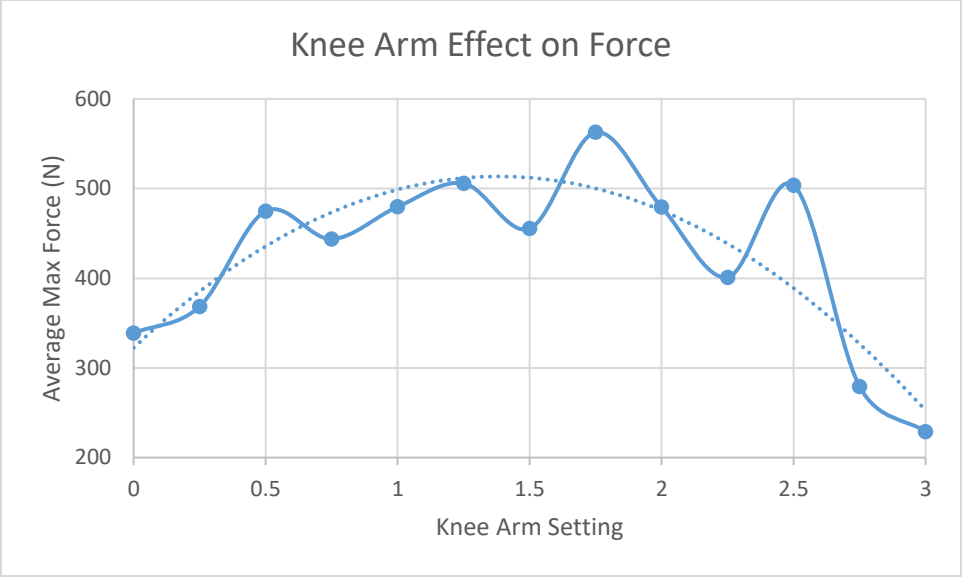

FIGURE 32 – A plot of average maximum forces at each knee arm setting.

Metronome data as seen in Table I below indicates an optimal range of beats per minute for the user to perform the exercise. With an increase in beats per minute, the standard deviation appears to increase. In addition to increasing standard deviation within trials, there appears to be drastic deviation in trial force average from the

TABLE I: Metronome Average Force and Standard Deviation Data

BPM:	40	60	80	100	120	140	Total
Average Force (N):	498.4	549.1	543.7	518.2	458.6	573.7	523.6
Standard Deviation (N):	47.2	44.2	52.5	62.9	86. 8	57.2	37.5

cumulative average in the 120 BPM and 140 BPM trials while the other trial averages remain within one standard deviation of total averages. Figure 33 shows two representative force and jerk over time plots of approximately how the jerk behaves in slower versus faster BPM trials of the metronome study. All metronome rep graphs can be found in Appendix XIV. Software issues in threshold recording of 40-80 BPM data resulted in duplicate reps which were not graphed while there was a complete set of reps

for the complete data from 100-140 BPM. It appeared that the jerk peaks were most notably positive as the force peaks in this sub-study contrary to most other jerk evaluation data. Despite this, there were also odd maximum and minimum peaks in jerk after the rep was performed. Jerk increases with BPM as expected while reps 2 and 6 of 140 BPM were extreme outliers. This sub-study was performed after volunteer trials.

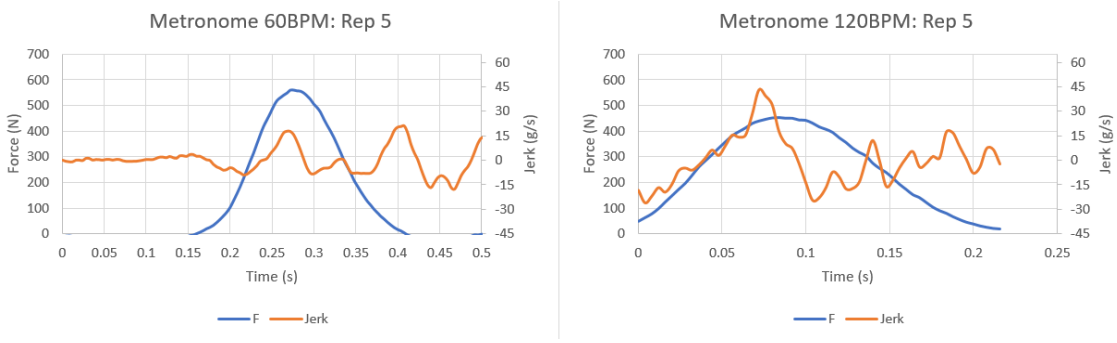

FIGURE 33 – Varying representative metronome force and jerk data of slower (left) and faster (right) BPM.

Reps from each pad setting were removed due to data repetition or as an outlier. There were four repeated reps in the single padded set while the double padded set had one repeat and one outlier. Otherwise given the same device settings, the double padded set of data had a consistently higher force output. Figure 34 shows that the single padded side consistently acquired an average force of 444 Newtons while the double padded side displays an average force of 598 Newtons. Both sets of data have small, respective standard deviations of 24.7 N and 40.3 N that ascertain a unique outcome by respective padding. It was also noted that the double padded side was more comfortable. This was also performed after volunteer trials.

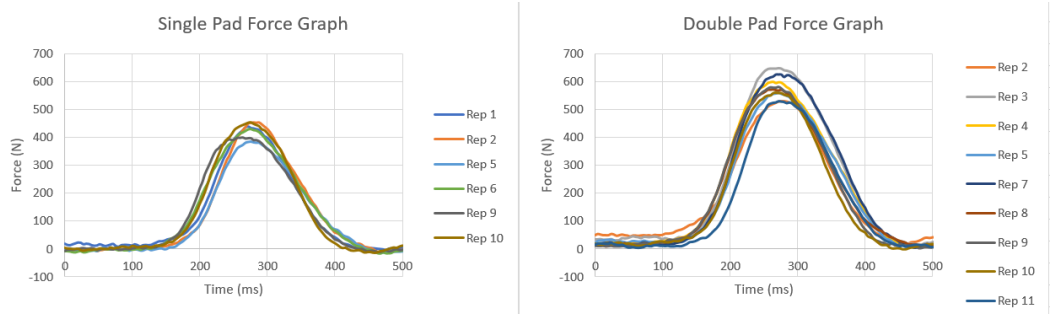

FIGURE 34 – Force graphs of unique single padded (left) and double padded (right) data.

Each user has unique anthropometry, settings, and data. Arm factor values ranged from 0.375 to 1.5, pad height values ranged from 2.25 to 4.25, and knee arm ranged from 0 to 2.5 as displayed in Table II. Some knee arm data was not collected in initial trials but was recorded in the most recent trials of any volunteer who performed more than once. Only arm factor and pad height were used for software inputs. Due to apparent software issues, only unique data was graphed and used for data analysis. Furthermore, due to time-based data truncation in some early volunteer trial data the threshold data acquisition window was increased to 290 ms both before and after an event force maximum. There were clear max force peaks in each case regardless of varying

TABLE II: Prototype Settings and Measurements by Volunteer

Volunteer Prototype Values			
Volunteer	Arm Factor	Pad Height	Knee Arm
1	0.625	3.7	2.5
2	1	2.75	1.5
3	1.5	2.86	---
4	0.75	3.35	---
5	0.875	3.56	---
6	0.375	2.78	---
7	0.625	4	2
8	1.25	4.25	1.75
9	1.125	2.75	0
10	0.375	2.25	0

magnitude with some having two peaks. These forces were achieved with varying force rates but still seem to correlate to their respective theoretical bone strain rates. Cumulative volunteer average maximum forces average to 499.5 N and an average standard deviation of 42.1 N. Some of these max forces come from a second, slightly larger peak as seen in Appendix XV to Appendix XXIV with the complete set of volunteer rep graphs through 0.5 seconds. Female volunteer average maximum forces were 486.3 N compared to 512.7 N in the male data with respective standard deviation averages of 36.9 N and 47.3 N. When plotted with jerk across all volunteers, it was commonly seen that there was a minimum peak near the top of the positive force slope to the maximum force peak. It was also common for this peak to be the most minimum peak. Example jerk and filtered force data from volunteers is seen below in Figure 35. For any case, the average jerk minimum was -13.8 g/s with a standard deviation of 3.2 g/s. Appendix XVII is one example set of data that shows that the minimum jerk was not always the minimum value at the band of interest where there was high force rate to the

FIGURE 35 – Example dynamic volunteer data showing a typical force curve with the minimum jerk peak as force increases.

force peak. Despite this, jerk values did not appear proportional to force nor strain rate values. Theoretical bone strain rate averages 21509.6 με/s with a standard deviation of 3032.9 με/s among all volunteers. There appears a software issue in recording the positive initial force rate of some reps that exceeded the width of time resulting in cut offs of force rate or false data up to 20 ms. Where there was still a positive initial force rate, only the data after 20 ms was used for peak force rate data thereby influencing the theoretical bone strain rate. Otherwise, only maximum force data was used while force rate and jerk data were not used. All of this can be seen in Appendix XV to Appendix XXIV. Female volunteer peak theoretical bone strain rate average 18459.0 με/s with a standard deviation of 2355.4 με/s while male volunteers average 24560.1 με/s with a standard deviation of 3710.4 με/s. When average force and average bone strain rate were collected from the users, all cases meet desired minimums for device use and rep performance. Table III displays the averages of unique user data. Any set of data was more consistent among their own reps than volunteer to volunteer performance.

TABLE III: Average Values of Volunteer Dynamic Data

Volunteer:	1	2	3	4	5	6	7	8	9	10	Average
Average Max Force (N):	418.5103	408.3181	817.9078	577.3127	351.8986	397.9717	545.8004	397.7099	457.6364	622.1613	**499.5227**
Standard Deviation (N):	45.22519	32.96395	85.668	54.90509	20.65233	30.11975	35.83346	26.22239	33.09027	56.35116	**42.10316**
Average Max Theoretical Bone Strain Rate (με/s):	23126.75	16183.3	44103.6	20958.33	16308.63	18303.42	18295.02	13701.12	18872.39	25243.32	**21509.59**
Standard Deviation (με/s):	4056.351	1352.526	4379.376	5952.081	2181.582	1982.518	2725.34	1630.351	1476.455	4592.42	**3032.9**
Average Jerk Minimum (g/s):	-12.5023	-11.033	-36.2285	-12.9625	-12.2163	-22.8298	-3.60967	-11.9485	-9.47661	-5.43176	**-13.8239**
Standard Deviation (g/s):	4.107513	3.305828	3.824303	3.705262	4.352698	5.112065	0.666077	2.733435	2.252704	1.740386	**3.180027**

IV. DISCUSSION

A. Significance

In its final iteration, the prototype is a mobile and functional device capable of fulfilling its tasks: acquiring accurate, dynamic data for next-stage testing. Functionality and versatility were major parameters to overcome in order to ensure the target population could test with reliable results. Hopefully, the users will benefit from the exercise to be tested later. Despite slight differences in outcomes likely caused by parameter and modeling variation, calculations alongside FEAs have proven integrity under extreme loading at extreme locations which are unlikely to be seen in use via outcomes below the respective material maximum yield strengths. Similarly, longevity based upon previous expected user input was ensured with results below the respective endurance limit of each material. The maximum result values of the plate and pin FEA analysis are revealed at specific geometry indicating where a failure would be expected should failure occur. While these results were promising, the expected performance of the prototype is expected to be greater due to limitations in calculations and modeling. Consequently, its design is projected to be safe as well as to be durable over time in testing.

A sufficient location for the strain gage was selected based on the early iteration FEA strain profile. The mounted sensor is proven both functional and sensitive in both raw voltage and strain outputs in early quasi-static testing. From here, preliminary data

was collected to ascertain software sufficiency and assess qualitative trends in force and acceleration. During this, many software issues were discovered and rectified while qualitative data trends were also noted. Among these trends, it was noticed that the largest slope of acceleration appears to consistently occur near the max force curve becoming a major unexpected deliverable to be used in further testing. Having functional hardware and reliable software output in terms of microstrain, the device could be tested quasi-statically again over a force range greater than what was expected by the user. This data was used to provide an adaptable regression equation across continuous prototype settings for an interpolated strain gage to pad force output. Due to the statistical software four-in-one plots and model summaries among various order regressions, the third order regression was proven optimized for accuracy. Utilizing this equation, the force applied to the pad and on the user during hip abduction could be generated according to the strain gage output at any device setting and user morphology. This is unique to this study as the previous device iteration study analyzed discrete force data.

At this point, output values were crucial to proving a series of effective device use and volunteer data. An important clarification was made to ensure the recording of raw peak values while filtering was added for the purposes of both qualitative trend analysis and quantitative force derivative analysis. Many setting and performance analyses were then evaluated to maximize effectiveness and future software readability. Arm factor as the pad arm setting is almost linearly proportional to average max force output where a narrower arm factor generates a larger force outcome. It was deduced that the increase in force output is due to an increased relative torque about the acetabulum in the three-point bending model as the location of the pin nears the axis under the same muscular torque.

This factor could be manipulated to benefit each user according to output and comfort requirements. Abductor drive revealed that the best rep for large forces and reliable jerk data appear with minimum instruction and driving through the pad. For the purposes of identifying force peaks by jerk data, these appear the ideal instruction. Coincidentally, these instructions were the simplest and most intuitive for the user. Similarly, the set of grip tests favor more natural grips so long as the user was not pushing down on the plate which negatively impacts jerk data. The force over knee arm graph follows a parabolic trend that provides a range of force output exceeding the required force threshold for bone stimulation. Acting similar to the pad arm factor, if the knee arm setting was too narrow especially where the proximal plate curvature leaves the belly, the pin location in the three-point bending model damps output while also generating discomfort over the quadricep. At too long of a setting in combination with a static pad arm setting which pull the proximal plate geometry into the belly, the pin could be over or behind the acetabulum eliminating the ability to generate force nor three-point bending. A balance of knee arm and pad arm settings were required. Beginning with an appropriate knee arm setting, subsequent pad arm adjustment was found to generate successful outcomes. Metronome clearly influences the repeatability of force output according to standard deviations while magnitude seems less affected. Likewise, jerk was favored for its qualitative performance in lower BPM trials. Consistency, ease of performance, and the ability for the software to read the jerk trends were prioritized. While it seems none of the metronomes were ideal, 60 BPM seems to have the best data fulfilling most of the priorities while also still achieving bone strain rate thresholds required for trabecular osteogenesis. The user's relative inability to perform at higher BPM is attributed to the

less favorable results as a whole despite the expectation that faster metronomes would facilitate significantly greater and more favorable data. Double padded appears to enhance force output as well as comfortability. This aligns with the increased force output of narrower arm settings due to an increase of material between the pin and the femur. An accumulation of best modes of fitting the prototype and user practices in performing the exercise was formulated from the collective results of these brief sub-studies to benefit the outcome for the user and the reliability of that outcome for future software relevance.

Beyond design and performance verification, dynamic volunteer data provided relevant deliverables also used in Troy et al., 2020 that can be compared to previous data on bone stimulation. Strain and strain rate thresholds are suggested to indicate anabolic bone remodeling in the literature which were then used as metrics for our testing as per Duncan et al., 2002, Judex et al., 2000, Osbourne, 2017, Rubin & Lanyon, 1985, Troy et al., 2020, and Turner & Takano, 1995. The average max force reading of 499.5 N exceeding the suggested force minimum of 350 N as well as exceeding the tested previous force magnitude target of 450 N which generated successful bone strain magnitudes in Osbourne, 2017. An average force above this implies even greater bone microstrain magnitudes of the bone ensuring remodeling. Perhaps more valuable is the theoretical bone strain rate total average of 21509.6 με/s and smallest volunteer average of 13701.1 με/s both of which are well above the 10000 με/s threshold for osteogenic stimulation. The femoral neck of the proximal femur is suspected to be stimulated by appropriately utilizing the fitted device in agreement with the literature according to known biomechanical modes and appropriate exercise stimulation as per Hall, 2016

Manske et al., 2009, Lee et al., 2017, Narra et al., 2013, Osbourne, 2017, and Stengel et al., 2005. Meeting these target metrics with a lateral vector translates to potentially stimulating lateral anabolic bone remodeling in the hip which could lead to reducing hip fracture rates of the aging population. Furthermore, device use exercise may lead to aid in hip abductor muscle readiness through regimented exercise performance. Jerk values do not appear to be proportional to user bone formation metric outcomes and thus does not seem to be a viable alternative to evaluate user repetition performance adequacy.

B. Limitations

Anthropometry data used in the design phase of this work was geared toward an archetype most vulnerable to lateral fall hip fracture. It is unlikely that the prototype will fit any individual given the limits of adjustability. Due to additional individual morphology, it is also possible that some potential users within the target archetype may not find a workable setting. Pad arm settings are the most likely issue with individual fitting caused by the influence of varying femur lengths and hip widths. In these instances, no combination of settings could be found for the user to generate appropriate hip loading thus insufficient bone strain and bone strain rate. There is also a possibility for human error in appropriately fitting a user or measuring setting values as inputs for the processing software. Errors such as these could generate inaccurate output values.

FEAs used in strength analyses of the device. In any case of running a static simulation, a mesh of the parts is required. Due to the complex geometry of parts such as the top plate or the head of the pin, a fine mesh was not always able to be rendered even with a simplified pin. Meshing quality can alter local outcomes of magnitude particularly in rounded edges where maximum strain values were found. In the case of these analyses,

that should translate to overestimating maximum values when evaluating safety. There may also be slight differences in the FEA models and actual parts due to fabrication part tolerance. This could mean some parts interacting differently on the prototype versus the FEA model. Calculations for strength analyses were also limited by part simplification and assumptions. These limitations do not factor for complex geometry nor part bending with loading as seen in the FEA. The system used in calculations assume complete rigidity while providing homogenous outcomes regardless of how stress may disperse according to the geometry. These are most present in the pin calculations where the fillet geometry, height, and shoulder spacing from the arm were not accounted for due to incorrect assumptions about the part prior to ordering.

Software was responsible for collecting, processing, and reporting data. Over the course of this study, the software constantly developed new formatting but reported the same, accurate data based on the regression in any case. It was noted that the 100 setting of quasi-static data was mounted slightly higher on the pad for safety set up resulting in potential inaccuracy at larger pad height settings. Additionally, due to plate bending, the pad was likely loaded at the top edge of the MTS mounting bars versus the middle by which it was aligned. However, there were instances in which the data of interest was not reported due to how the threshold collection mode operates. Collecting data in a limited window caused some critical time-based data to be truncated or generate a large false force rate up to 20 ms especially when the user performed a long rep. Without the large positive force slope data, only the usable results were analyzed for averages but provides a smaller sample size. Some data even in the latest software iteration would reveal a unique instance but copy the data of the previous event. Volunteer data collection was not

performed to a metronome potentially generating a recording issue in which event peaks were too close according to the programing if the user performed reps too rapidly. Ultimately this also leaves a smaller sample of usable data. Furthermore, the metronome sub-study data above 104.5 BPM was manually filtered and processed from complete data as this was the software upper limit before there are issues in output. Conversion from bone force to bone strain was extrapolated exclusively from 450 N data which is only assumed to be linearly proportional across all forces.

As previously stated, volunteer testing was performed over time while some tweaks were still being made. While it is not believed that this had a direct impact on recording data, it is possible that there were small changes around the data collection that could influence the values recorded such as refining pad height measurement as an input. No volunteer was of the target archetype nor were the volunteer trials of a large sample size. Consequently, the data provided is not generalizable to a larger population but instead proves the functionality of this iteration of device hardware and software alongside the ability of a user to generate adequate pad and hip loads with the exercise. Sub-studies data was performed by one volunteer limiting their generalizability despite repetition volume at each respective setting and study.

C. Future Development

Future prototype development would be beneficial in use. Utilizing a lighter but rigid material would allow the device to be easily transported and manipulated for the user. Current lightening geometry could also be adjusted. A wider radius of the proximal, medial corner of the large proximal cutouts could reduce stress focus bringing lower risk of plate strength issues. Furthermore, adding curved ribs in line with leg abduction

pathway in the large cutouts would prevent the potential issue with hanging up on clothes or the leg during exercise while remaining light. Adding more discrete measurement settings could aid in user fitting of the device with further tailored user software input.

This software iteration performs well but with functional flaws. Updates need to be made in order to ensure consistent and unique outputs. Having evaluated trends, the relevant trends appear in the positive slope and peak regions of the force curve. Focusing the recordings on this area of an event could reduce the incidents of losing the positive slope and maintain unique event recording in the case that a user performs repetitions at a frequency above 104.5 BPM. Additionally, this would likely resolve the false rate issue caused by truncated force slopes. Changing the center-difference derivative to backwards-difference derivative in data processing was also favored for less damped maximum rate of already smoothed data. While that development was crucial to appropriate acquisition, other features may benefit the efficiency of data collection and processing such as image or graph generation, eliminating the threshold startup event recording, a table summary of valued inputs, and user setting input memory.

Testing has many next steps. Utilizing one static method of both device use and user setting acquisition based on the refinements made in this study would maximize the comparability of volunteer data. More testing data would be useful in diagnosing quantitative jerk trends in relation to force for a future iteration. A future iteration would ideally be of a lighter material for user ease and minimizing production cost. A larger study of more individuals performing multiple sets over time would ensure greater generalizability and stronger data validation. Most importantly, a formal study of the target archetype is a future step with both pre- and post- DEXA scan evaluation would

acquire more specific data that could prove device efficacy on anabolic bone remodeling in vivo. Evaluating hip strength and reactivity may also prove muscular utility of the device to users as this has not been done but may influence a user's risk of hip fracture due to falling.

V. CONCLUSION

A next-generation prototype device has been designed and fabricated to fit a variety of anatomical user profiles while also meeting device integrity objectives. Statistical regression model values based on strain gage output through continuous, varying user settings processed via custom software provides an accurate conversion from plate microstrain to user pad force which is used to find theoretical bone strain rate. From here, the design was further proven capable of achieving the lateral forces at the hips as the user performs the exercise in volunteer testing. Optimum user factors were identified for a best outcome. Volunteer force data implies that the biological requirements of strain and strain rate for inducing anabolic bone remodeling are met in accordance with the first iteration study thus validating the prototype. GUI feedback from the designed software indicates a user-met force threshold. Collectively, the results from the volunteer trials suggest that this device could potentially aid in reducing hip fracture by enhancing the lateral framework of bone at the hip but do not support jerk values as an alternative evaluation of repetition adequacy. Clinical trials of a larger and longer standardized study will be necessary to prove device efficacy on bone remodeling in the target population.

VI. REFERENCES

Bayraktar, H. H., Morgan, E. F., Niebur, G. L., Morris, G. E., Wong, E. K., & Keaveny, T. M. 2004. Comparison of the elastic and yield properties of human femoral trabecular and cortical bone tissue. *Journal of Biomechanics, 37*(1), 27-35.

Burge, R., Dawson-Hughes, B., Solomon, D. H., Wong, J. B., King, A., and Tosteson, A. 2007. Incidence and economic burden of osteoporosis-related fractures in the united states, 2005-2025. *Journal of Bone and Mineral Research, 22*(3), 465-475.

Caetano-Lopes, J., Canhão H, and Fonseca, J. E. 2007. Osteoblasts and bone formation. *Acta Reumatologica Portuguesa, 32*(2), 103-110.

de Bakker, P. M., Manske, S. L., Ebacher, V., Oxland, T. R., Cripton, P. A., and Guy, P. 2009. During sideways falls proximal femur fractures initiate in the superolateral cortex: evidence from high-speed video of simulated fractures. *Journal of Biomechanics, 42*(12), 1917-1925.

Dick, I. M., and Prince, R. L. 1997. Estrogen effects on the renal handling of calcium in the ovariectomized perfused rat. *Kidney International, 51*(6), 1719-28.

Duncan, C. S., Blimkie, C. J., Cowell, C. T., Burke, S. T., Briody, J. N., and Howman-Giles, R. 2002. Bone mineral density in adolescent female athletes: relationship to exercise type and muscle strength. *Medicine and Science in Sports and Exercise, 34*(2), 286-294.

Farahmand, B. Y., Michaëlsson Karl, Ahlbom, A., Ljunghall, S., and Baron, J. A. 2005. Survival after hip fracture. *Osteoporosis International: With Other Metabolic Bone Diseases, 16*(12), 1583-1590.

Fryar C.D., Gu Q., and Ogden C.L. 2012. Anthropometric Reference Data for Children and Adults: United States, 2007-2010. National Center for Health Statistics. *Vital Health Statistics, 11*(252).

Glinkowski, W., Narloch, J., Krasuski, K., & Śliwczyński Andrzej. 2019. The increase of osteoporotic hip fractures and associated one-year mortality in poland: 2008–2015. *Journal of Clinical Medicine, 8*(9), 1487.

Hall, J. E. 2016. *Guyton and Hall Textbook of Medical Physiology* (13th edition.). Philadelphia, PA: Elsevier.

Hayes, W.C., Myers, E.R., Morris, J.N., Gerhart, T.N., Yett, H.S., and Lipsitz, L.A. 1993. Impact near the hip dominates fracture risk in elderly nursing home residents who fall. *Calcified Tissue International*, *52*,192-198.

Horii, M., Fujiwara, H., Mikami, Y., Ikeda, T., Ueshima, K., Ikoma, K., and Kubo, T. 2016. Differences in monthly variation, cause, and place of injury between femoral neck and trochanteric fractures: 6-year survey (2008-2013) in kyoto prefecture, japan. *Clinical Cases in Mineral and Bone Metabolism: The Official Journal of the Italian Society of Osteoporosis, Mineral Metabolism, and Skeletal Diseases*, *13*(1), 19-24.

Judex, S. and Zernicke, R. F. 2000. High-impact exercise and growing bone: relation between high strain rates and enhanced bone formation. *Journal of Applied Physiology (Bethesda, Md.: 1985)*, *88*(6), 2183-2191.

Koh, G. C., Tai, B. C., Ang, L. W., Heng, D., Yuan, J. M., and Koh, W. P. 2013. All-cause and cause-specific mortality after hip fracture among chinese women and men. *Osteoporosis International: A Journal Established As Result of Cooperation between the European Foundation for Osteoporosis and the National Osteoporosis Foundation of the Usa*, *24*(7), 1981-1989.

Lee, S. H., and Kim, H. S. 2017. Exercise interventions for preventing falls among older people in care facilities: a meta-analysis. *Worldviews on Evidence-Based Nursing*, *14*(1), 74-80.

Li, J., Bao, Q., Chen, S., Liu, H., Feng, J., Qin, H., Li, A., Liu, D., Shen, Y., Zhao, Y., Zong, Z. 2017. Different bone remodeling levels of trabecular and cortical bone in response to changes in wnt/β-catenin signaling in mice. *Journal of Orthopaedic Research*, *35*(4), 812-819.

Määttä Mikko, Moilanen, P., Timonen, J., Pulkkinen, P., Korpelainen, R., & Jämsä Timo. 2014. Association between low-frequency ultrasound and hip fractures -- comparison with dxa-based bmd. *Bmc Musculoskeletal Disorders*, *15*(1), 208.

Manske, S., Lorincz, C., and Zernicke, R. 2009. Bone health: part 2, physical activity. *Sports Health*, *1*(4), 341-346.

MatWeb, LLC, "Aluminum 6061-T6; 6061-T651," *Internet Source*, available from http://www.matweb.com/search/DataSheet.aspx?MatGUID=b8d536e0b9b54bd7b69e4124d8f1d20a; last accessed 8 August 2020.

Narra, N., Nikander, R., Viik, J., Hyttinen, J., and Sievänen Harri. 2013. Femoral neck cross-sectional geometry and exercise loading. *Clinical Physiology and Functional Imaging*, *33*(4), 258-266.

Niebur, G. L., Feldstein, M. J., Yuen, J. C., Chen, T. J., and Keaveny, T. M. 2000. High-resolution finite element models with tissue strength asymmetry accurately predict failure of trabecular bone. *Journal of Biomechanics, 33*(12), 1575-1583.

Openshaw, S. and Taylor, E. 2007. *Ergonomics and Design: A Reference Guide*. Diane Publishing, p. 13.

Osbourne, A. 2017. Biomechanical testing of an exercise for strengthening the proximal femur. *Electronic Theses and Dissertations.* Paper 2813. Master of Engineering thesis, University of Louisville.

Pistoia, W., van Rietbergen, B., Lochmüller E.-M, Lill, C. A., Eckstein, F., and Rüegsegger P. 2002. Estimation of distal radius failure load with micro-finite element analysis models based on three-dimensional peripheral quantitative computed tomography images. *Bone*, *30*(6), 842-848.

Prince, R. L., Schiff, I., and Neer, R. M. 1990. Effects of transdermal estrogen replacement on parathyroid hormone secretion. *The Journal of Clinical Endocrinology and Metabolism, 71*(5), 1284-1287.

Rubin, C.T. and Lanyon, L.E. 1985. Regulation of bone mass by mechanical strain magnitude. *Calcified Tissue International, 37*, 411-417.

Stengel, S. V., Kemmler, W., Pintag, R., Beeskow, C., Weineck, J., Lauber, D., Engelke, K. 2005. Power training is more effective than strength training for maintaining bone mineral density in postmenopausal women. *Journal of Applied Physiology (Bethesda, Md: 1985)*, *99*(1), 181-188.

Stevens, J. A. and Rudd, R. A. 2013. The impact of decreasing u.s. hip fracture rates on future hip fracture estimates. *Osteoporosis International: A Journal Established As Result of Cooperation between the European Foundation for Osteoporosis and the National Osteoporosis Foundation of the Usa*, *24*(10), 2725-2728.

Troy, K.T., Mancuso, M.E., Johnson, J.E., Wu, Z., Schnitzer, T.J., Butler, T.A. 2020. Bone adaptation in adult women is related to loading dose: a 12-month randomized controlled trial. *Journal of Bone and Mineral Research, 35*(7), 1300-1312.

Turner, C. H., Owan, I., and Takano, Y. 1995. Mechanotransduction in bone: role of strain rate. *American Journal of Physiology-Endocrinology and Metabolism*, *269*(3), 442.

von Friesendorff, M., McGuigan, F. E., Wizert, A., Rogmark, C., Holmberg, A. H., Woolf, A. D., and Akesson, K. 2016. Hip fracture, mortality risk, and cause of death over two decades. *Osteoporosis International: A Journal Established As*

Result of Cooperation between the European Foundation for Osteoporosis and the National Osteoporosis Foundation of the Usa, *27*(10), 2945-2953.

Ziller, M., Herwig, J., Ziller, V., Kauka, A., Kostev, K., and Hadji, P. 2012. Effects of a low-dose oral estrogen only treatment on bone mineral density and quantitative ultrasonometry in postmenopausal women. *Gynecological Endocrinology: The Official Journal of the International Society of Gynecological Endocrinology*, *28*(12), 1002-1005.

APPENDIX I.

UPPER LEG LENGTH (Fryar et al., 2012)

Table 34. Upper leg length in centimeters for females aged 20 and over and number of examined persons, mean, standard error of the mean, and selected percentiles, by race and ethnicity and age: United States, 2007–2010

Race and ethnicity and age	Number of examined persons	Mean	Standard error of the mean	Percentile								
				5th	10th	15th	25th	50th	75th	85th	90th	95th
				Centimeters								
All racial and ethnic groups[1]												
20 years and over	5,676	36.7	0.10	31.2	32.5	33.4	34.7	36.9	38.9	40.0	40.7	41.8
20–29 years	943	38.1	0.13	33.3	34.7	35.3	36.2	38.2	39.9	40.8	41.5	42.5
30–39 years	986	37.6	0.13	32.6	33.9	34.7	35.6	37.5	39.5	40.8	41.6	42.5
40–49 years	1,032	37.0	0.12	32.0	33.1	33.9	35.2	37.0	38.9	40.0	40.7	41.9
50–59 years	834	36.2	0.17	30.1	32.0	32.8	34.2	36.5	38.4	39.5	40.1	41.0
60–69 years	906	35.7	0.13	30.3	31.6	32.3	33.6	36.0	37.9	38.8	39.6	40.5
70–79 years	627	35.0	0.20	29.1	30.9	31.7	32.9	35.0	37.3	38.3	39.0	39.9
80 years and over	348	34.2	0.25	29.0	30.3	30.9	32.3	34.2	36.0	37.1	38.1	39.9
Non-Hispanic white												
20 years and over	2,635	36.8	0.11	31.5	32.8	33.7	35.0	37.0	38.9	39.9	40.6	41.6
20–39 years	796	38.1	0.12	33.9	35.0	35.4	36.3	38.1	39.9	40.8	41.5	42.2
40–59 years	832	36.8	0.13	31.6	33.0	33.9	35.2	37.0	38.7	39.8	40.5	41.4
60 years and over	1,007	35.4	0.16	30.1	31.4	32.2	33.4	35.3	37.4	38.4	39.1	40.2
Non-Hispanic black												
20 years and over	1,075	38.4	0.21	32.4	33.8	34.9	36.3	38.5	40.6	41.9	42.5	43.4
20–39 years	373	39.7	0.24	34.1	36.0	37.0	37.9	39.7	41.8	42.5	43.2	44.6
40–59 years	364	38.0	0.23	32.4	33.7	34.8	36.0	38.2	40.1	41.1	41.9	42.8
60 years and over	338	36.3	0.24	30.3	31.7	32.8	34.0	36.5	38.7	39.9	40.6	41.6
Hispanic[2]												
20 years and over	1,692	35.1	0.12	29.5	30.9	31.9	33.0	35.1	37.2	38.3	39.1	40.0
20–39 years	650	36.0	0.18	30.9	32.3	33.0	34.0	36.0	38.1	39.1	39.7	40.7
40–59 years	567	34.7	0.19	29.2	30.7	31.5	32.8	34.9	36.6	37.6	38.4	39.4
60 years and over	475	32.8	0.26	27.3	28.7	29.4	30.6	33.0	35.0	36.1	36.9	37.7
Mexican American												
20 years and over	1,037	34.8	0.12	29.1	30.6	31.5	32.8	34.9	36.9	38.1	38.8	39.7
20–39 years	412	35.7	0.22	30.5	32.0	32.8	33.7	35.6	37.9	38.7	39.3	40.5
40–59 years	343	34.4	0.21	28.7	30.6	31.4	32.5	34.4	36.3	37.3	38.1	39.5
60 years and over	282	32.3	0.21	25.8	28.4	29.1	30.2	32.6	34.5	35.5	36.1	37.6

[1]Persons of other races and ethnicities are included.
[2]Mexican-American persons are included in the Hispanic group.

SOURCE: CDC/NCHS, National Health and Nutrition Examination Survey.

APPENDIX II.

SEATED ANTHROPOMETRY (Openshaw et al., 2007)

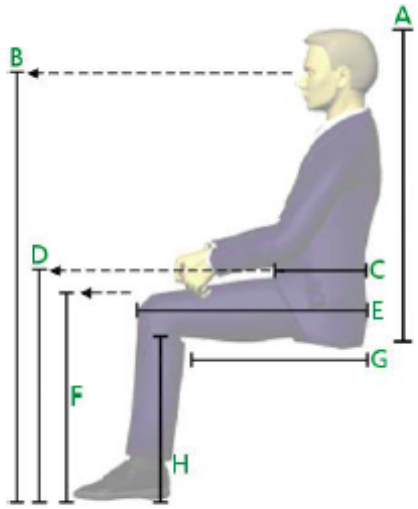

Figure 4. Common anthropometric measurements for the seated position. Use Table 2 for values.

Measurement	Letter	Female 5th – 95th%	Male 5th – 95th%	Overall Range 5th – 95th%
Sitting Height	A	31.3" – 35.8"	33.6" – 38.3"	31.3" – 38.3"
Sitting Eye Height	B	42.6" – 48.8"	46.3" – 52.6"	42.6" – 52.6"
Waist Depth	C	7.3" – 10.7"	7.8" – 11.4"	7.3" – 11.4"
Thigh Clearance	D	21.0" – 24.5"	23.0" – 26.8"	21.0" – 26.8"
Buttock-to-Knee	E	21.3" – 25.2"	22.4" – 26.3"	21.3 – 26.3"
Knee Height	F	19.8" – 23.2"	21.4" – 25.0"	19.8" – 28.0"
Seat Length/Depth	G	16.9" – 20.4"	17.7" – 21.1"	16.9" – 21.1"
Popliteal Height	H	15.0" – 18.1"	16.7" – 19.9"	15.0" – 19.9"
Seat Width	Not Shown	14.5" – 18.0"	13.9" – 17.2"	13.9" – 18.0"

Table 2. Values for 5th to 95th percentile males and females in the seated position used in designing seating. Use Figure 4 for visualization. Data from BIFMA Ergonomics Guidelines, 2002. All measurements are in inches.

APPENDIX III

STRAIN GAGE MOUNTING

Protocol:

1. Degrease area on the surface of the top plate around gage placement with CSM-1.
2. Apply acidic Conditioner-A to degreased section.
3. In small, circular motion, use sandpaper to perform a wet clean leaving fine scuffing to the surface.
4. Wipe with fuzz-free paper towel or cloth in a single direction using fresh area with each stroke.
5. Clean with 70% isopropyl alcohol and repeat Step 4.
6. Reapply Conditioner-A and repeat Step 4.
7. Apply basic M-Prep Neutralizer and repeat Step 4.
8. Repeat Steps 2-7 as needed.
9. Using a pencil and scale, carefully mark the surface for gage alignment.
10. Using forceps, carefully place the gage according to Step 9 along with additional soldering tabs to protect the gage leads from wire pull.
11. Pre-fold a tab on a strip of cellophane tape and cover the strain gage. Slowly fold back removing the gage leaving some tape on the surface.
12. Apply a small amount of E-6000 glue to the back of the gage and tabs proximal to the plate.
13. Return the gage to its placement on the plate via sliding a finger from the tape on the plate to the tab ensuring a complete, thin, and even coat of adhesive. Hold for 5 minutes.
14. Remove tape by pulling the tab at a steep angle to leave the gage in place.
15. Repeat Steps 1-15 as necessary.
16. Remove excess glue and solder the necessary wires.

APPENDIX IV.

DEVICE PLACEMENT IN THE MTS MACHINE

Protocol:

1. Turn on MTS machine and prepare device settings.
2. With bar attachments, increase distance to just beneath pad setting width.
3. Place top bar on pad according to the percent pad height:
    a. For 50%, ensure the center of the bar is in center of pad height.
    b. For 75%, ensure the center of the bar is exactly between the middle and bottom of the pads.
    c. For 100%, line up bottom of bar with bottom of pad to prevent slipping off with bending.
4. Keeping the bar perpendicular to the pads, the plate perpendicular to the ground, and keeping the pads at the bottom of the pins, slowly introduce MTS height just enough for the device to be secure and free standing.
5. Zero the MTS force readings.
6. Turn on gage recording software (should zero automatically).
7. Begin loading for experiment recording change in force.

APPENDIX V.

TOP PLATE CALCULATIONS

*Second Plate Calculation Example Math

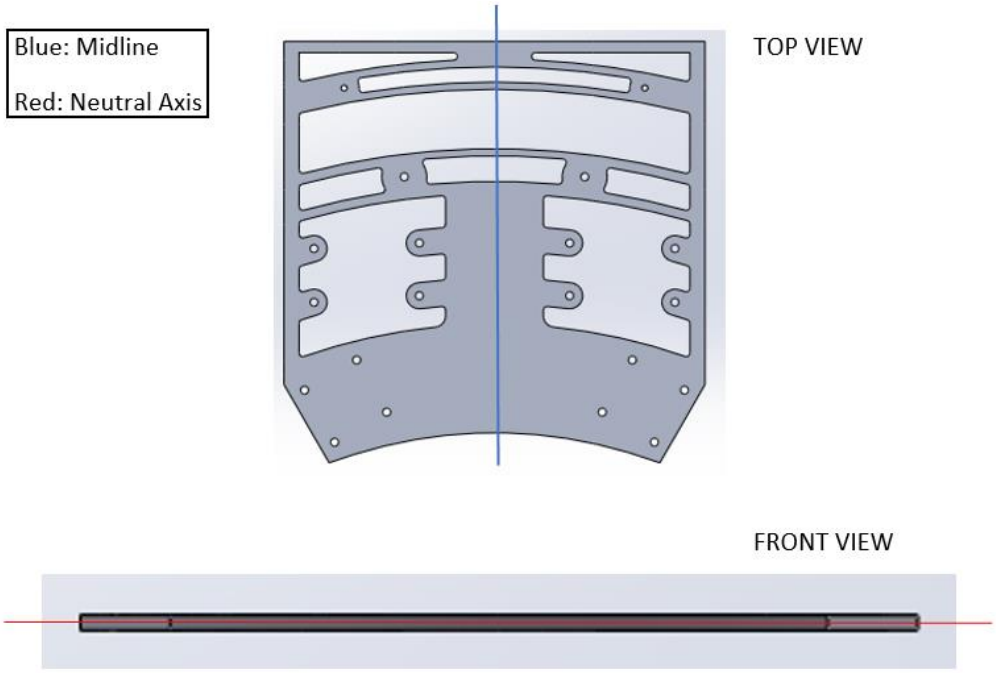

Bending Stress on plate:

σ_B = Bending Stress

M = Moment Arm

F = Force

$d_{perpendicular}$ = Perpendicular Distance (Pin Shoulder Length)

y = Distance from Neutral Axis

$I_{A,\ rect.}$ = Area of Inertia for a Rectangle

b = Base Length

h = Height Length

$$\sigma_B = \frac{My}{I_A} \left(\frac{N}{mm^2} \; or \; MPa\right)$$

$$M = F \times d_{perpendicular}$$

$$I_{A,rect.} = \frac{1}{12} bh^3 \; (mm^4)$$

Where:

$$1in = 25.4 \; mm$$

ABOUT AREA OF CONCERN:

$$d_{perpendicular} = 5.5in$$

$$d_{perpendicular} = 5.5in \left(\frac{25.4mm}{1in}\right)$$

$$d_{perpendicular} = 139.7mm$$

$$y = \frac{0.25in}{2}$$

$$y = 0.125in$$

$$y = 0.125in \left(\frac{25.4mm}{1in}\right)$$

$$y = 3.175mm$$

$$F = 1000N$$

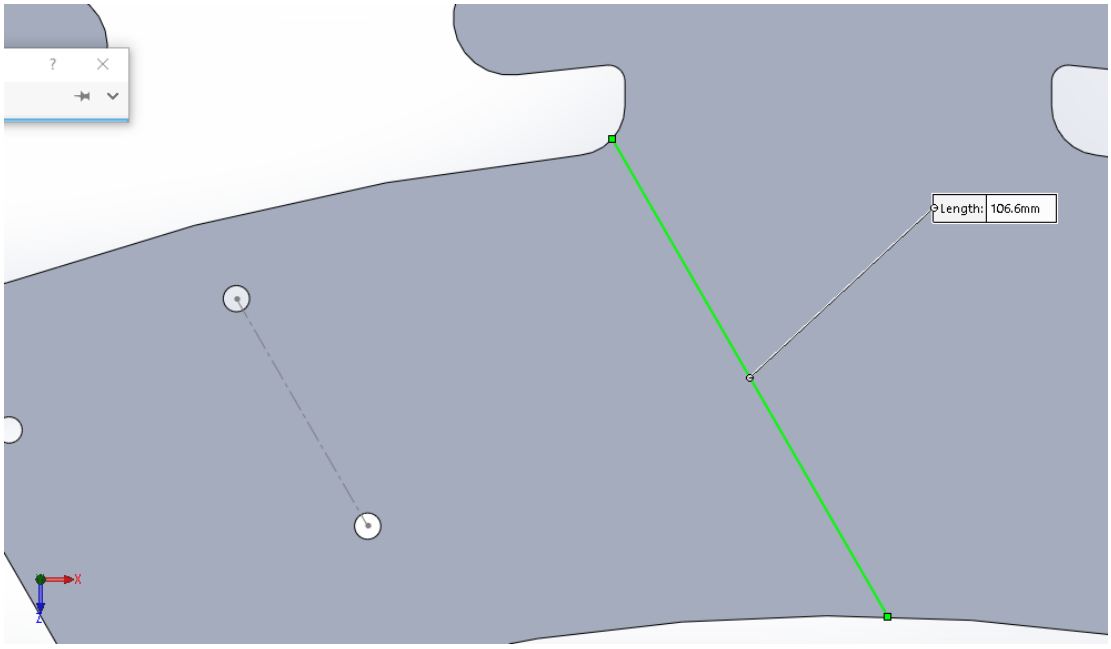

$$b = 106.6\,mm$$

$$h = 0.25in$$

$$h = 0.25in\left(\frac{25.4mm}{1in}\right)$$

$$h = 6.35\,mm$$

For M:

$$M = F \times d_{perpendicular}$$

$$M = 1000N(cos30) \times 139.7mm$$

$$M = 866.0N \times 139.7mm$$

$$M = 120{,}980.2\,N \times mm$$

For I_A:

$$I_{A,rect.} = \frac{1}{12}bh^3\ \ (mm^4)$$

$$I_{A,rect.} = \frac{1}{12}(106.6mm)(6.35mm)^3$$

$$I_{A,rect.} = \frac{1}{12}(106.6mm)(256.05mm^3)$$

$$I_{A,rect.} = 2274.6mm^4$$

For $\sigma_{B,\ Plate}$:

$$\sigma_{B,Plate} = \frac{My}{I_{A,rect.}}$$

$$\sigma_{B,Plate} = \frac{(\ 120{,}980.2N \times mm)(3.175mm)}{2274.6mm^4}$$

$$\boldsymbol{\sigma_{B,Plate} = 168.9\ MPa}$$

APPENDIX VI.

PIN CALCULATIONS

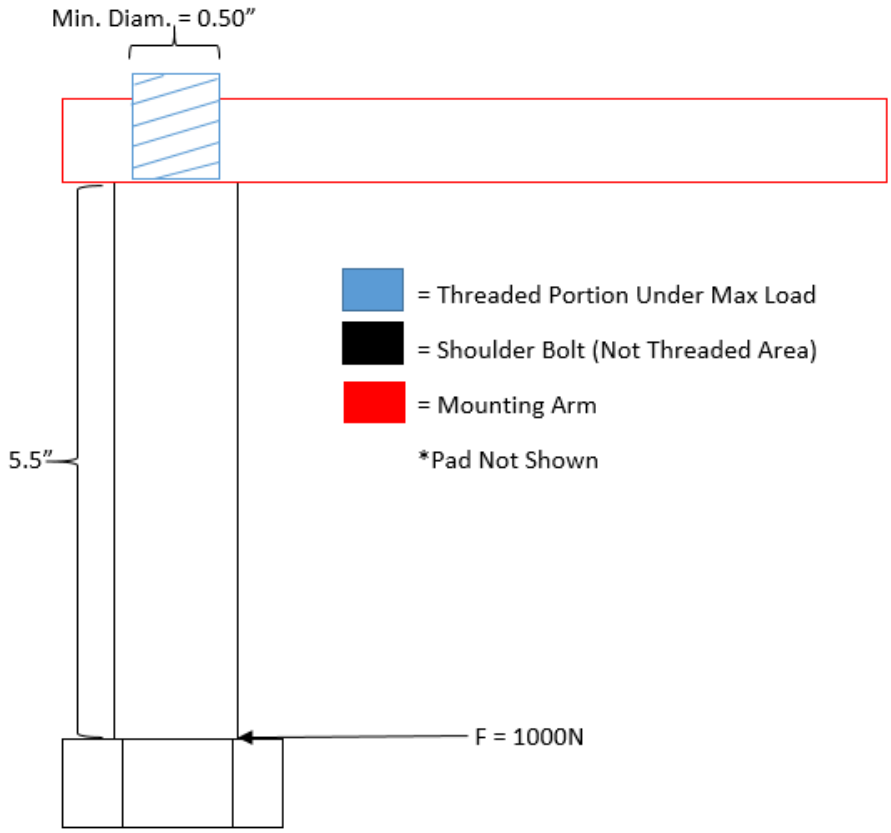

Bending Stress on Pin:

σ_B = Bending Stress

M = Moment Arm

F = Force

$d_{perpendicular}$ = Perpendicular Distance

y = Distance from Neutral Axis

$I_{A,\ Circle}$ = Area of Inertia for a Circle

r = Radius

$$\sigma_B = \frac{My}{I_A}\ \left(\frac{N}{mm^2}\ or\ MPa\right)$$

$$M = F \times d_{perpendicular}$$

$$I_{A,Circle} = \frac{1}{4}\pi r^4\ \ (mm^4)$$

Where:

$$1in = 25.4\ mm$$

$$d_{perpendicular} = 5.5in$$

$$d_{perpendicular} = 5.5in\ \left(\frac{25.4mm}{1in}\right)$$

$$d_{perpendicular} = 139.7mm$$

$$y\ =\ r\ =\ \frac{0.50in}{2}$$

$$r =\ 0.25in$$

$$r = 0.25in\ \left(\frac{25.4mm}{1in}\right)$$

$$r = 6.4mm$$

$$F = 1000N$$

For M:

$$M = F \times d_{perpendicular}$$

$$M = 1000N \times 139.7mm$$

$$M = 139{,}700\ N \times mm$$

For $I_{A,\ Circle}$:

$$I_{A,Circle} = \frac{1}{4}\pi r^4\ \ (mm^4)$$

$$I_{A,Circle} = \frac{1}{4}\pi(6.4mm)^4$$

$$I_{A,Circle} = \frac{1}{4}\pi(1677.7mm^4)$$

$$I_{A,Circle} = 1317.7\ mm^4$$

For $\sigma_{B,\ Pin}$:

$$\sigma_B = \frac{My}{I_A}$$

$$\sigma_{B,Pin} = \frac{(139{,}700\ N \times mm)(6.4mm)}{1317.7\ mm^4}$$

$$\sigma_{B,Pin} = 675.1\ MPa$$

Shear Stress on Pin:

τ_{Max} = Maximum Shear Stress

S = Shear Force

A_{Circle} = Area of Circle (Cross Section of Pin Where Under Max Load)

r = Radius

F = Force

$$\tau_{Max} = \frac{4}{3}\left(\frac{S}{A_{Circle}}\right)\ \left(\frac{N}{mm^2}\ or\ MPa\right)$$

$$A_{Circle} = \pi r^2\ \ (mm^2)$$

Where:

$$r = 6.4mm$$

$$S = F\ \ (N)$$

$$F = 1000N$$

For A_{Circle}:

$$A_{Circle} = \pi r^2\ \ (mm^2)$$

$$A_{Circle} = \pi(6.4\ mm)^2$$

$$A_{Circle} = 128.7\ mm^2$$

For τ_{Max}:

$$\tau_{Max} = \frac{4}{3}\left(\frac{S}{A_{Circle}}\right)\ \left(\frac{N}{mm^2}\ or\ MPa\right)$$

$$\tau_{Max} = \frac{4}{3}\left(\frac{1000N}{128.7mm^2}\right)$$

$$\tau_{Max} = \ 10.4\ MPa$$

Total Stress on Pin:

σ_P = Principal Stress

σ_B = Bending Stress

σ_x = Stress in x-direction

σ_y = Stress in y-direction

C = Center of Mohr's Circle

$$C = \frac{\sigma_x + \sigma_y}{2}\ (MPa)$$

$$C = \frac{675.1\ MPa + 0}{2}\ (MPa)$$

$$C = 337.6\ (MPa)$$

$$\sigma_P = \sqrt{(\sigma_B - C)^2 + (\tau_{Max})^2} + C\ \left(\frac{N}{mm^2}\ or\ MPa\right)$$

$$\sigma_P = \sqrt{(675.1\ MPa - 337.6\ MPa)^2 + (10.4\ MPa)^2} + 337.6\ MPa\ \left(\frac{N}{mm^2}\ or\ MPa\right)$$

$$\sigma_P = \sqrt{(337.5\ MPa)^2 + (10.4\ MPa)^2} + 337.6\ MPa\ \left(\frac{N}{mm^2}\ or\ MPa\right)$$

$$\sigma_P = \sqrt{113906.3\ MPa + 108.2\ MPa} + 337.6\ MPa\ \left(\frac{N}{mm^2}\ or\ MPa\right)$$

$$\sigma_P = \sqrt{114014.4\ MPa} + 337.6\ MPa\ \left(\frac{N}{mm^2}\ or\ MPa\right)$$

$$\sigma_P = 337.7\ MPa + 337.6\ MPa\ \left(\frac{N}{mm^2}\ or\ MPa\right)$$

$$\boldsymbol{\sigma_P = 675.3\ MPa\ \left(\frac{N}{mm^2}\ or\ MPa\right)}$$

Safety:

Max Stress of Pin = 965 MPa

Endurance = 1/3 Max = 322 MPa

Use σ_B eqn

$$\sigma_B = \frac{My}{I_A}$$

$$M = F \times d_{perpendicular}$$

$$\sigma_B = \frac{F \times d_{perpendicular} \times y}{I_A}$$

$$322\ MPa = \frac{450\ N \times d_{perpendicular} \times 6.4\ mm}{1317.7\ mm^4}$$

$$d_{perpendicular} = \frac{322\ MPa \times 1317.7\ mm^4}{450\ N\ \times 6.4\ mm}$$

$$\boldsymbol{d_{perpendicular} = 147.3\ mm}$$

APPENDIX VII.

QUASI-STATIC 1 GRAPHS

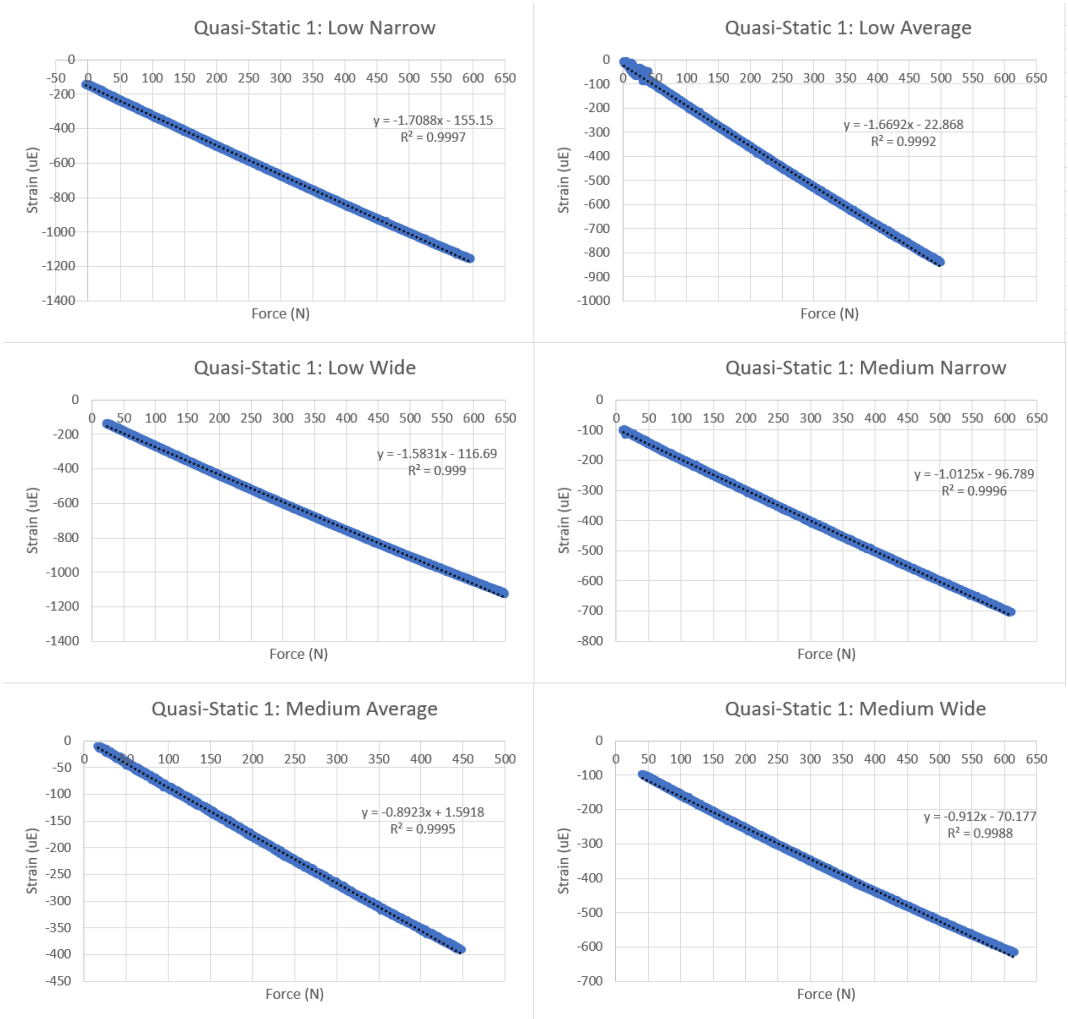

APPENDIX VIII.

PRELIMINARY 2 GRAPHS

* Only qualifying reps are graphed.

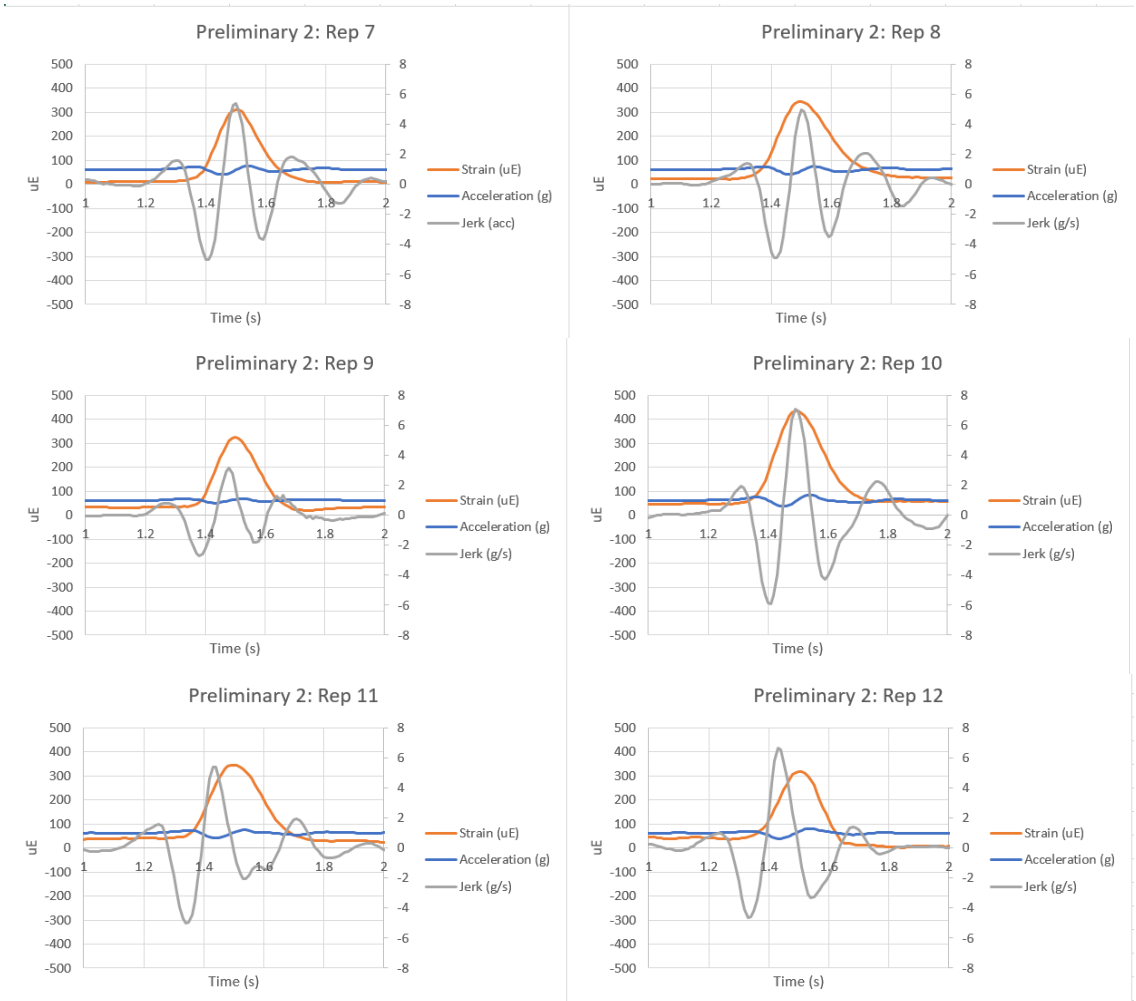

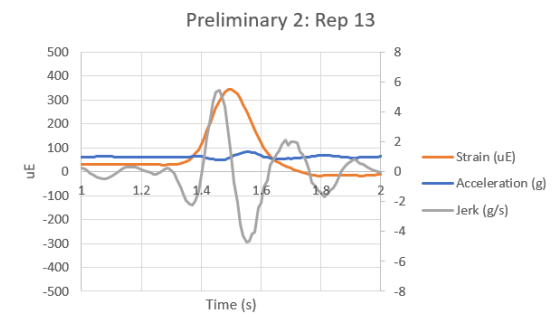
Preliminary 2: Rep 13
uE
Time (s)
Strain (uE)
Acceleration (g)
Jerk (g/s)

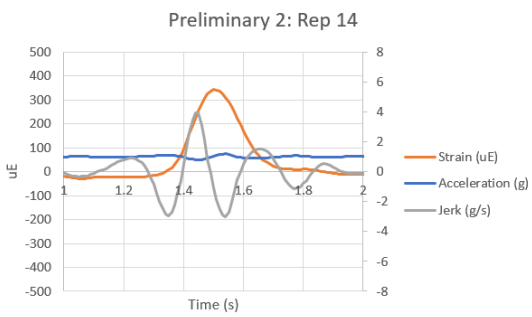
Preliminary 2: Rep 14
uE
Time (s)
Strain (uE)
Acceleration (g)
Jerk (g/s)

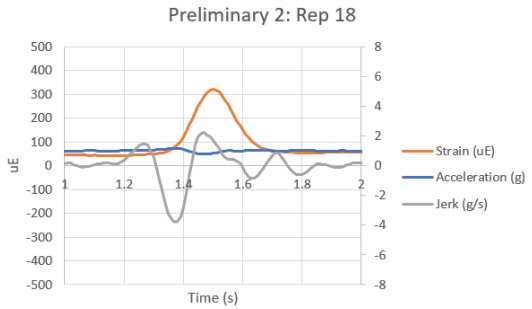
Preliminary 2: Rep 18
uE
Time (s)
Strain (uE)
Acceleration (g)
Jerk (g/s)

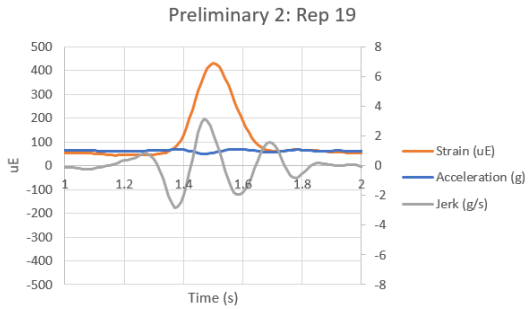
Preliminary 2: Rep 19
uE
Time (s)
Strain (uE)
Acceleration (g)
Jerk (g/s)

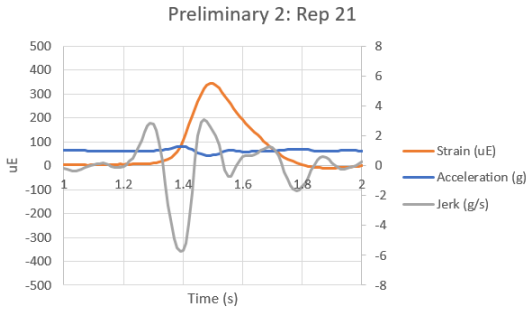
Preliminary 2: Rep 21
uE
Time (s)
Strain (uE)
Acceleration (g)
Jerk (g/s)

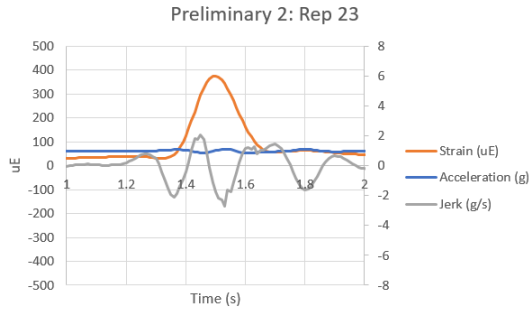
Preliminary 2: Rep 23
uE
Time (s)
Strain (uE)
Acceleration (g)
Jerk (g/s)

APPENDIX IX.

PRELIMINARY 3 GRAPHS

* Only qualifying reps are graphed.

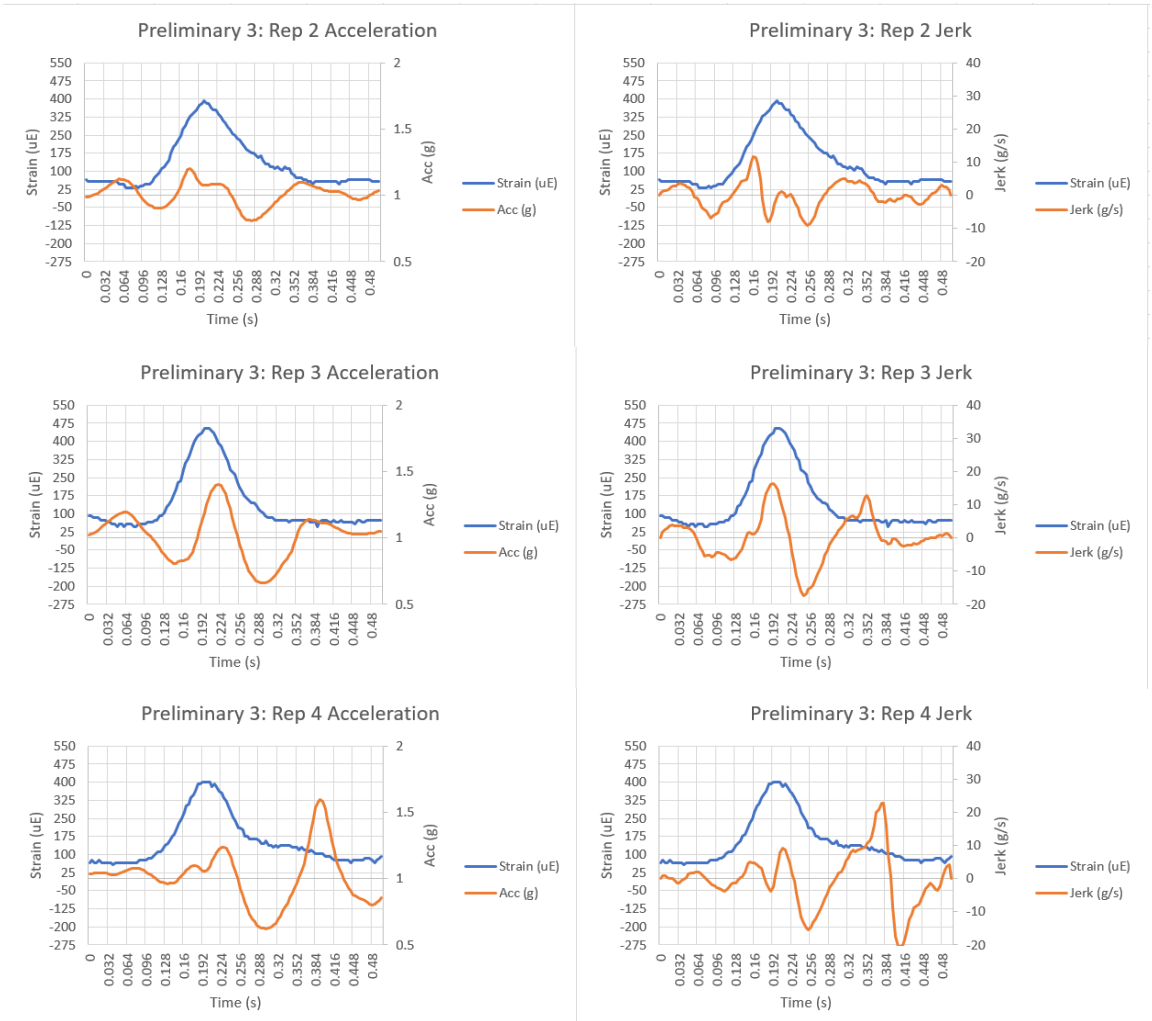

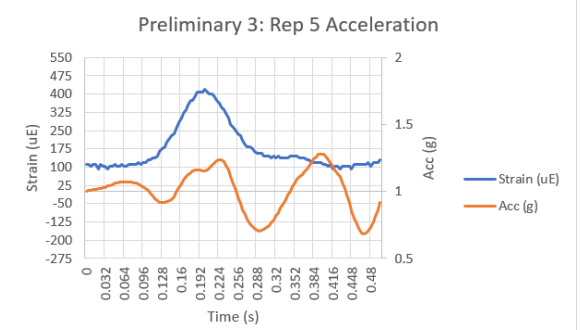
Preliminary 3: Rep 5 Acceleration
Strain (uE)
Acc (g)
Time (s)

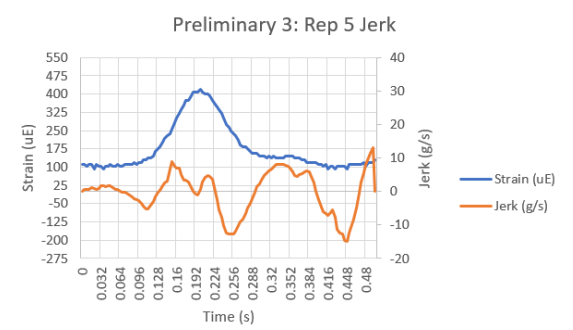
Preliminary 3: Rep 5 Jerk
Strain (uE)
Jerk (g/s)
Time (s)

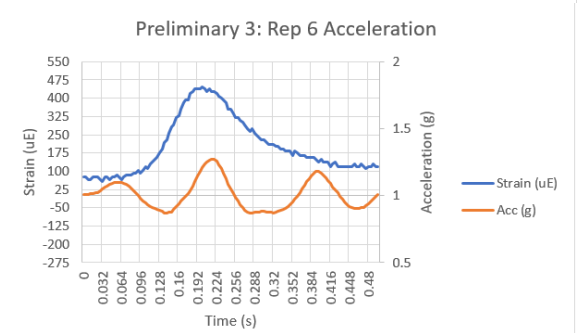
Preliminary 3: Rep 6 Acceleration
Strain (uE)
Acceleration (g)
Acc (g)
Time (s)

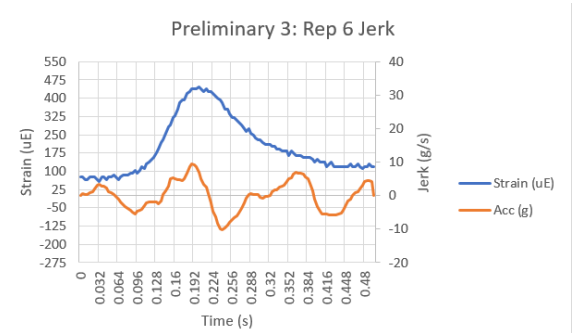
Preliminary 3: Rep 6 Jerk
Strain (uE)
Jerk (g/s)
Acc (g)
Time (s)

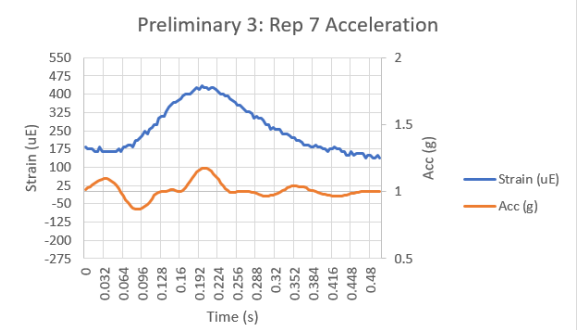
Preliminary 3: Rep 7 Acceleration
Strain (uE)
Acc (g)
Time (s)

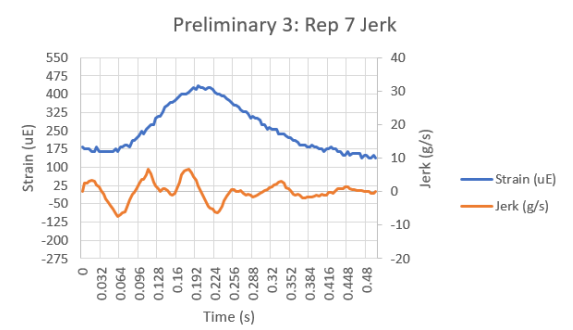
Preliminary 3: Rep 7 Jerk
Strain (uE)
Jerk (g/s)
Time (s)

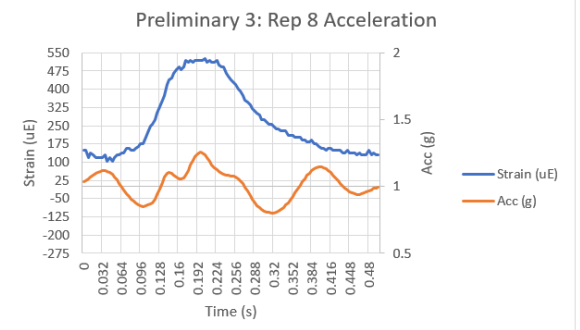
Preliminary 3: Rep 8 Acceleration
Strain (uE)
Acc (g)
Time (s)

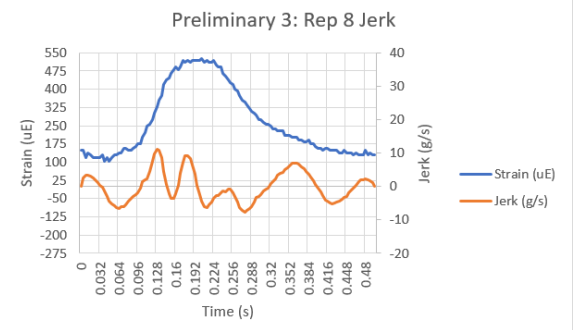
Preliminary 3: Rep 8 Jerk
Strain (uE)
Jerk (g/s)
Time (s)

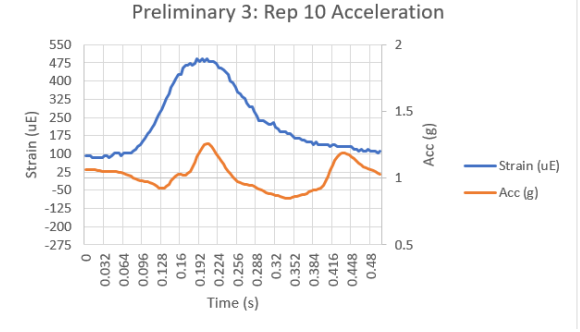
Preliminary 3: Rep 10 Acceleration
Strain (uE)
Acc (g)
Time (s)

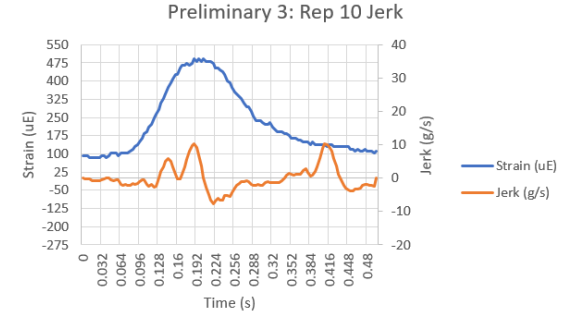
Preliminary 3: Rep 10 Jerk
Strain (uE)
Jerk (g/s)
Time (s)

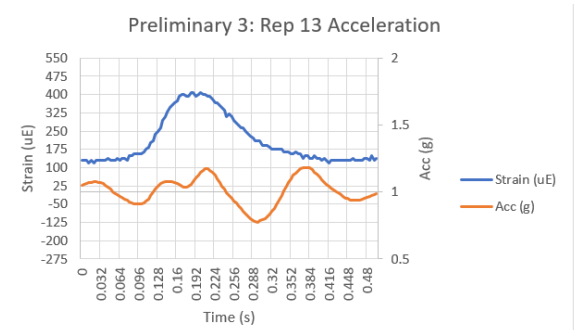
Preliminary 3: Rep 13 Acceleration
Strain (uE)
Acc (g)
Time (s)

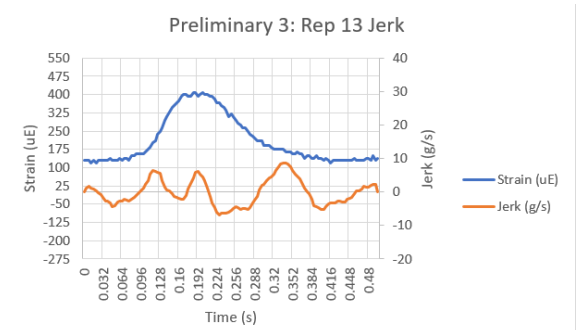
Preliminary 3: Rep 13 Jerk
Strain (uE)
Jerk (g/s)
Time (s)

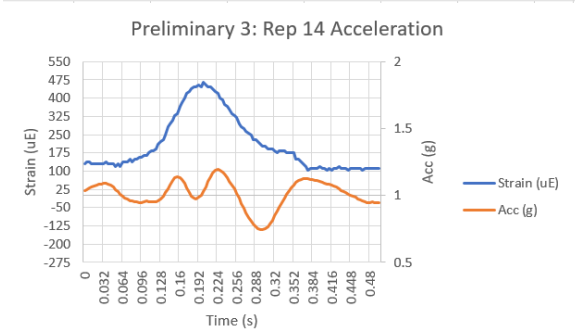
Preliminary 3: Rep 14 Acceleration
Strain (uE)
Acc (g)
Time (s)

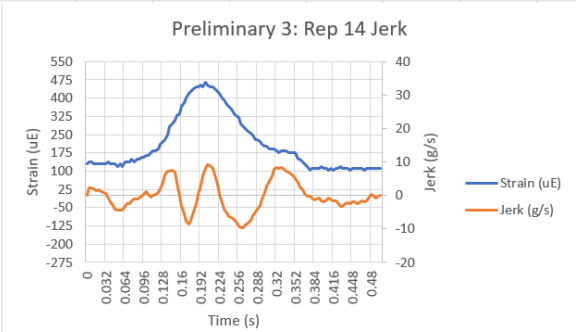
Preliminary 3: Rep 14 Jerk
Strain (uE)
Jerk (g/s)
Time (s)

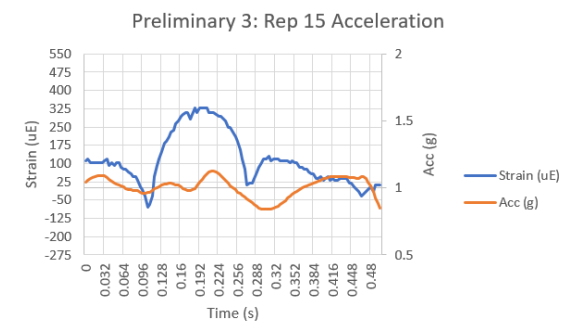
Preliminary 3: Rep 15 Acceleration
Strain (uE)
Acc (g)
Time (s)

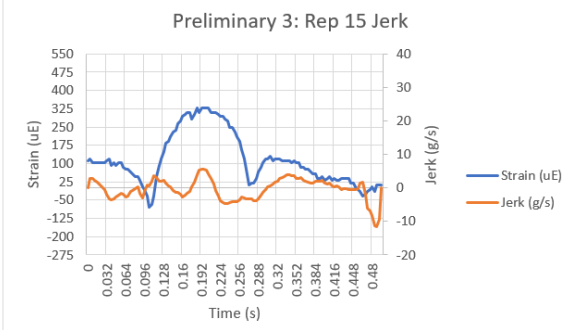
Preliminary 3: Rep 15 Jerk
Strain (uE)
Jerk (g/s)
Time (s)

APPENDIX X.

QUASI-STATIC 2 GRAPHS

*Blue is measured strain while Orange is true strain with removed offset.

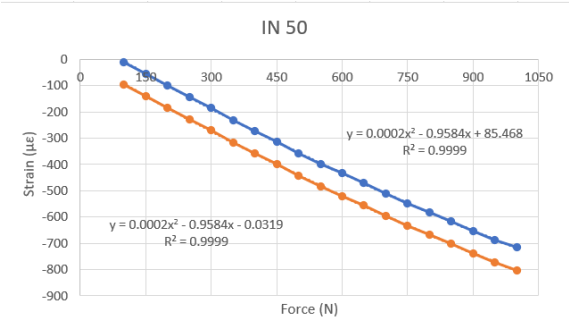

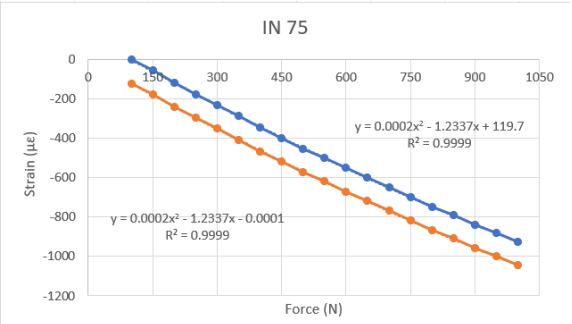

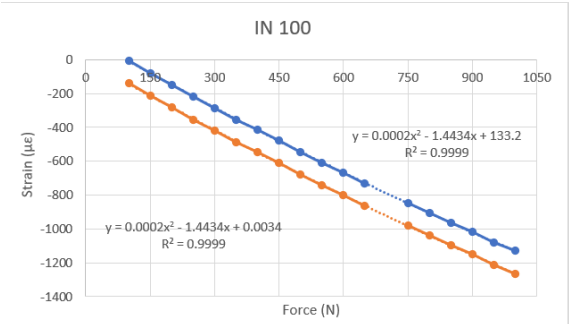

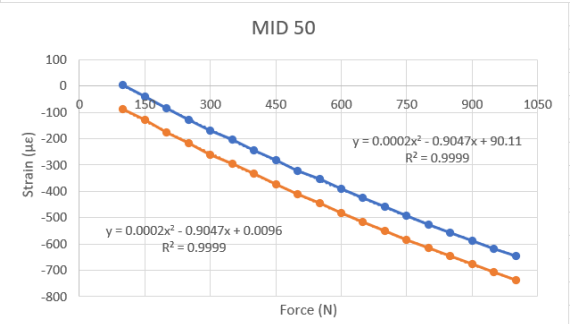

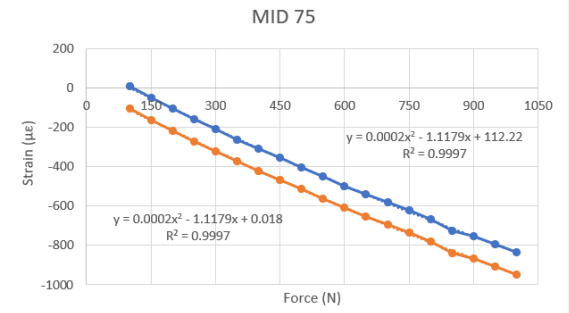

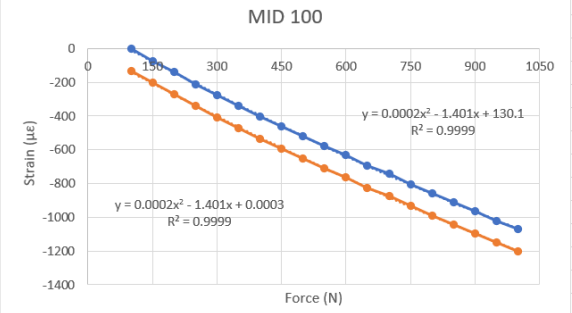

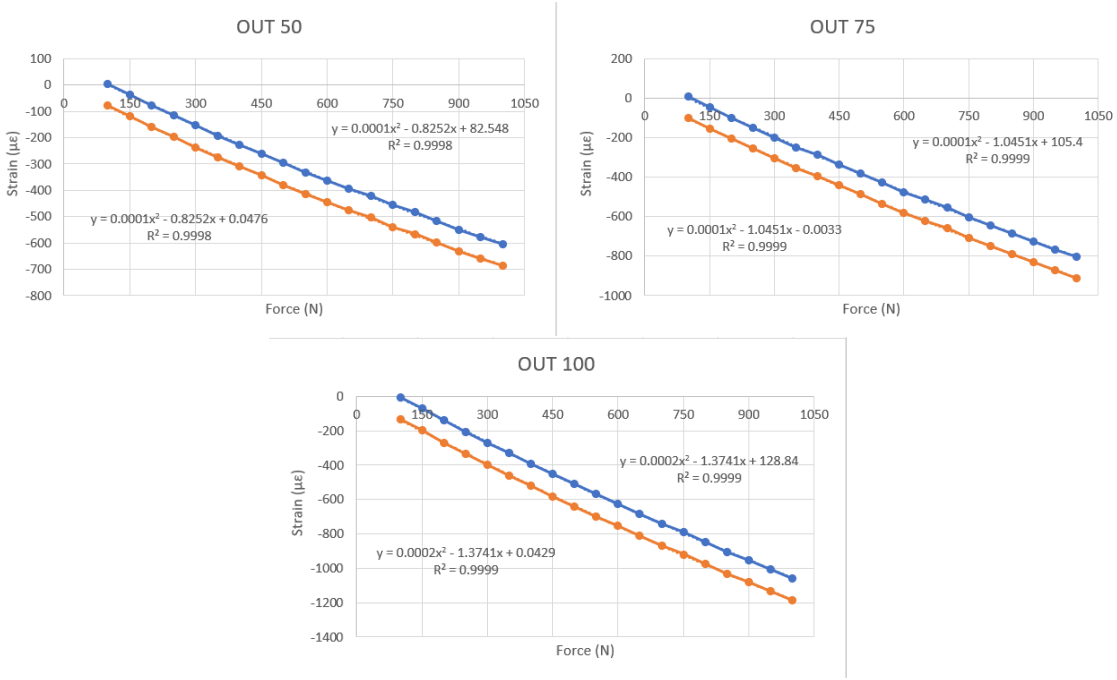
OUT 50
Strain (με)
Force (N)
y = 0.0001x² - 0.8252x + 82.548
R² = 0.9998
y = 0.0001x² - 0.8252x + 0.0476
R² = 0.9998
OUT 75
Strain (με)
Force (N)
y = 0.0001x² - 1.0451x + 105.4
R² = 0.9999
y = 0.0001x² - 1.0451x - 0.0033
R² = 0.9999
OUT 100
Strain (με)
Force (N)
y = 0.0002x² - 1.3741x + 128.84
R² = 0.9999
y = 0.0002x² - 1.3741x + 0.0429
R² = 0.9999

APPENDIX XI.

ARM FACTOR GRAPHS

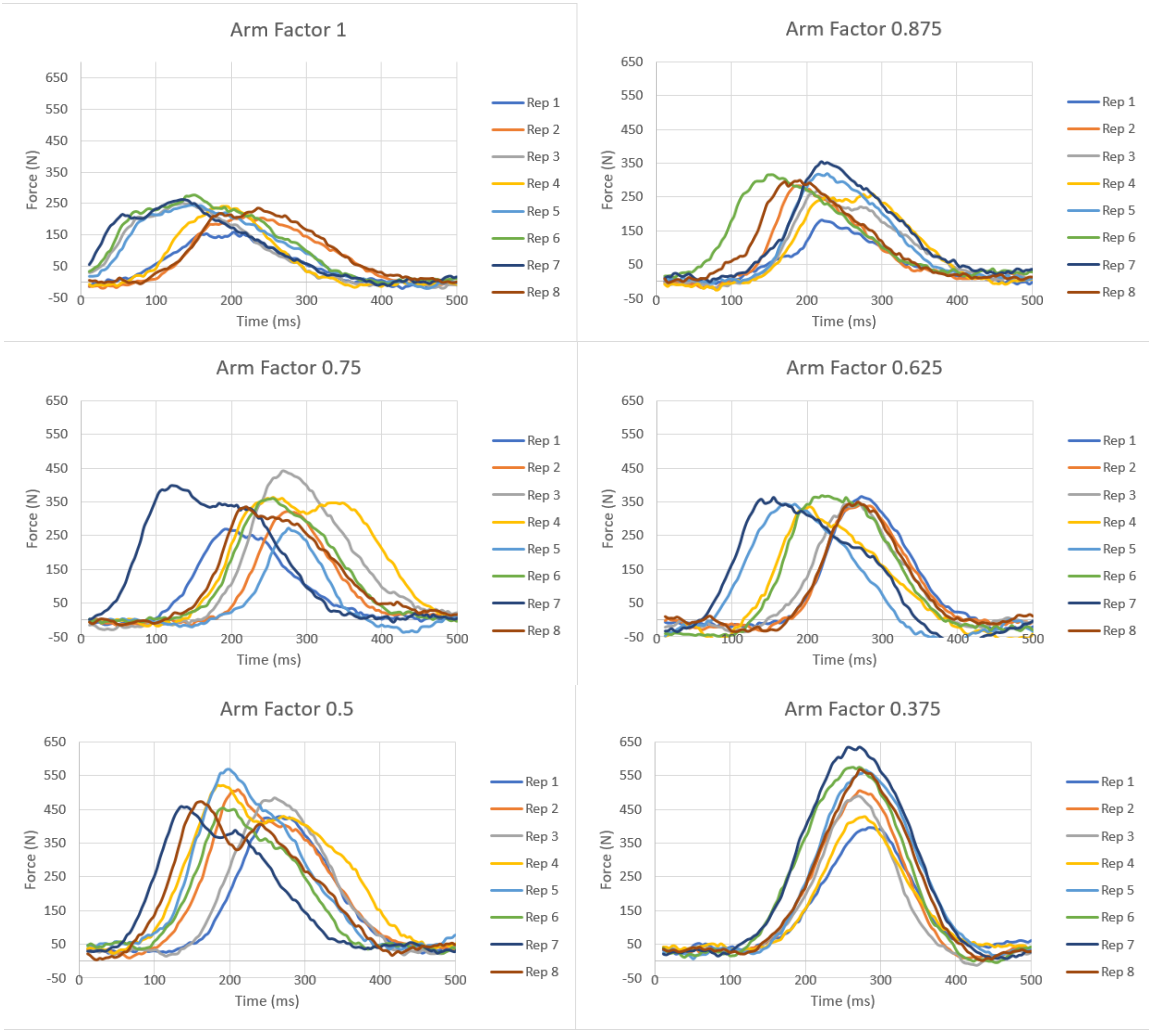

APPENDIX XII.

ABDUCTION INSTRUCTION GRAPHS

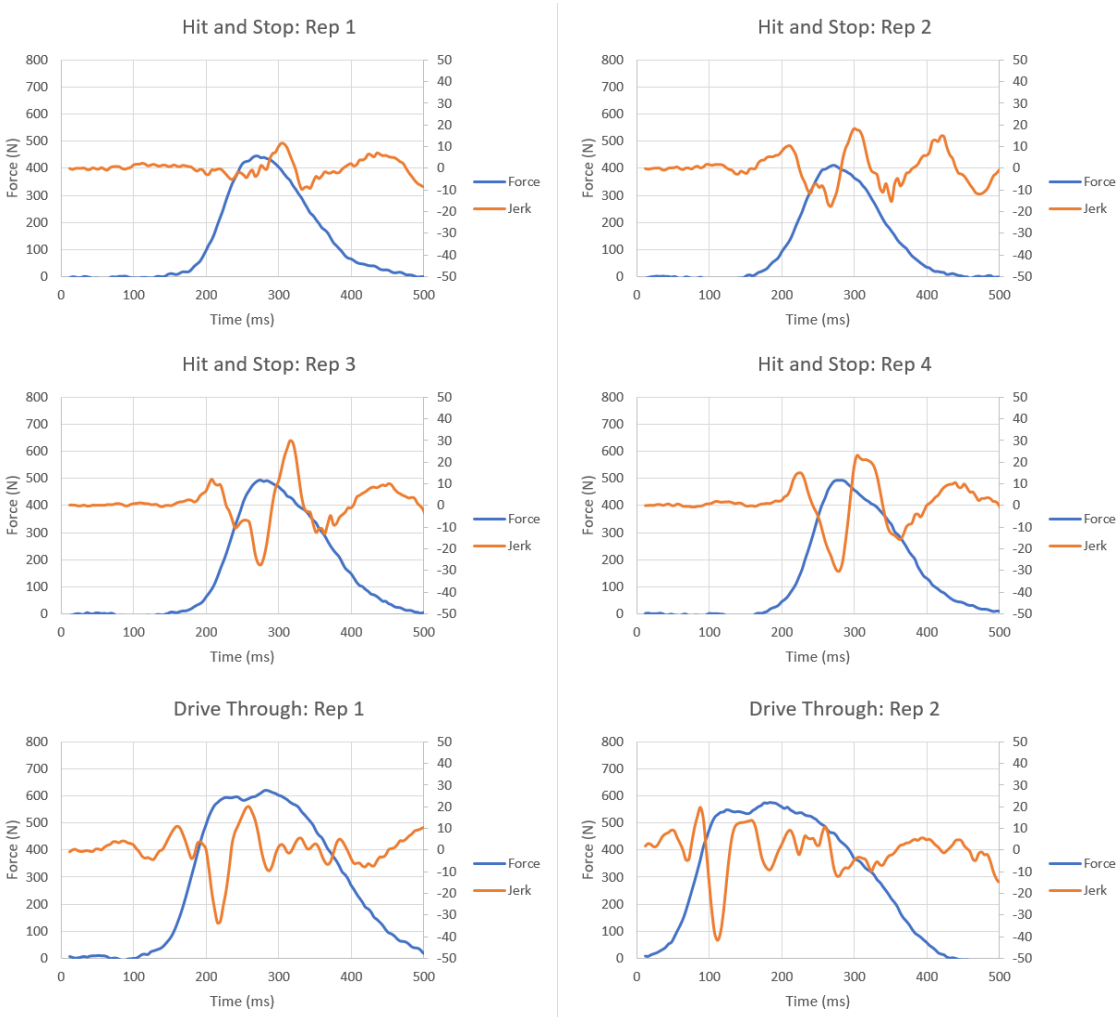

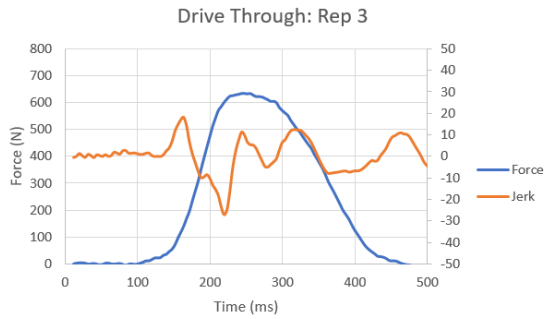
Drive Through: Rep 3
Force (N)
Time (ms)
Force
Jerk

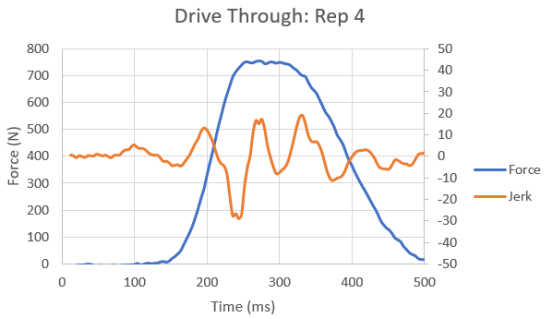
Drive Through: Rep 4
Force (N)
Time (ms)
Force
Jerk

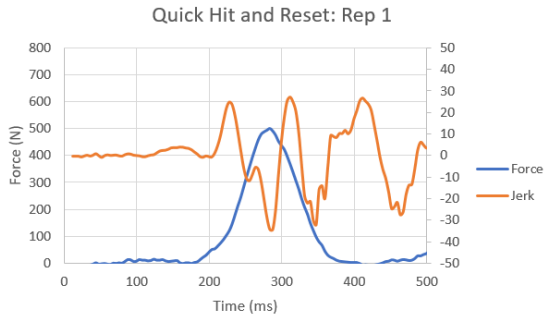
Quick Hit and Reset: Rep 1
Force (N)
Time (ms)
Force
Jerk

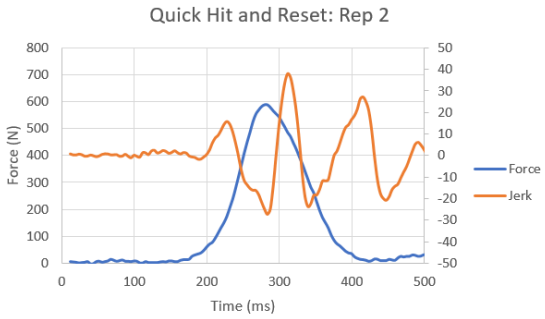
Quick Hit and Reset: Rep 2
Force (N)
Time (ms)
Force
Jerk

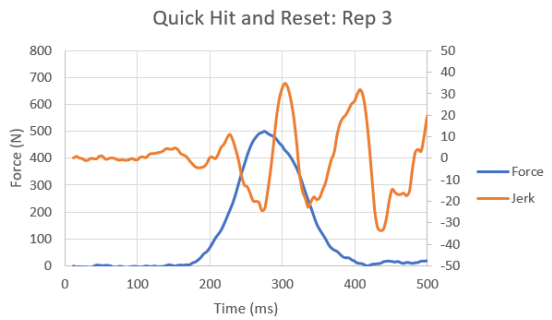
Quick Hit and Reset: Rep 3
Force (N)
Time (ms)
Force
Jerk

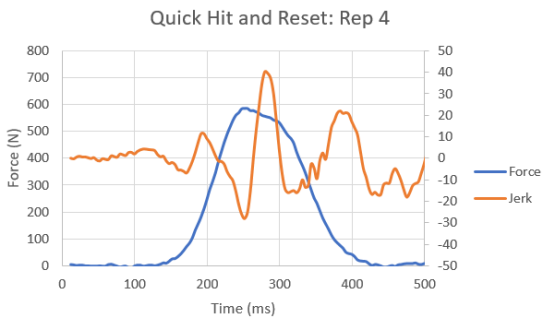
Quick Hit and Reset: Rep 4
Force (N)
Time (ms)
Force
Jerk

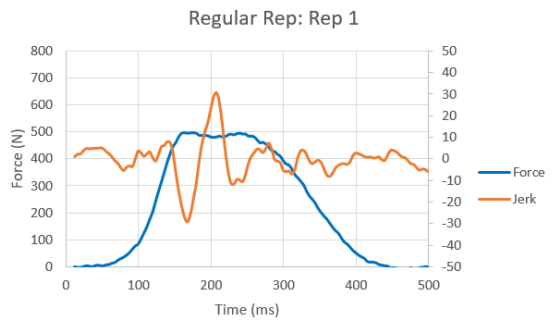
Regular Rep: Rep 1
Force (N)
Time (ms)
Force
Jerk

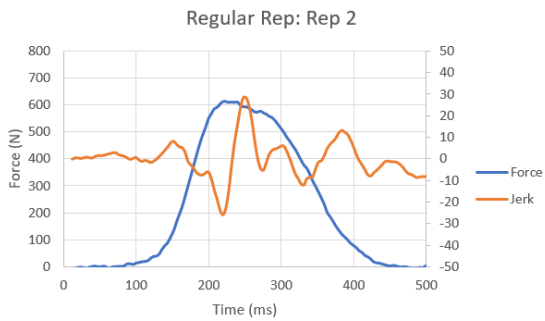
Regular Rep: Rep 2
Force (N)
Time (ms)
Force
Jerk

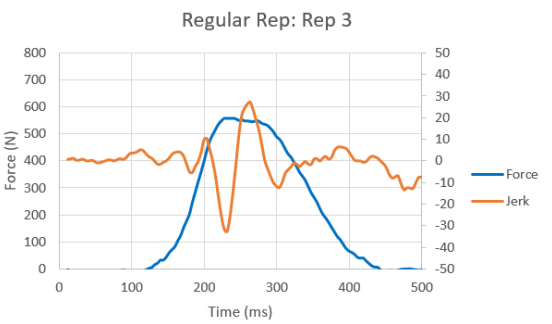
Regular Rep: Rep 3
Force (N)
Time (ms)
Force
Jerk

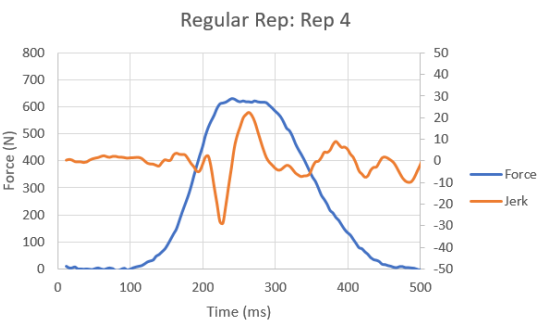
Regular Rep: Rep 4
Force (N)
Time (ms)
Force
Jerk

APPENDIX XIII.

GRIP INSTRUCTION GRAPHS

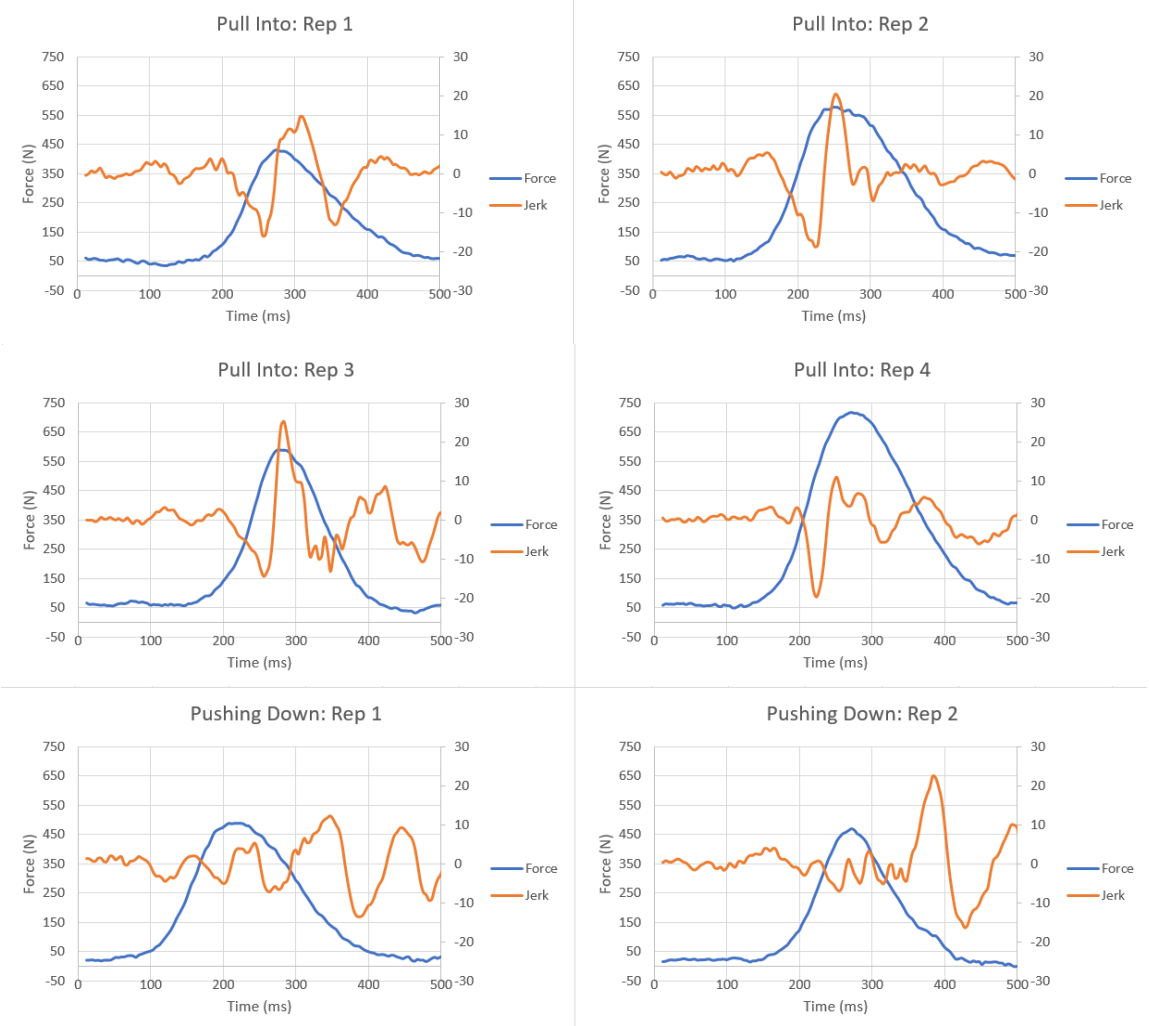

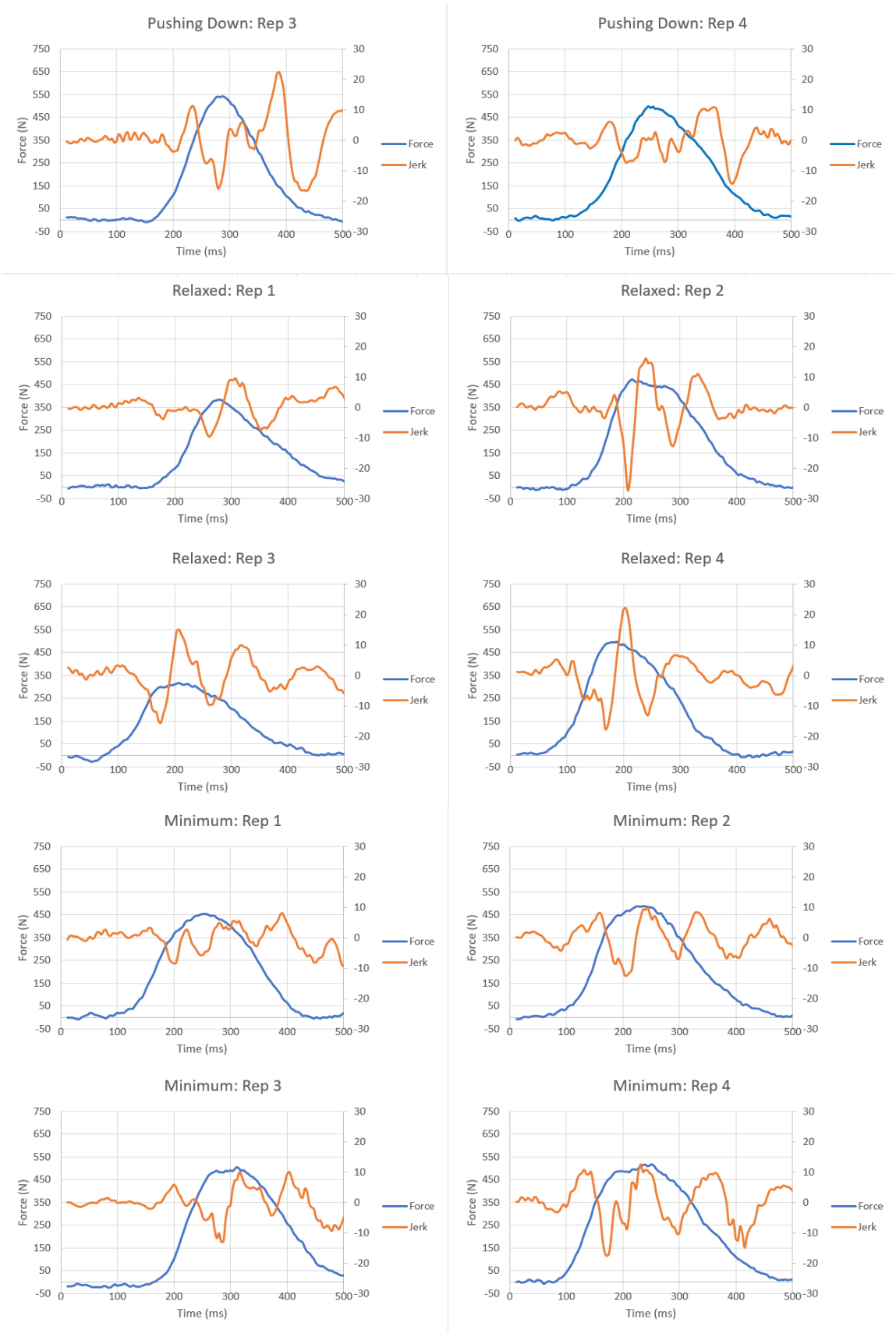
Pushing Down: Rep 3
Pushing Down: Rep 4
Relaxed: Rep 1
Relaxed: Rep 2
Relaxed: Rep 3
Relaxed: Rep 4
Minimum: Rep 1
Minimum: Rep 2
Minimum: Rep 3
Minimum: Rep 4
Force (N)
Time (ms)
Force
Jerk

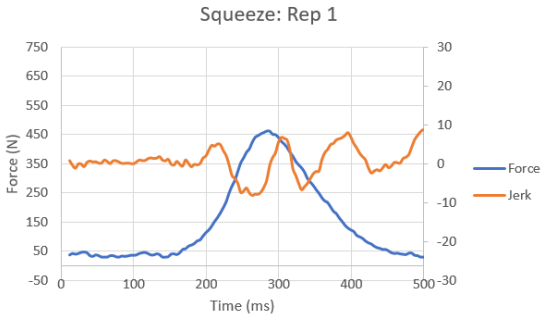
Squeeze: Rep 1
Force (N)
Time (ms)
Force
Jerk

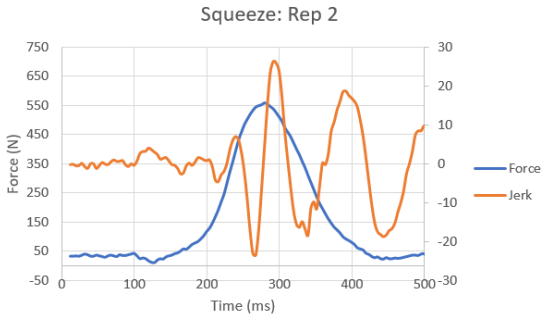
Squeeze: Rep 2
Force (N)
Time (ms)
Force
Jerk


Squeeze: Rep 3
Force (N)
Time (ms)
Force
Jerk

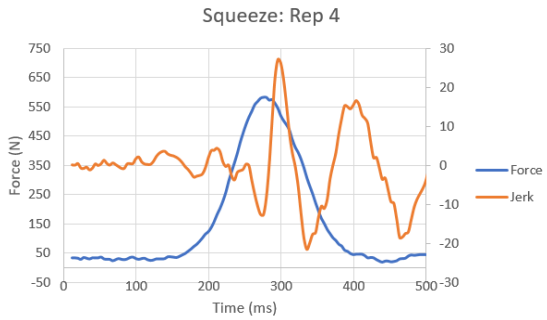
Squeeze: Rep 4
Force (N)
Time (ms)
Force
Jerk

APPENDIX XIV.

METRONOME GRAPHS

* Only unique data graphed.

* Threshold data (40-80 BPM) is plotted to 0.5s while complete data (100-140 BPM) is plotted to 0.25s.

* Reps 2 and 6 of 140 BPM have unique jerk axes.

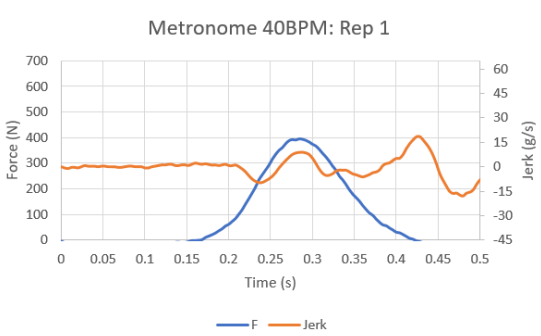

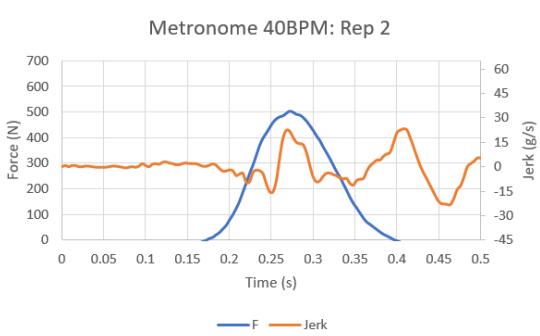

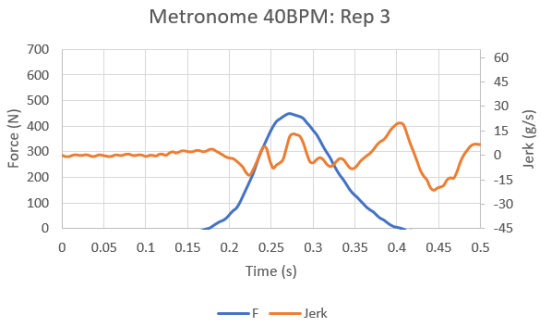

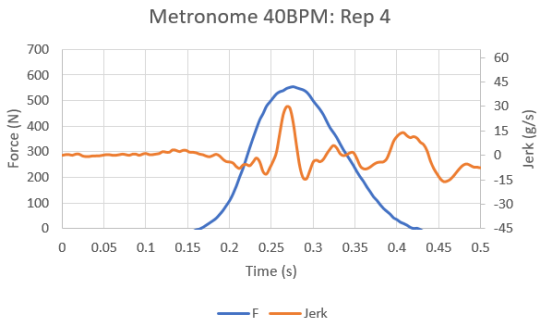

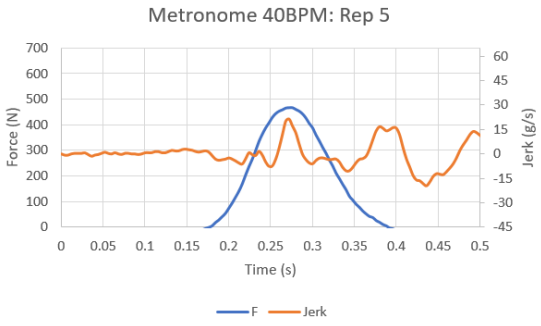

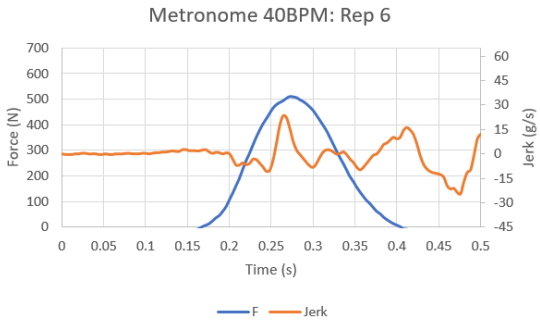

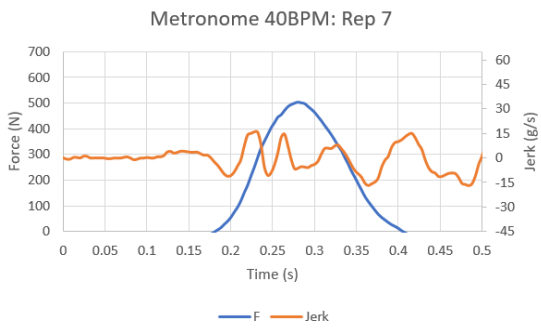
Metronome 40BPM: Rep 7
Force (N)
Jerk (g/s)
Time (s)
F
Jerk

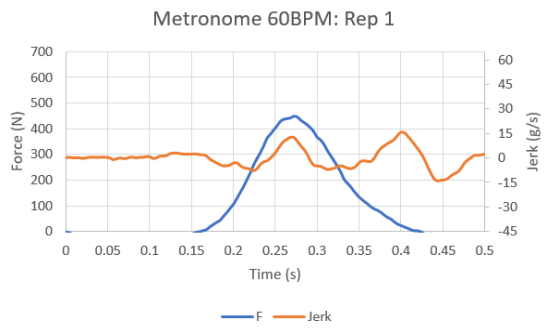
Metronome 60BPM: Rep 1
Force (N)
Jerk (g/s)
Time (s)
F
Jerk

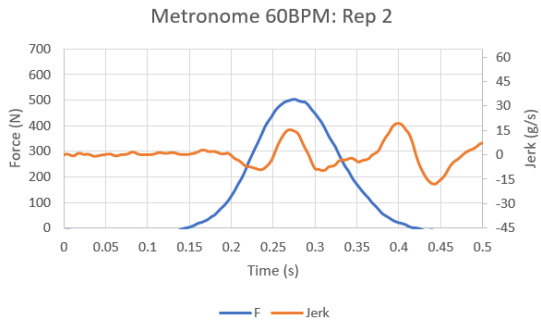
Metronome 60BPM: Rep 2
Force (N)
Jerk (g/s)
Time (s)
F
Jerk

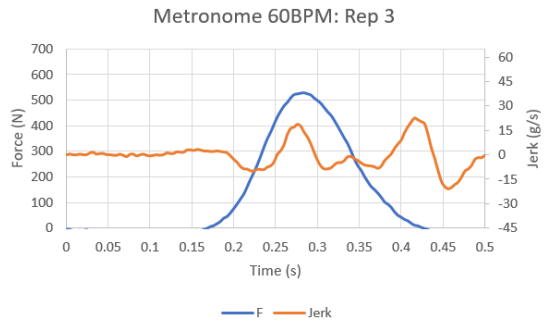
Metronome 60BPM: Rep 3
Force (N)
Jerk (g/s)
Time (s)
F
Jerk

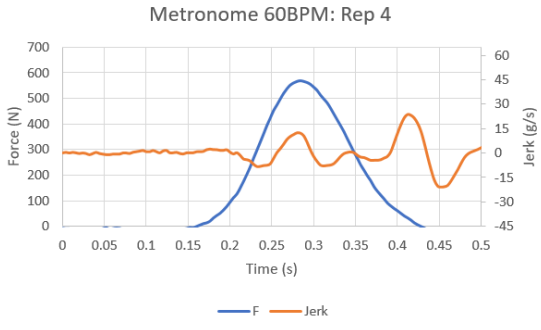
Metronome 60BPM: Rep 4
Force (N)
Jerk (g/s)
Time (s)
F
Jerk

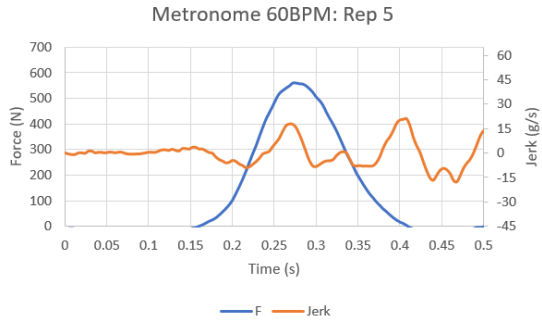
Metronome 60BPM: Rep 5
Force (N)
Jerk (g/s)
Time (s)
F
Jerk

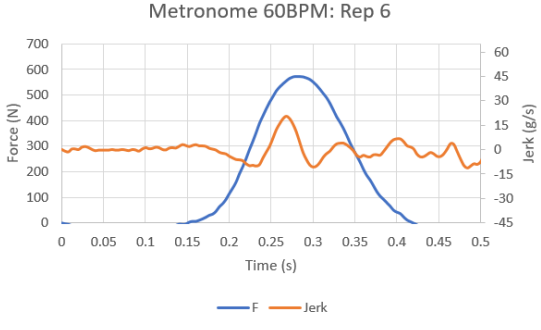
Metronome 60BPM: Rep 6
Force (N)
Jerk (g/s)
Time (s)
F
Jerk

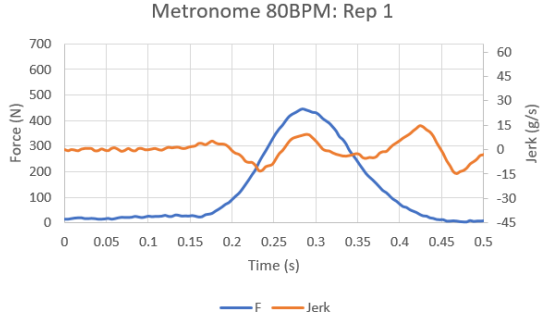
Metronome 80BPM: Rep 1
Force (N)
Jerk (g/s)
Time (s)
F
Jerk

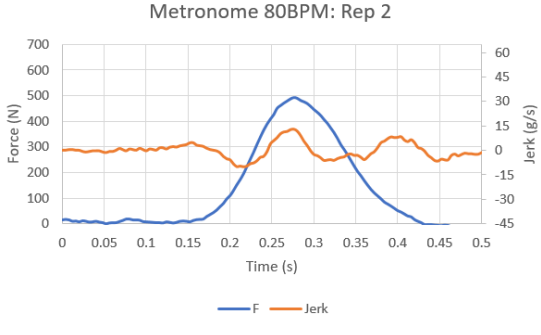
Metronome 80BPM: Rep 2
Force (N)
Jerk (g/s)
Time (s)
F
Jerk

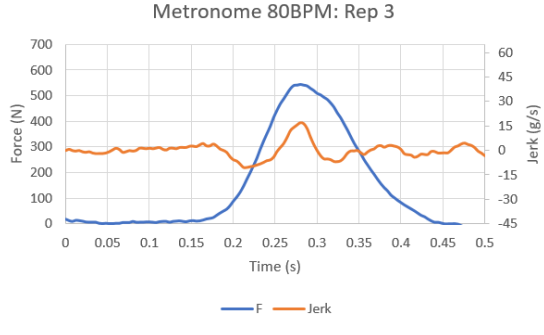
Metronome 80BPM: Rep 3
Force (N)
Jerk (g/s)
Time (s)
F
Jerk

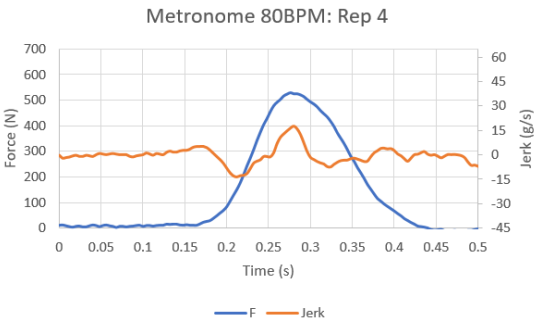
Metronome 80BPM: Rep 4
Force (N)
Jerk (g/s)
Time (s)
F
Jerk

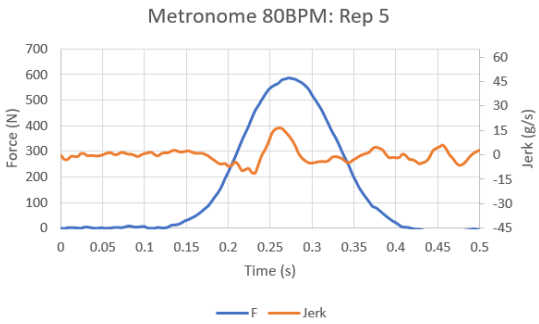
Metronome 80BPM: Rep 5
Force (N)
Jerk (g/s)
Time (s)
F
Jerk

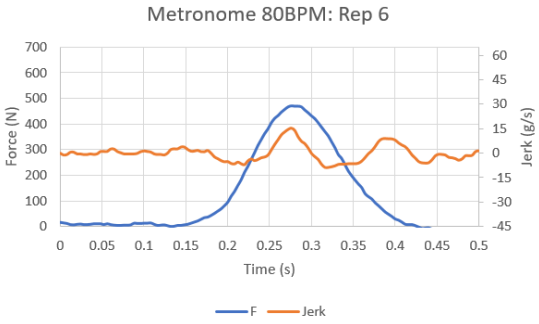
Metronome 80BPM: Rep 6
Force (N)
Jerk (g/s)
Time (s)
F
Jerk

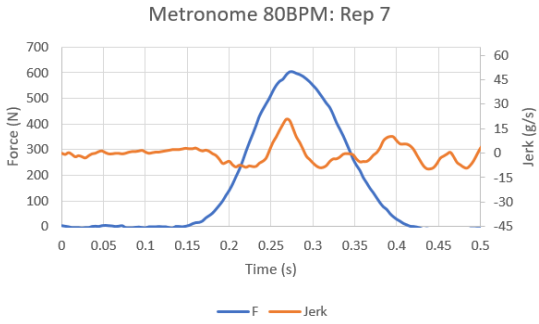
Metronome 80BPM: Rep 7
Force (N)
Jerk (g/s)
Time (s)
F
Jerk

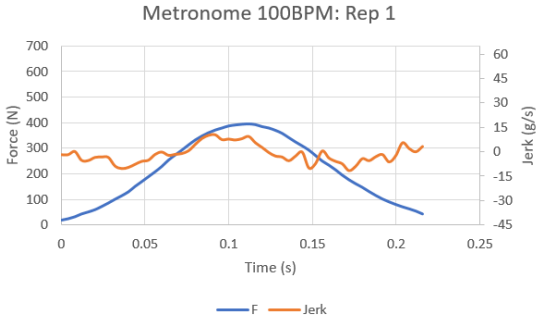
Metronome 100BPM: Rep 1
Force (N)
Jerk (g/s)
Time (s)
F
Jerk

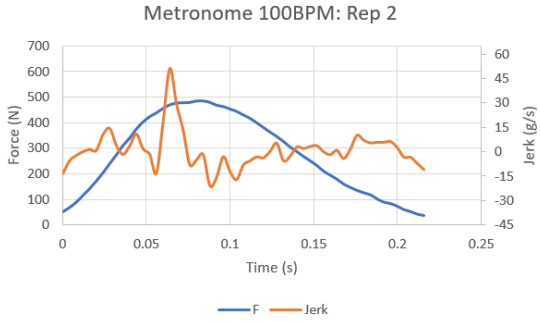
Metronome 100BPM: Rep 2
Force (N)
Jerk (g/s)
Time (s)
F
Jerk

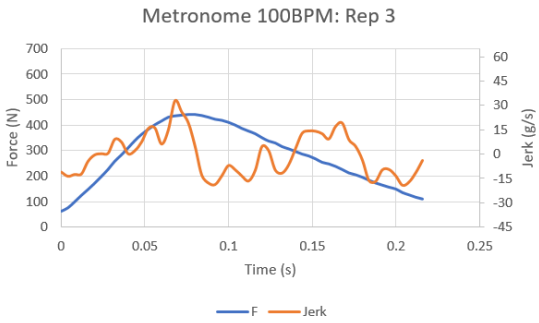
Metronome 100BPM: Rep 3
Force (N)
Jerk (g/s)
Time (s)
F
Jerk

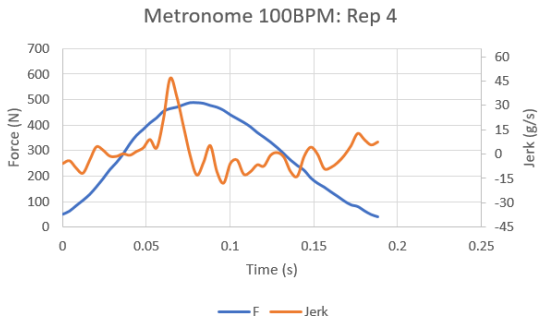
Metronome 100BPM: Rep 4
Force (N)
Jerk (g/s)
Time (s)
F
Jerk

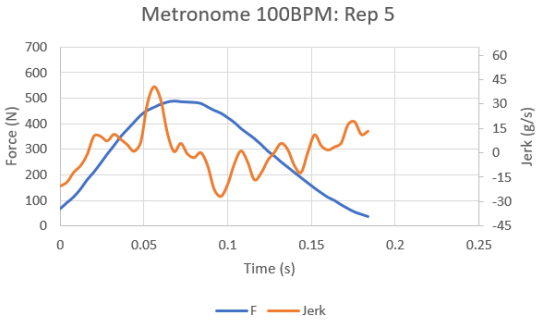
Metronome 100BPM: Rep 5
Force (N)
Jerk (g/s)
Time (s)
F
Jerk

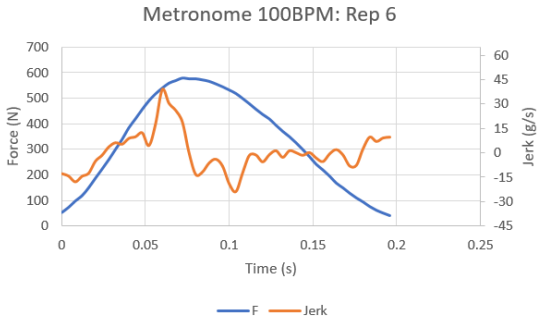
Metronome 100BPM: Rep 6
Force (N)
Jerk (g/s)
Time (s)
F
Jerk

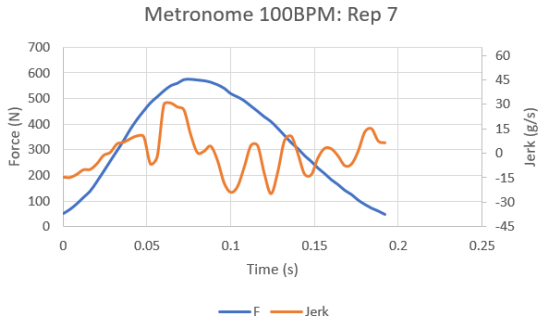
Metronome 100BPM: Rep 7
Force (N)
Jerk (g/s)
Time (s)
F
Jerk

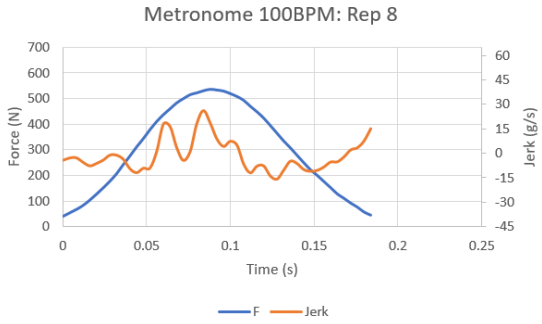
Metronome 100BPM: Rep 8
Force (N)
Jerk (g/s)
Time (s)
F
Jerk

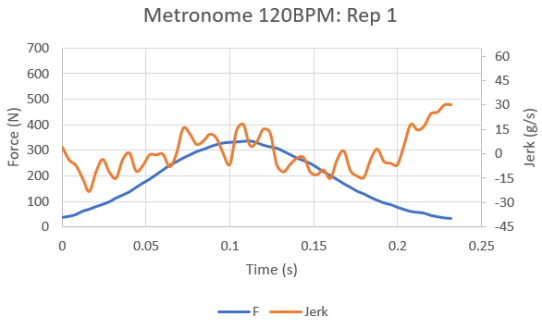
Metronome 120BPM: Rep 1
Force (N)
Jerk (g/s)
Time (s)
F
Jerk

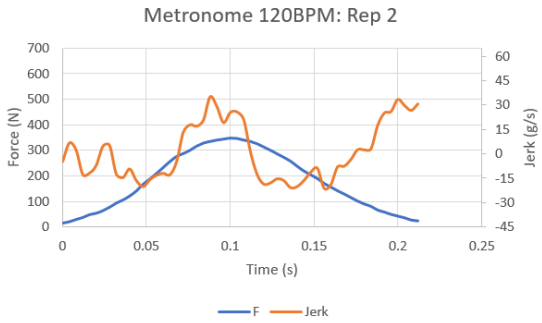
Metronome 120BPM: Rep 2
Force (N)
Jerk (g/s)
Time (s)
F
Jerk

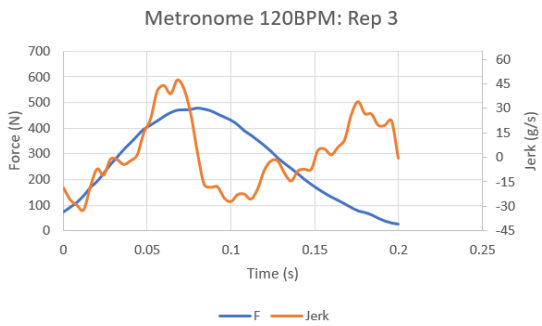
Metronome 120BPM: Rep 3
Force (N)
Jerk (g/s)
Time (s)
F
Jerk

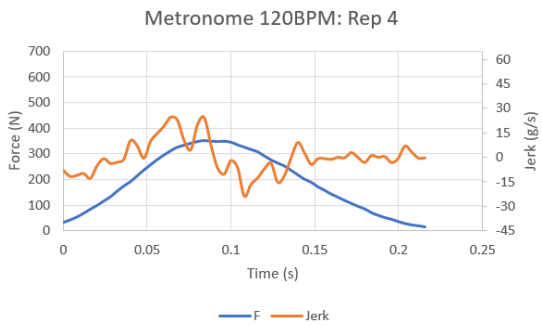
Metronome 120BPM: Rep 4
Force (N)
Jerk (g/s)
Time (s)
F
Jerk

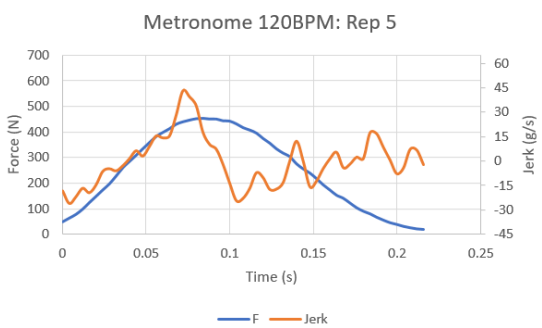
Metronome 120BPM: Rep 5
Force (N)
Jerk (g/s)
Time (s)
F
Jerk

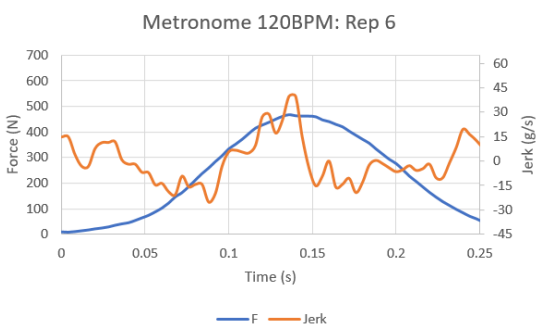
Metronome 120BPM: Rep 6
Force (N)
Jerk (g/s)
Time (s)
F
Jerk

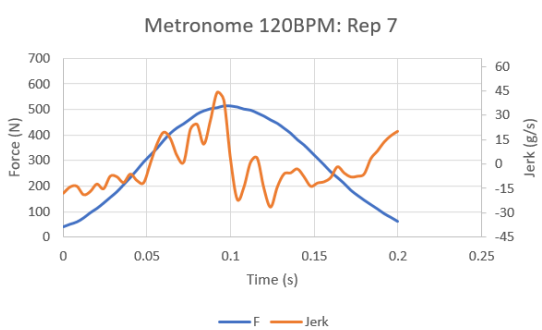
Metronome 120BPM: Rep 7
Force (N)
Jerk (g/s)
Time (s)
F
Jerk

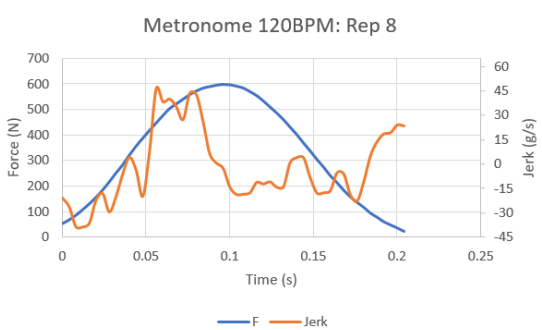
Metronome 120BPM: Rep 8
Force (N)
Jerk (g/s)
Time (s)
F
Jerk

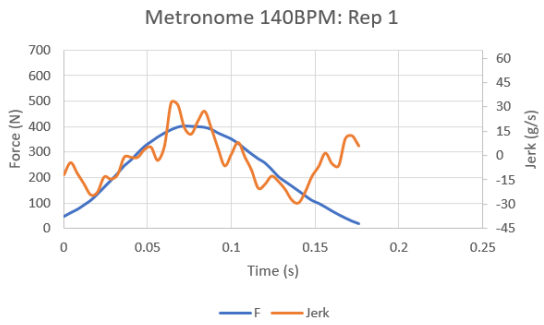
Metronome 140BPM: Rep 1
Force (N)
Jerk (g/s)
Time (s)
F
Jerk

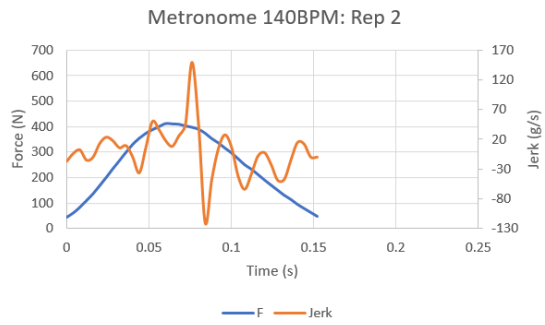
Metronome 140BPM: Rep 2
Force (N)
Jerk (g/s)
Time (s)
F
Jerk

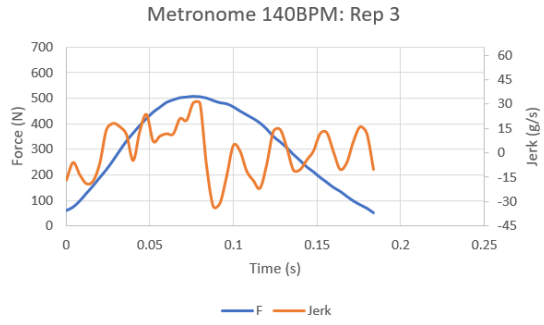
Metronome 140BPM: Rep 3
Force (N)
Jerk (g/s)
Time (s)
F
Jerk

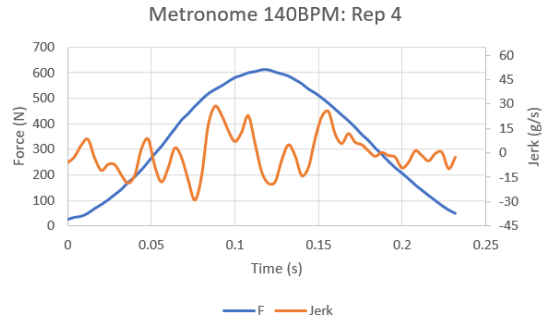
Metronome 140BPM: Rep 4
Force (N)
Jerk (g/s)
Time (s)
F
Jerk

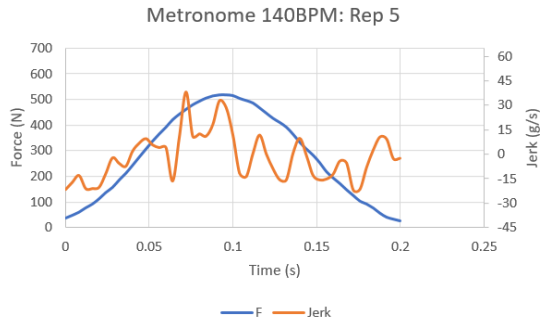
Metronome 140BPM: Rep 5
Force (N)
Jerk (g/s)
Time (s)
F
Jerk

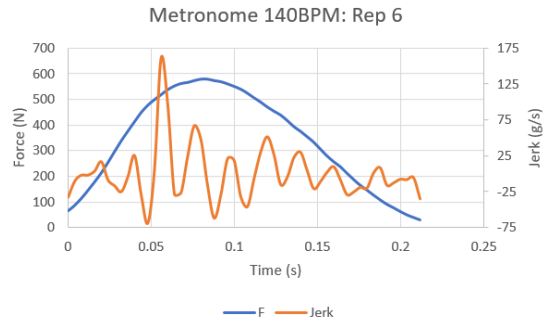
Metronome 140BPM: Rep 6
Force (N)
Jerk (g/s)
Time (s)
F
Jerk

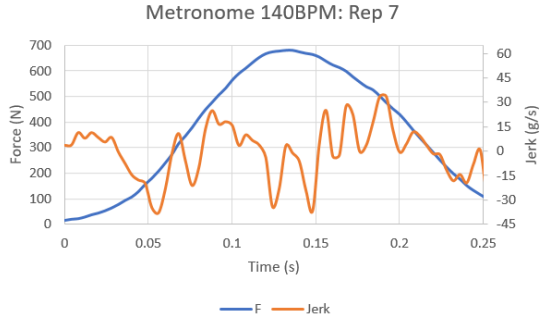
Metronome 140BPM: Rep 7
Force (N)
Jerk (g/s)
Time (s)
F
Jerk

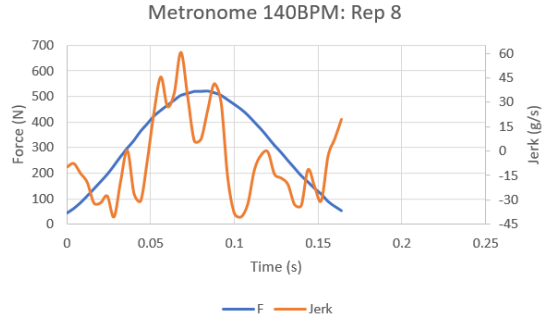
Metronome 140BPM: Rep 8
Force (N)
Jerk (g/s)
Time (s)
F
Jerk

APPENDIX XV.

VOLUNTEER 1 GRAPHS

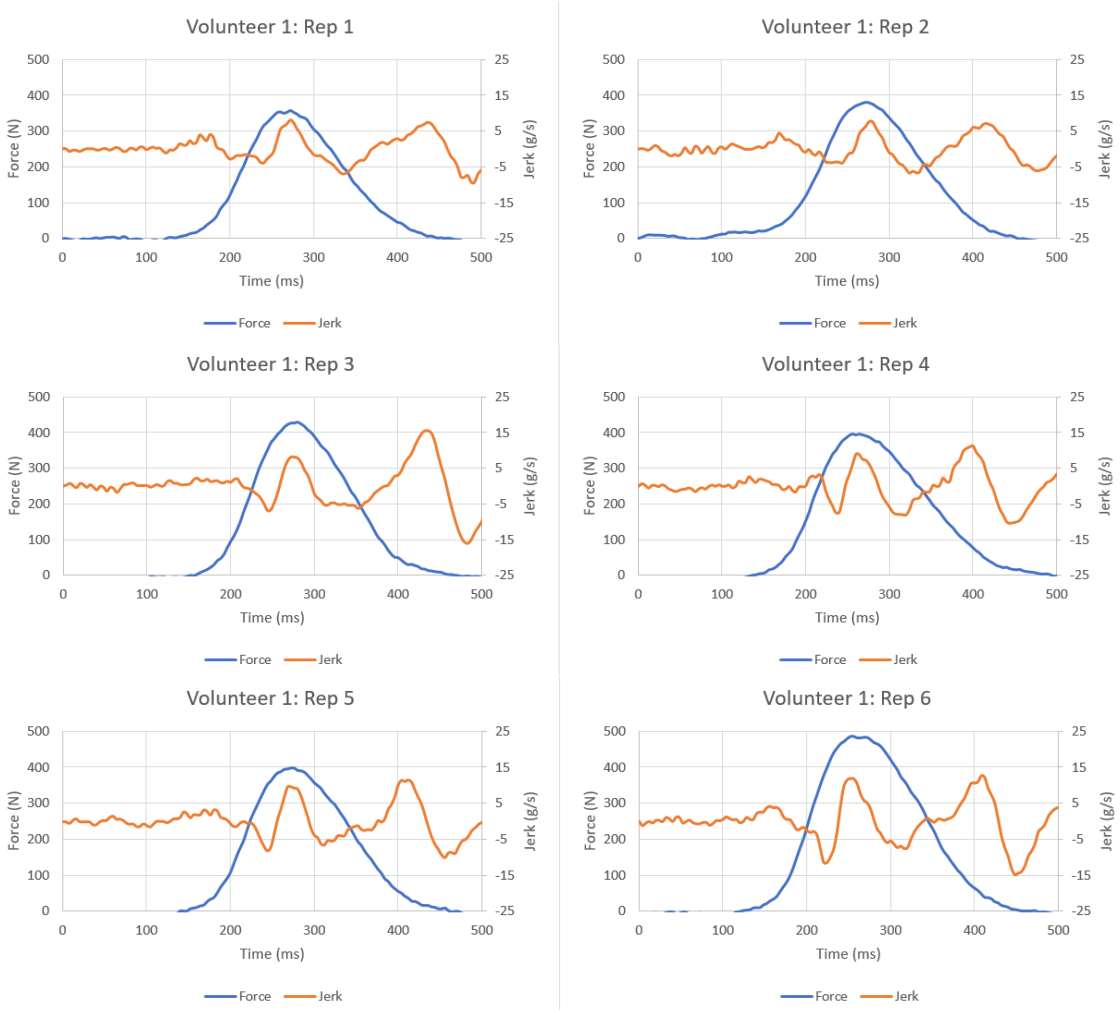

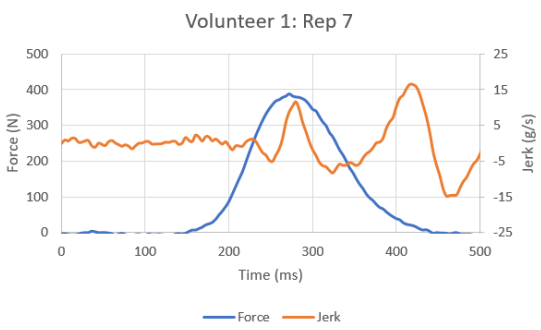
Volunteer 1: Rep 7
Force (N)
Jerk (g/s)
Time (ms)
Force
Jerk

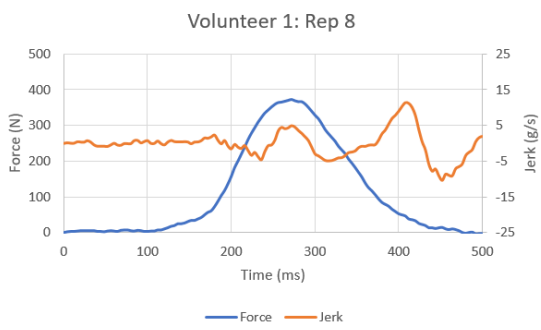
Volunteer 1: Rep 8
Force (N)
Jerk (g/s)
Time (ms)
Force
Jerk

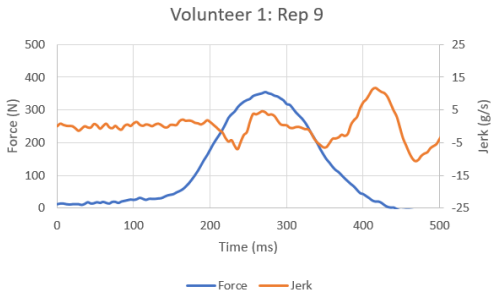
Volunteer 1: Rep 9
Force (N)
Jerk (g/s)
Time (ms)
Force
Jerk

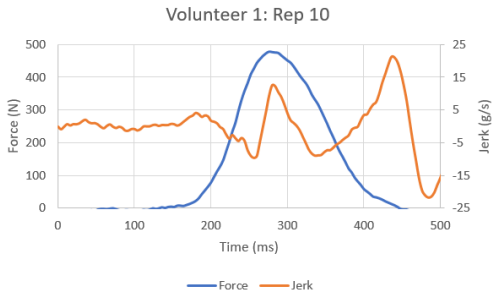
Volunteer 1: Rep 10
Force (N)
Jerk (g/s)
Time (ms)
Force
Jerk

APPENDIX XVI.

VOLUNTEER 2 GRAPHS

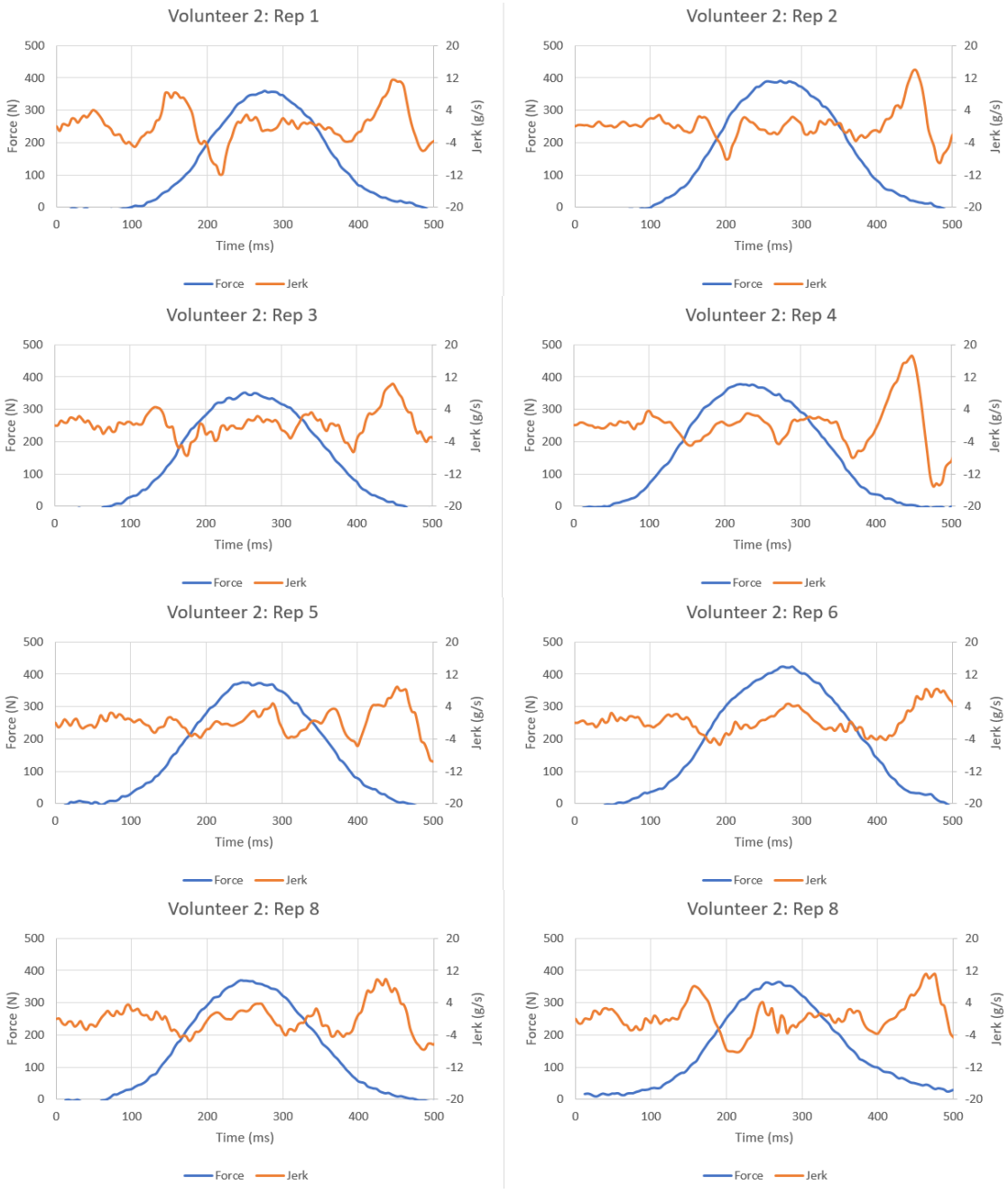


Volunteer 2: Rep 9
Force (N)
Jerk (g/s)
Time (ms)
Force
Jerk


Volunteer 2: Rep 10
Force (N)
Jerk (g/s)
Time (ms)
Force
Jerk

APPENDIX XVII.

VOLUNTEER 3 GRAPHS

* Only unique repetitions are graphed.

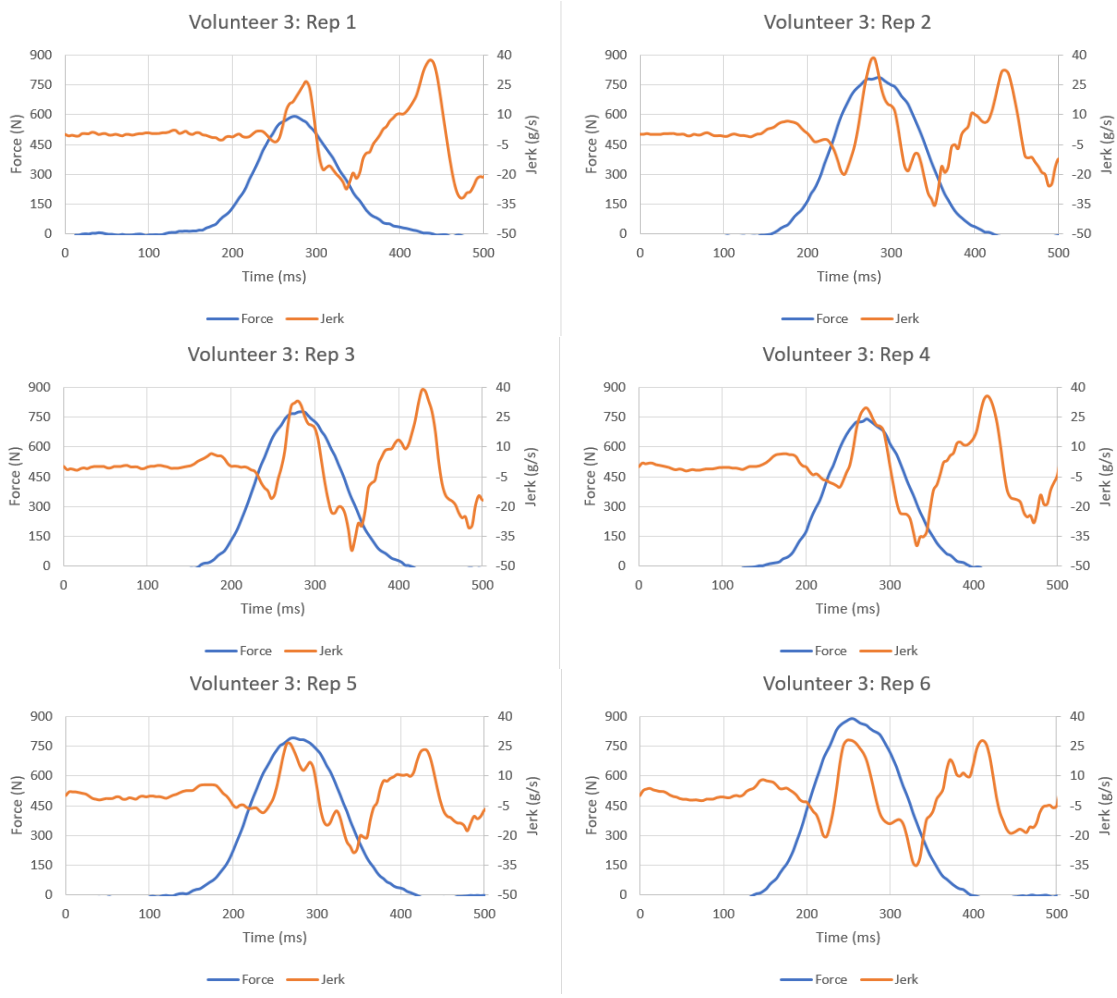

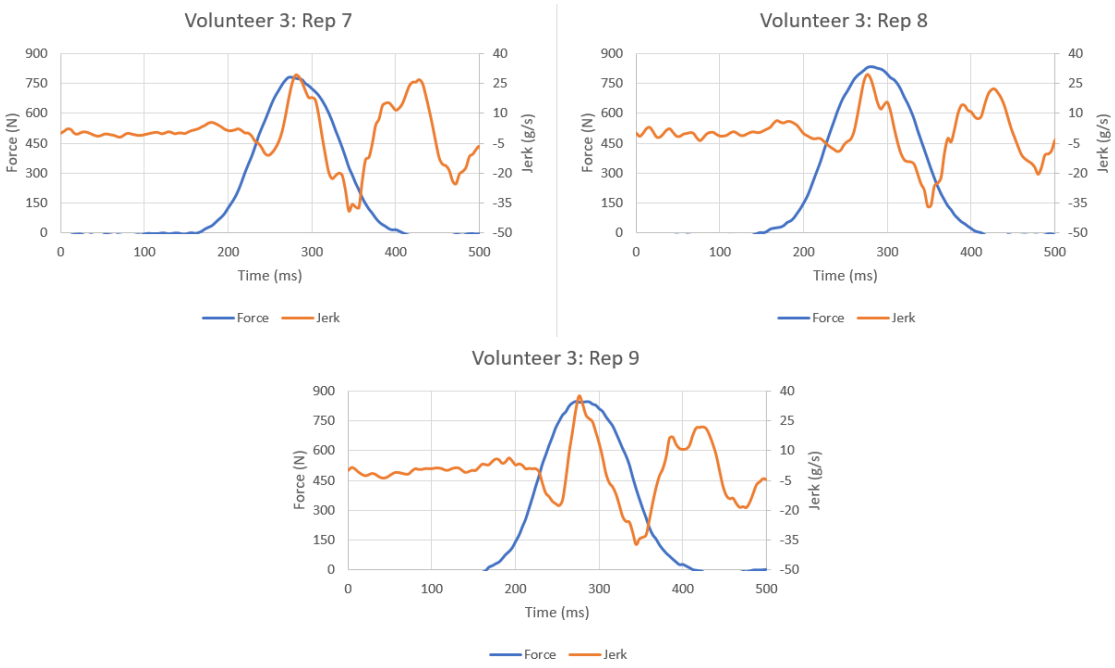
Volunteer 3: Rep 7
Force (N)
Jerk (g/s)
Time (ms)
Force
Jerk
Volunteer 3: Rep 8
Force (N)
Jerk (g/s)
Time (ms)
Force
Jerk
Volunteer 3: Rep 9
Force (N)
Jerk (g/s)
Time (ms)
Force
Jerk

APPENDIX XVIII.

VOLUNTEER 4 GRAPHS

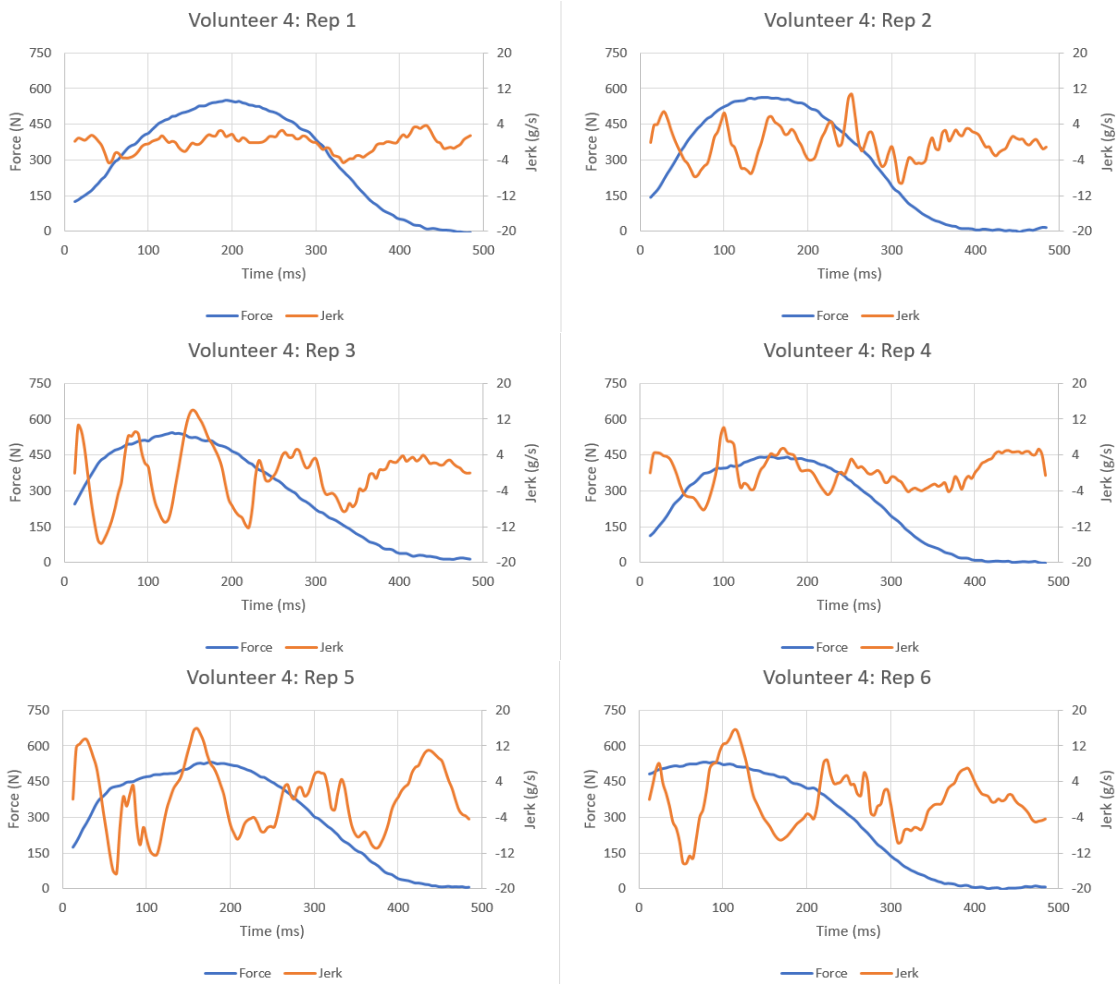


Volunteer 4: Rep 7
Force (N)
Jerk (g/s)
Time (ms)
Force
Jerk


Volunteer 4: Rep 8
Force (N)
Jerk (g/s)
Time (ms)
Force
Jerk

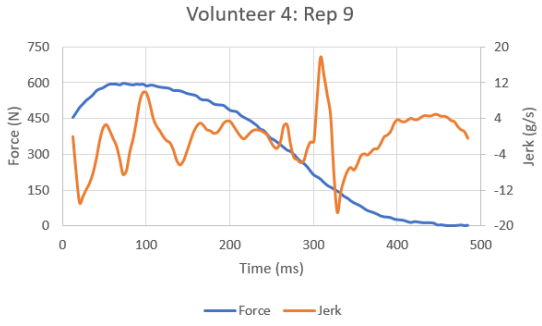
Volunteer 4: Rep 9
Force (N)
Jerk (g/s)
Time (ms)
Force
Jerk

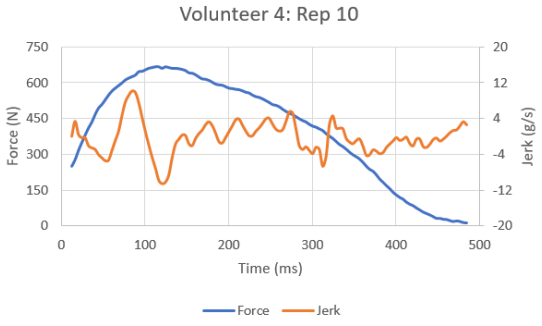
Volunteer 4: Rep 10
Force (N)
Jerk (g/s)
Time (ms)
Force
Jerk

APPENDIX XIX.

VOLUNTEER 5 GRAPHS

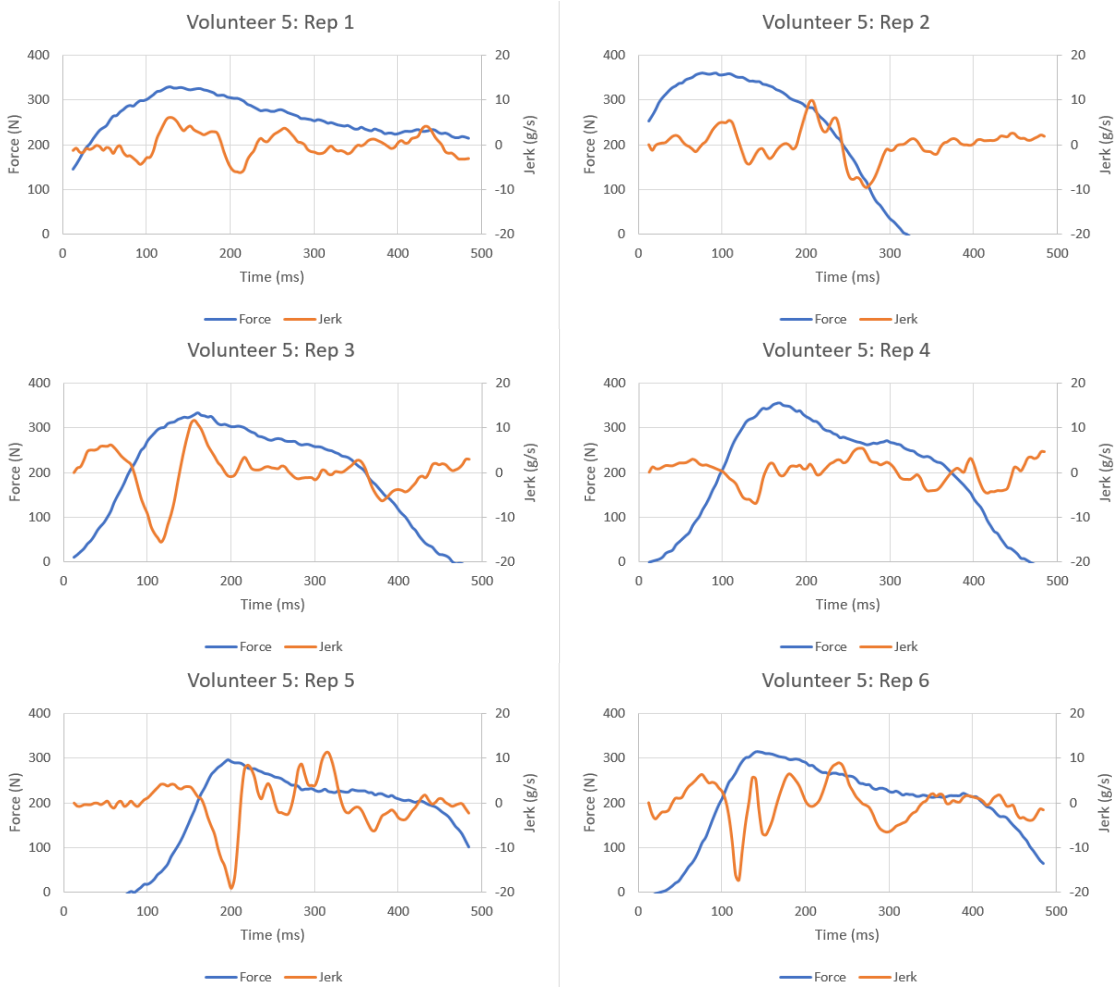

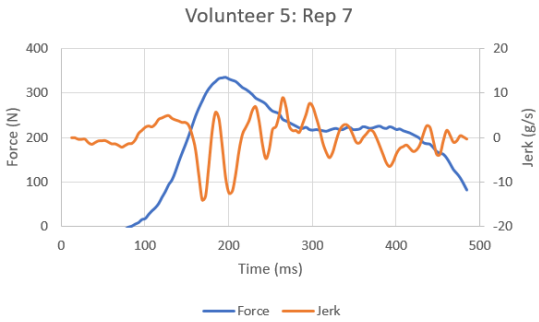
Volunteer 5: Rep 7
Force (N)
Jerk (g/s)
Time (ms)
Force
Jerk


Volunteer 5: Rep 8
Force (N)
Jerk (g/s)
Time (ms)
Force
Jerk

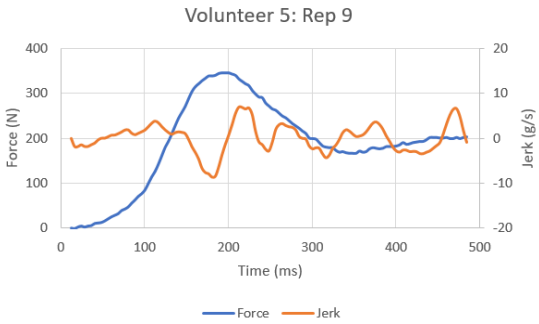
Volunteer 5: Rep 9
Force (N)
Jerk (g/s)
Time (ms)
Force
Jerk

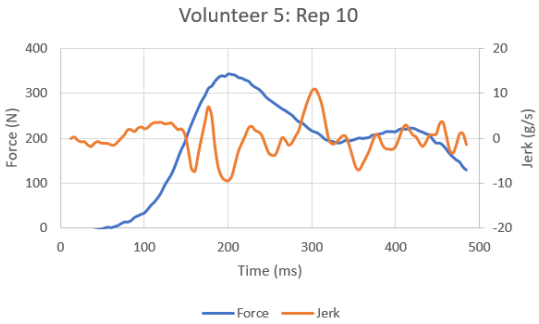
Volunteer 5: Rep 10
Force (N)
Jerk (g/s)
Time (ms)
Force
Jerk

APPENDIX XX.

VOLUNTEER 6 GRAPHS

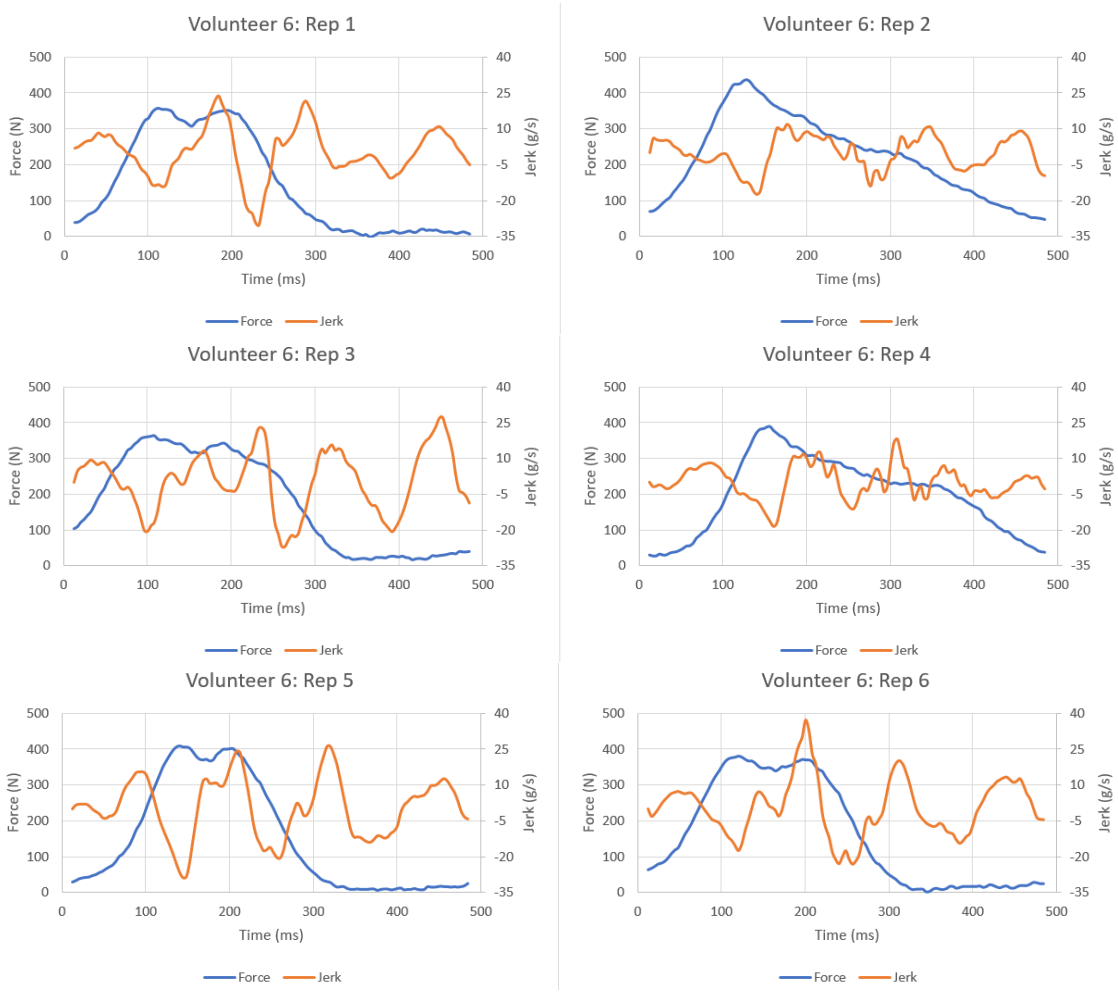


Volunteer 6: Rep 7
Force (N)
Jerk (g/s)
Time (ms)
Force
Jerk


Volunteer 6: Rep 8
Force (N)
Jerk (g/s)
Time (ms)
Force
Jerk


Volunteer 6: Rep 9
Force (N)
Jerk (g/s)
Time (ms)
Force
Jerk


Volunteer 6: Rep 10
Force (N)
Jerk (g/s)
Time (ms)
Force
Jerk

APPENDIX XXI.

VOLUNTEER 7 GRAPHS

* Only unique repetitions are graphed.

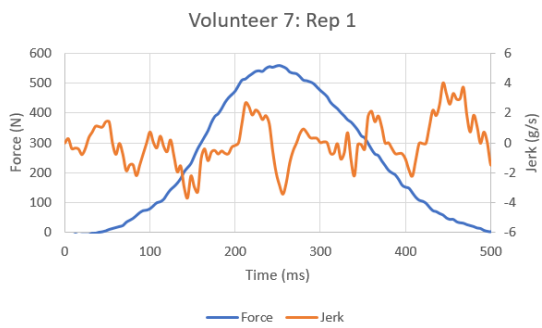

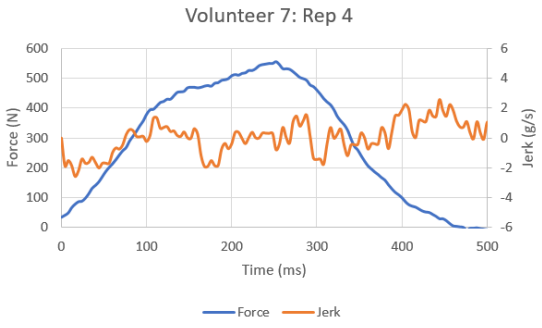

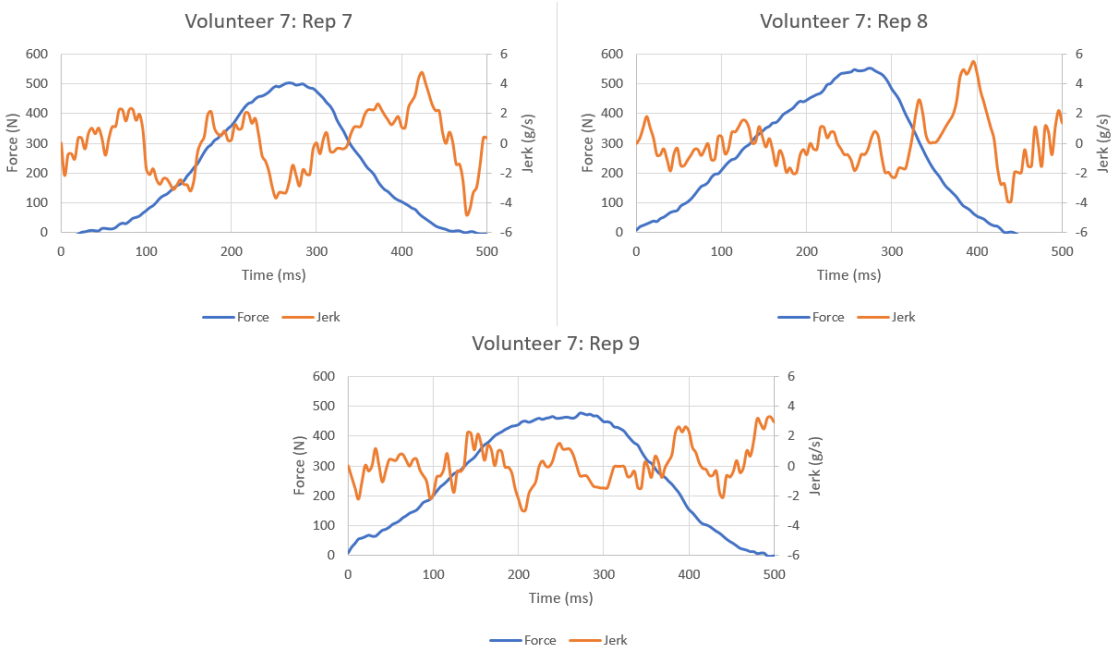
Volunteer 7: Rep 7
Force (N)
Jerk (g/s)
Time (ms)
Force
Jerk
Volunteer 7: Rep 8
Force (N)
Jerk (g/s)
Time (ms)
Force
Jerk
Volunteer 7: Rep 9
Force (N)
Jerk (g/s)
Time (ms)
Force
Jerk

APPENDIX XXII.

VOLUNTEER 8 GRAPHS

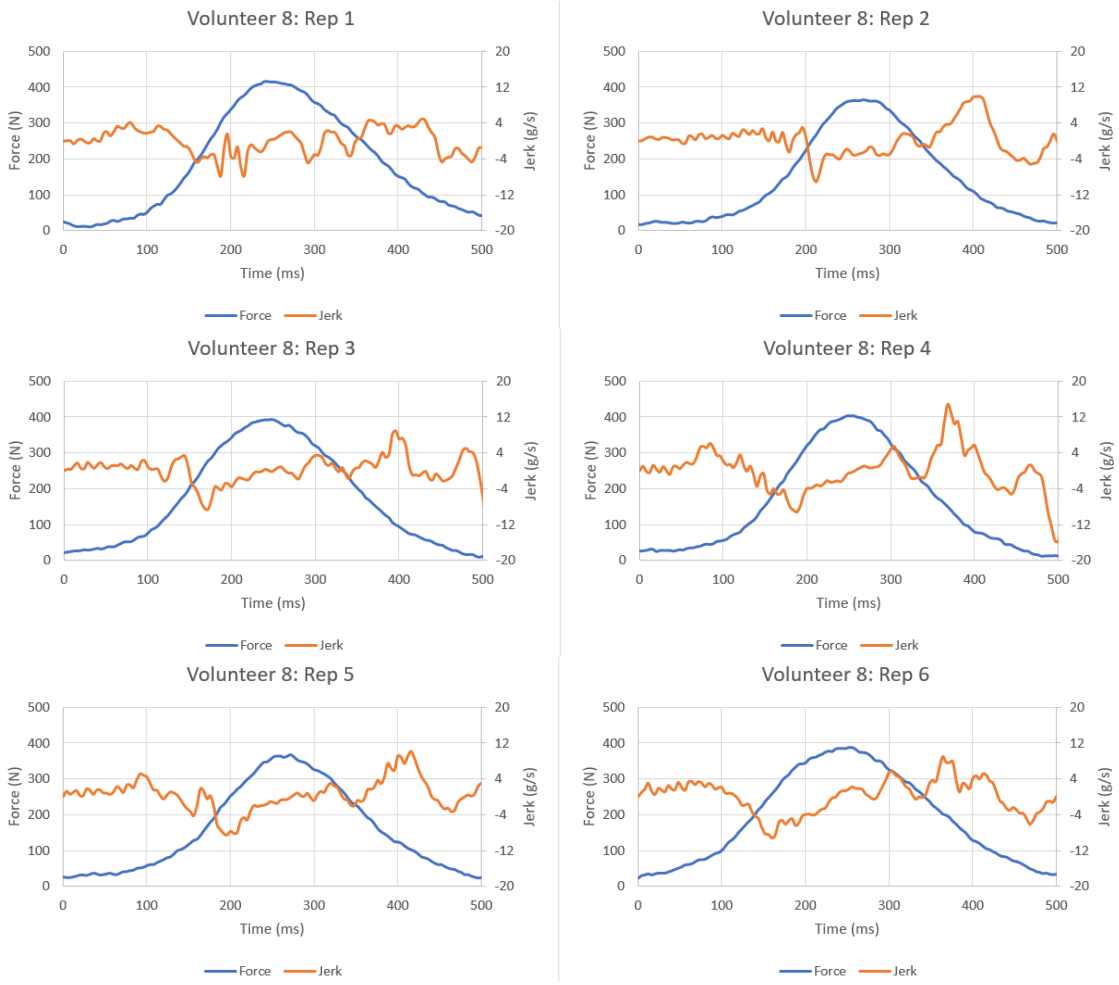

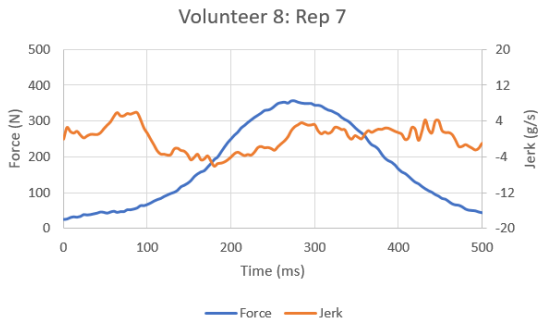
Volunteer 8: Rep 7
Force (N)
Jerk (g/s)
Time (ms)
Force
Jerk


Volunteer 8: Rep 8
Force (N)
Jerk (g/s)
Time (ms)
Force
Jerk


Volunteer 8: Rep 9
Force (N)
Jerk (g/s)
Time (ms)
Force
Jerk


Volunteer 8: Rep 10
Force (N)
Jerk (g/s)
Time (ms)
Force
Jerk

APPENDIX XXIII.

VOLUNTEER 9 GRAPHS

* Only unique repetitions are graphed.

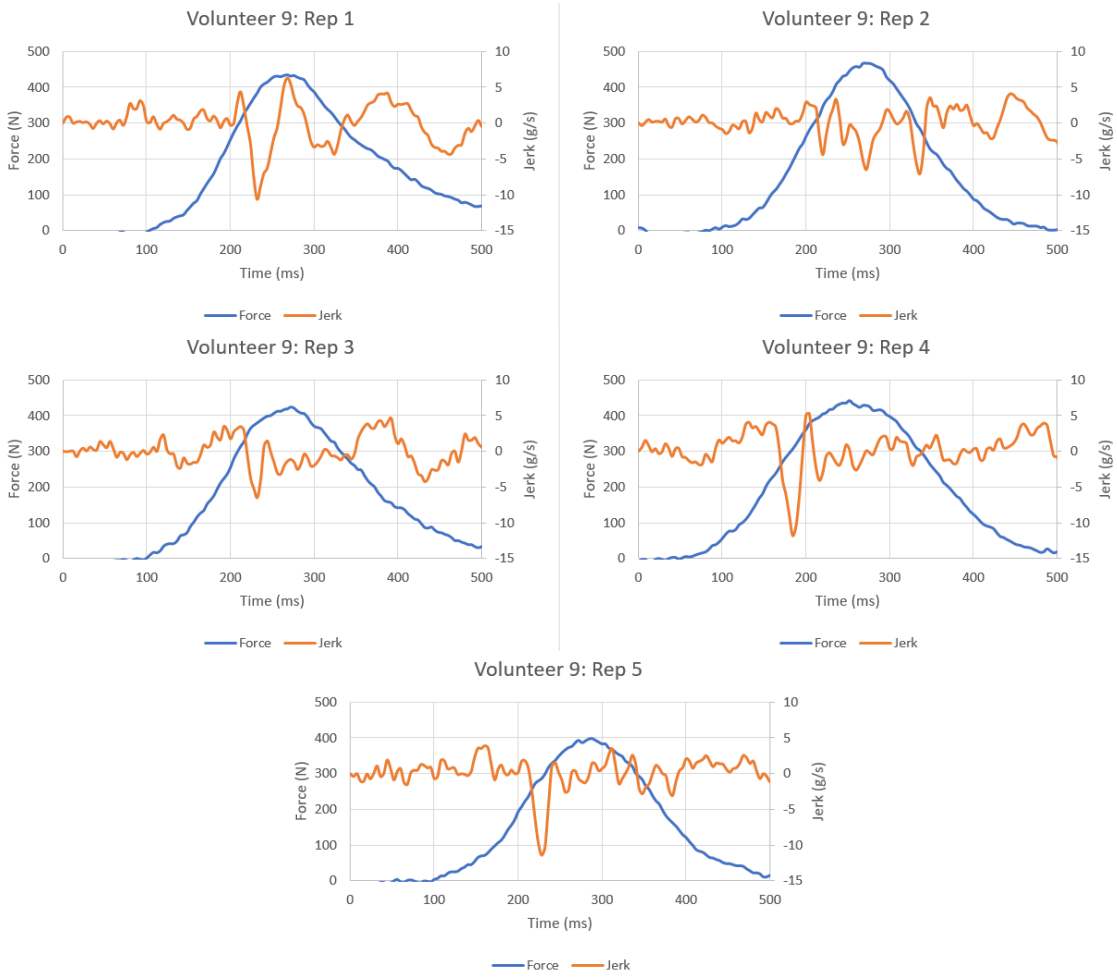

APPENDIX XXIV.

VOLUNTEER 10 GRAPHS

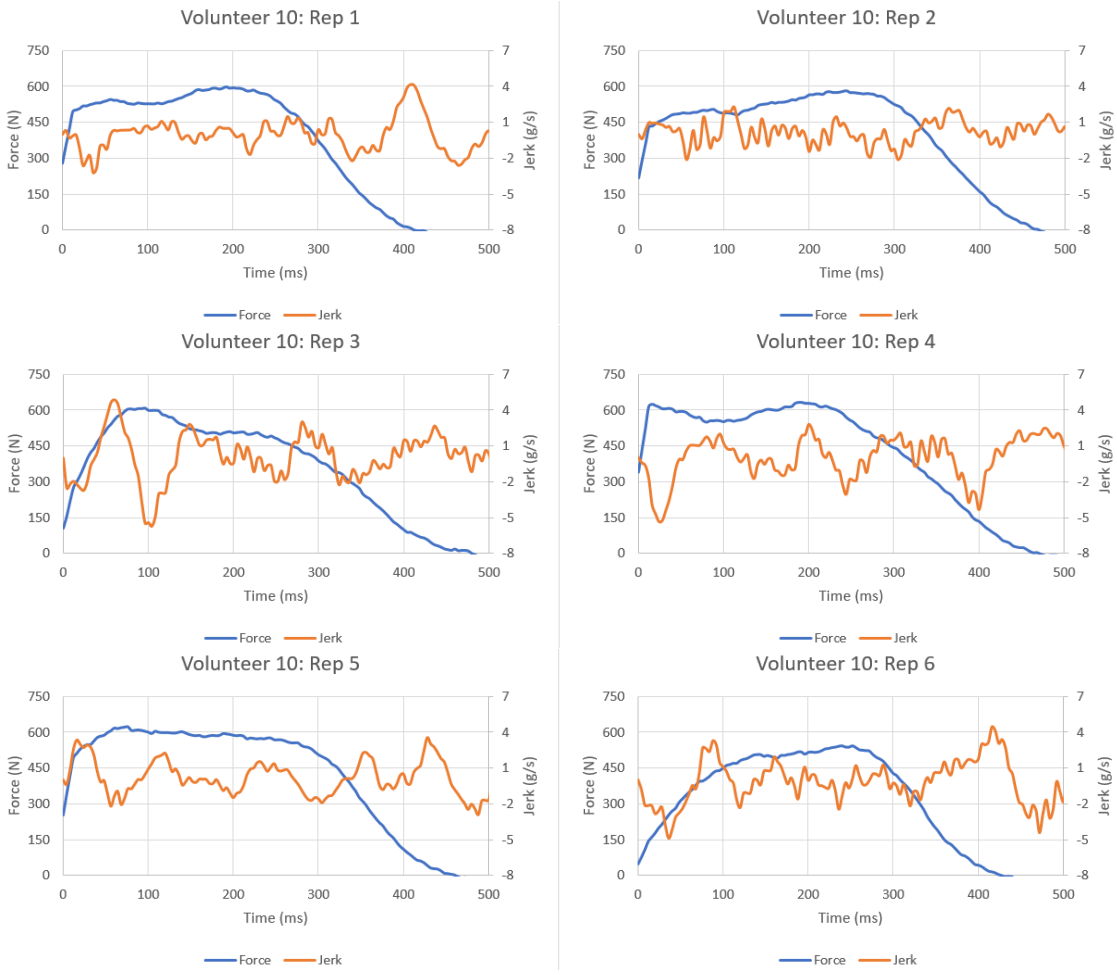


Volunteer 10: Rep 7
Force (N)
Jerk (g/s)
Time (ms)
Force
Jerk


Volunteer 10: Rep 8
Force (N)
Jerk (g/s)
Time (ms)
Force
Jerk


Volunteer 10: Rep 9
Force (N)
Jerk (g/s)
Time (ms)
Force
Jerk


Volunteer 10: Rep 10
Force (N)
Jerk (g/s)
Time (ms)
Force
Jerk


Volunteer 10: Rep 11
Force (N)
Jerk (g/s)
Time (ms)
Force
Jerk

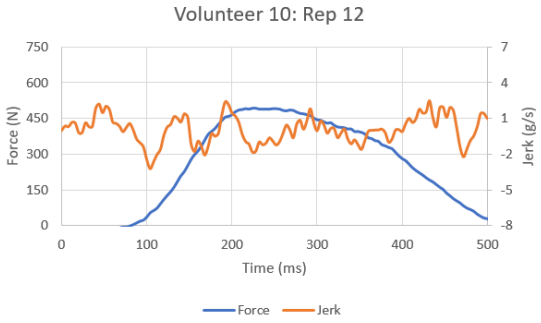
Volunteer 10: Rep 12
Force (N)
Jerk (g/s)
Time (ms)
Force
Jerk

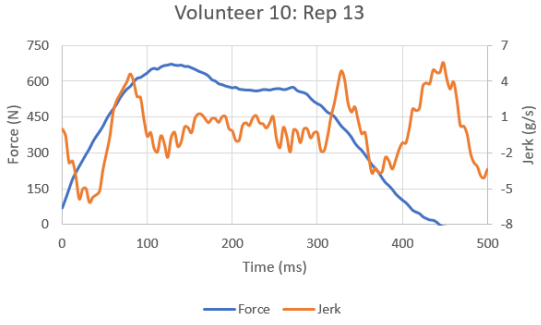
Volunteer 10: Rep 13
Force (N)
Jerk (g/s)
Time (ms)
Force
Jerk

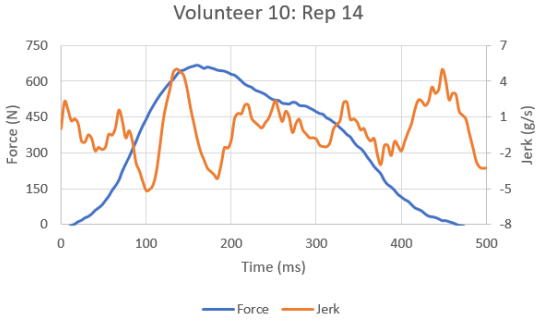
Volunteer 10: Rep 14
Force (N)
Jerk (g/s)
Time (ms)
Force
Jerk

VITA

Sean Coyle is a Louisville native who received his Bachelor of Science in Bioengineering at the University of Louisville's J.B. Speed School of Engineering in 2016. Motivated by curiosity and a passion for the human body in addition to his experiences with Ohio Willow Wood Company and Frazier Rehab Institute, Sean went on to achieve his Master of Engineering in Bioengineering to be received in 2020. Orthopedics, device design, and exercise have been particular interests that ultimately guide the direction of his study among other personal pursuits.